JACS
JOURNAL OF THE AMERICAN CHEMICAL SOCIETY

Carbohydrate-Mediated Purification of Petrochemicals

James M. Holcroft[†‡], Karel J. Hartlieb[†‡], Peyman Z. Moghadam[§], Jon G. Bell[×], Gokhan Barin[ₒ], Daniel P. Ferris[†], Eric D. Bloch[ₒ], Mohammed M. Algaradah[¶], Majed S. Nassar[¶], Youssry Y. Botros[¶ǂ], K. Mark Thomas[×], Jeffrey R. Long[ₒ], Randall Q. Snurr[§], J. Fraser Stoddart[†*]

[†]*Department of Chemistry, Northwestern University, 2145 Sheridan Road, Evanston, IL 60208 −3113, USA*

[§]*Department of Chemical & Biological Engineering, Northwestern University, 2145 Sheridan Road, Evanston, IL 60208 −3120, USA*

[ₒ]*Department of Chemistry, University of California, Berkeley, CA 94720 −1460, USA*

[×] *Wolfson Northern Carbon Research Laboratories, School of Chemical Engineering and Advanced Materials, Newcastle University, Newcastle upon Tyne NE1 7RU, UK*

[¶] *Joint Center of Excellence in Integrated Nano-Systems (JCIN), King Abdul-Aziz City for Science and Technology (KACST), P. O. Box 6086, Riyadh 11442, KSA*

[ǂ] *University Research Office, Intel Corporation, Building RNB-6-64, 2200 Mission College Boulevard, Santa Clara, CA 95054 −1549, USA*

[*]E-mail: stoddart@northwestern.edu

MAIN TEXT

***Correspondence Address**

Professor J Fraser Stoddart

Department of Chemistry

Northwestern University

2145 Sheridan Road

Evanston, IL 60208-3113 (USA)

Tel: (+1)-847-491-3793

E-Mail: *stoddart@northwestern.edu*

ABSTRACT: Metal-organic frameworks (MOFs) are known to facilitate energy-efficient separations of important industrial chemical feedstocks. Here, we report how a class of green MOFs – namely CD-MOFs – exhibits high shape-selectivity towards aromatic hydrocarbons. CD-MOFs, which consist of an extended porous network of γ-cyclodextrins (γ-CDs) and alkali metal cations, can separate a wide range of benzenoid compounds as a result of their relative orientation and packing within the transverse channels, formed from linking $(\gamma\text{-CD})_6$ body-centered cuboids in three dimensions. Adsorption isotherms and liquid-phase chromatographic measurements indicate a retention order of *ortho*- > *meta*- > *para*-xylene. The persistence of this regioselectivity is also observed during the liquid-phase chromatography of the ethyltoluene and cymene regioisomers. In addition, molecular shape-sorting within CD-MOFs facilitates the separation of the industrially relevant BTEX (Benzene, Toluene, Ethylbenzene and the Xylene isomers) mixture. The high resolution and large separation factors exhibited by CD-MOFs for benzene and these alkylaromatics provide an efficient, reliable and green alternative to current isolation protocols. Furthermore, the isolation of the regioisomers of (i) ethyltoluene and (ii) cymene, together with the purification of (iii) cumene from its major impurities (benzene, *n*-propylbenzene and diisopropylbenzene), highlight the specificity of the shape-selectivity exhibited by CD-MOFs. Grand canonical Monte Carlo (GCMC) simulations and single component gas adsorption isotherms reveal the origin of the shape-selectivity and provide insight into the capability of CD-MOFs to serve as versatile separation platforms derived from renewable sources.

■ INTRODUCTION

With the expanding global demand for petrochemical feedstocks, the development of novel, low-cost materials that reduce the impact of chemical processing on the environment is critically important. Improving the efficiency of the refinement and separation of aromatic hydrocarbons is of particular importance, given the large volumes on which these compounds are produced. The sustained interest in metal-organic frameworks[1] (MOFs) as adsorbents and

sequestering agents for industrially important gases,[2–4] e.g., H_2, CH_4, CO_2 and N_2, as well as for the liquid-phase separation of larger molecular compounds, which include 1) constitutional isomers,[5] 2) chiral compounds,[6] 3) aliphatic hydrocarbons[3b, 5b, 7] and 4) pharmaceuticals,[8] is leading to MOFs being investigated as alternatives to zeolites[9] and activated carbon[10] as separation media. The improvements[5–7] in separation efficiencies using MOFs over traditional size- and shape-selective materials can be attributed primarily to (i) the physiochemical properties imbedded in their diverse building blocks, (ii) their higher surface areas and (iii) their larger adsorption capacities, which reduce the amount of adsorbent required for industrial processes.[7a,11] Consequently, MOFs represent emergent materials for separation technologies in many different industrial settings.

In the chemical industry, one of the most challenging separations is that of BTEX — benzene, toluene, ethylbenzene and the three regioisomers of xylene — obtained from the refining of crude oil. The xylene isomers, together with ethylbenzene, constitute the C_8 aromatics, that are derived[12] from crude oil by catalytic reforming, toluene disproportionation and the distillation of pyrolysis gasoline. These C_8 aromatics not only act[12b] as octane and antiknocking additives in gasoline, but they are also important chemical feedstock's, thus bringing about the necessity for their processing and separation. The difficulty in separating *para*-xylene from the BTEX mixture can be ascribed to the similar physical properties (Supplementary Table 2) of these C_8 aromatics. Industrial practices[12-13] focus on separation by adsorption strategies or crystallization procedures, with 60% of *para*-xylene produced today relying on simulated moving bed (SMB) technologies.[12, 13] Here, C_8 aromatics are separated based on differences in adsorbate-adsorbent interactions within faujasite-type zeolites. The xylene adsorption equilibrium can be tuned by ion-exchange within the zeolite to attain[9a, 12a, 14] *para*-xylene purities of approximately 95 wt% per pass. Crystallization techniques account for the purification of the remaining 40% of *para*-xylene produced.[13b, 13c, 15] These energy intensive processes highlight the need for further improvements in the technologies currently available,

especially in relation to materials that can discriminate amongst BTEX molecules. A wide variety of materials have been investigated for the separation of aromatic hydrocarbons, such as zeolites,[9, 12a] discrete metal complexes[16] and organic cages.[17] MOFs have exhibited varying degrees of success in separating xylenes from mixtures of C_8 aromatics, e.g., classical rigid MOFs, such as copper benzenetricarboxylate [$Cu_3(btc)_2$], have been employed to separate BTEX mixtures chromotographically,[18] whilst MOF-5 shows little to no separation of the xylene isomers.[19] The most widely investigated MOFs for separating aromatic hydrocarbons are the terephthalate-based structures with one-dimensional channels,[20–24] namely MIL-47 and MIL-53, both MOFs exhibit high *ortho*-xylene selectivity, separating the xylene regioisomers based on molecular packing and entropic differences.[21–23, 25] More recently,[26, 27] MIL-125 and MAF-X8 have exhibited high *para*-xylene affinity due to pore morphology and commensurate stacking, respectively. The guest-driven restructuring of a flexible cerium tetradentate carboxylate MOF has led to high selectivity by restructuring of the MOF around *para*- and *meta*-xylene, displaying molecular level recognition,[28] and adding to the growing number of flexible MOFs of potential utility for separations.[6h, 21, 28]

Here, we report the high selectivity of CD-MOFs (Fig. 1) for the separation of aromatic hydrocarbons. These frameworks can be synthesized readily in kilogram quantities from γ-cyclodextrin[29] (γ-CD) and alkali metal cations in aqueous media under ambient conditions. The resulting extended structures are body-centered cubic and are composed[30–32] of six γ-CD units coordinated by the cations to form (Fig. 1a−c) three-dimensional porous structures. The shape and topology of the cavities suggest that the CD-MOF frameworks are capable of shape-selective adsorption (Fig. 1d). This extended porous network exhibits a BET surface area[30, 31] of 1030 m^2 g^{-1}. The combination of high porosity with multifarious nanopores affords a structure analogous to that of zeolites. In the case of CD-MOF, we will show that the high selectivity for different aromatic hydrocarbons results from van der Waals (vdW) interactions within the transverse pores (0.71 nm), that connect the $(\gamma\text{-CD})_6$ units (Fig. 1a). The focus of our research has been the

separation of aromatic hydrocarbons, such as multisubstituted benzenes, toluenes, cumene and the regioisomers of xylene that complement the shape of the transverse pores. Owing to the similarities in the physical properties of these important chemical feedstock's, molecular shape is one of the most prominent distinguishing features, and thus materials capable of shape-selectivity should prove to be promising separation media.[6h, 21, 25, 28]

■ EXPERIMENTAL SECTION

The full experimental details are provided in the Supporting Information. The most important information is summarized below briefly.

Materials and General Methods. Potassium hydroxide, rubidium hydroxide hydrate, cetyltrimethylammonium bromide (CTAB) and MeOH were all purchased from Sigma Aldrich, while γ-cyclodextrin[29] (γ-CD) was obtained from WACKER (CAVAMAX W8 PHARMA). All chemicals were used as received without further purification. CD-MOF-1 and CD-MOF-2 were prepared according to the literature procedures.[30, 32] Particle size control experiments on CD-MOF-1 were undertaken using a modified protocol from the literature.[32] Large CD-MOF-2 crystals were harvested and ground using a KRUPS type F203 blender prior to grinding with a mortar and pestle. The ground particles were sieved under an atmosphere of nitrogen through Gilson Company Inc. membrane sieves, #170, #230 and #400, to obtain final particle sizes between 10–37 μm that were unable to pass through a 10 μm sieve. Optical microscope (OM) images for CD-MOF-1 size-controlled particles and CD-MOF-2 particles after grinding were obtained using an Olympus BX53 microscope with an Olympus DP25-mounted camera. Scanning electron microscopy (SEM) images were collected on a Hitachi S-3400N-II variable pressure SEM, with a tungsten filament and ESED II detector. Samples used for SEM images were suspended in MeOH and diluted to 1 mg mL^{-1} using serial dilutions before deposition onto a carbon tape. The samples were then dried under vacuum for 30 min before imaging them at 30 kV under high vacuum. Powder X-ray diffraction patterns of CD-MOF-1 and CD-MOF-2 were

collected on a Bruker AXS APEX2 diffractometer, equipped with a CCD detector and a CuKα IμS microfocus source with MX optics. Data were collected with an area detector as rotation frames over 180° in φ at 2θ values of 12 and 24° and exposed for 10 min for each frame. At a distance of 150 mm, the detector area covers 24° in 2θ. Overlapping sections of data were matched and the resulting pattern integrated using the Bruker APEX2 Phase ID program. Powder pattern data were treated for amorphous background scatter. HPLC was carried out using a Shimadzu analytical normal-phase HPLC, equipped with a Shimadzu SIL-20A HT prominence auto-sampler, SPD-M20A prominence diode array detector, LC-20AB prominence LC and a DGU-20A3 degasser. The normal phase HPLC was fitted with CD-MOF packed columns with dimensions 250 mm length, 4.6 mm internal diameter x 1/4" outer diameter. Unless otherwise stated, chromatography was carried out using HPLC grade hexane as the mobile phase at a flow rate of 1 mL min^{-1}, with 10 μL injection volumes of 50 mg mL^{-1} solutions. Single component gas adsorption isotherms were conducted on an IGA gravimetric analyser (Hiden Isochema, IGA-001, Warrington, UK). The analyzer is an ultra-high vacuum (UHV) one comprising of a computer-controlled microbalance with both pressure and temperature regulation systems. The microbalance has a long-term stability of ± 1 μg with a weighing resolution of 0.2 μg. The CD-MOF-2 sample was outgassed for 12 h until a constant weight was achieved, at < 10^{-6} Pa, at 60°C prior to adsorption measurements. The pressure transducers had ranges of 0 – 2, 2 – 100 and 100 – 1000 mbar. Vapor sorption isotherms were obtained using a circulating water-ethylene glycol bath controlled by a computer using IGA software. The xylene regioisomers used to generate the vapor for the isotherm measurements were degassed fully by repeated evacuation and equilibration cycles of the vapor reservoir. The vapor pressure was gradually increased to the desired point during ~ 30 s in order to prevent disruption of the microbalance. It follows that the period during which the pressure change occurs is small when compared with the adsorption kinetics, allowing isotherm adsorption kinetics to be obtained for each pressure step. The sample temperature was measeured using a

thermocouple located 5 mm from the sample. The pressure set point was maintained by computer control throughout the duration of the experiment. Breakthrough experiments were carried out in a 4-mm glass U-tube with CD-MOF-2 crystals. CD-MOF-2 (1.46 g) was used in order to fill the tube at a length of 16 cm. The sample was purged with dry N_2 at 60 ºC overnight to ensure the complete activation of the sample prior to breakthrough measurements. Dry N_2 at a rate of 20 mL/min was bubbled through a mixture of the xylene isomers (15 mL each) at atmospheric pressure. The effluent was passed through a VICI Valco 6-way sampling valve. An aliquot (0.25 mL) of gas was sampled every 5 min and delivered to a Perkin Elmer Clarus 500 Gas Chromatograph fitted with a Supelco SCOT capillary GC column (Sigma-Aldrich 23813-U, 50 ft long, 0.02 in. outside diameter) maintained at 90 ºC. The analyses were performed using an injector and detector (FID) temperature of 220 ºC and N_2 was used as the carrier gas which was maintained at an inlet pressure of 1.5 psi with a split ratio of 10:1. Baseline separation of the xylene isomers was achieved and all peaks were easily integrated in the resulting GC trace.

Synthetic Protocols. The extended metal-organic frameworks, CD-MOF-1 and CD-MOF-2, were prepared according to literature procedures.[30, 32]

CD-MOF-1: γ-CD (1.30 g, 1 mmol) and KOH (0.45 g, 8 mmol) were dissolved in H_2O (20 mL). The solution was filtered through a 45-μm syringe filter and decanted into separate vials. MeOH was allowed to diffuse slowly into the solution over a period of a week.

CD-MOF-2: γ-CD (1.30 g, 1 mmol) and RbOH (0.82 g, 8 mmol) were dissolved in H_2O (20 mL). The solution was filtered through a 45-μm syringe filter and decanted into separate vials. MeOH was allowed to diffuse slowly into the solution over a period of a week.

Particle Preparation and Activation. The crystals were harvested and crushed to sizes of approximately 100–500 μm. The crystals were filtered and washed with MeOH (4 x 50 mL) under vacuum. Additional washing with CH_2Cl_2 (3 x 50 mL) was carried out to remove the excess of MeOH. The crystals were then left to vacuum dry for 12 h. The crystals were transferred to a N_2 glovebox where they were finely ground using a KRUPS type F203 blender,

prior to being ground further using a mortar and pestle. The resulting particles were sieved through Gilson Company Inc. membrane sieves, #170, #230 and #400 with repeated grinding between sieving through each membrane to ensure particles smaller than 37 μm were attained. The milled CD-MOF-2 particles were checked for crystallinity and structural integrity using powder X-ray crystallography before being dry loaded or slurry loaded using any non-aqueous solvent into the column (SI B4).

Particle Size Control Synthesis of CD-MOF-1. CD-MOF-1 was synthesized using a modified literature proceedure.[30]

CD-MOF-1-Micro: γ-CD (8.15 g, 6.2 mmol) and KOH (2.8 g, 49.7 mmol) were dissolved in H_2O (250 mL). The solution was filtered through a 45-μm syringe filter and decanted into separate vials (5 mL in each vial). MeOH was allowed to diffuse slowly into the solutions for 24 h. Each solution was decanted into a fresh vial before cetyltrimethylammonium bromide (CTAB) was added, and after the complete dissolution of CTAB, MeOH was diffused into the solution for an additional 24 h. The solutions were combined together, and centrifuged at 5000 rpm for 10 min before the supernatant was removed and replaced with MeOH. This process was repeated five times in order to ensure CTAB was completely removed from the sample.

Varying the amount of CTAB during the synthesis of CD-MOF-1 can be used to control the size of the CD-MOF-1 particles as confirmed (Table 1) by optical microscopy and SEM. The size of the CD-MOF-1 particles is utilized in this system to control the elution times of the aliphatic and aromatic compounds by optimizing packing conditions to prevent the bypassing of the solid phase. The particle size modified column was prepared using CD-MOF-1-Micro-2 , where CTAB (40 mg) was added to the reaction mixture after the first incubation period. This protocol facilitated the formation (Figure 2) of CD-MOF-1 crystallites of 10–15 μm.

HPLC Column Loading. HPLC was carried out using a Shimadzu analytical normal-phase HPLC, fitted with a CD-MOF packed column with dimensions 250 mm in length and 4.6 mm internal diameter and 1/4" outer diameter. Chromatography was carried out using HPLC-

grade hexane as the mobile phase at a flow rate of 1 mL min^{-1}, with 10 μL injection volumes of 50 mg mL^{-1} solutions, unless otherwise stated. The CD-MOF particles were checked for their crystallinity and structural integrity using powder X-ray crystallography before being packed into the column. The blended CD-MOF-2 particles can be dry loaded or slurry loaded — using any non-aqueous solvent ─ into the column, whilst the 10–15 μm particles of CD-MOF-1 were slurry loaded using a non-aqueous solvent.

■ RESULTS AND DISCUSSION

CD-MOFs, which can be synthesized from γ-CD and a variety of alkali cations, have identical extended structures, aside from the identity of the cations — CD-MOF-1 contains potassium while CD-MOF-2 incorporates rubidium. CD-MOF-2 crystals were grown[30] by vapor diffusion of MeOH into an aqueous solution of γ-CD and RbOH.

Top-Down Protocol. Crystals were harvested, ground into smaller particles using a mortar and pestle and sieved sequentially through a series of mesh sizes under a nitrogen atmosphere. The final top-down CD-MOF-2 particles (10–37 μm) were dry-loaded into a HPLC column with a length and internal diameter of 250 and 4.6 mm, respectively. The structural stability of CD-MOF-2 during the column preparation phases was monitored using powder X-ray diffraction at intervals throughout the process to ensure that crystallinity was maintained under these rigorous grinding protocols (Supplementary Figure 4). CD-MOF-2 remained crystalline during the column preparation phases, and it was shown to be suitable for separation experiments. By contrast, CD-MOF-1 did not retain its crystallinity during top-down processing and so could not be employed in top-down separation experiments.

Top-Down Separations. The top-down CD-MOF-2 HPLC column exhibited (Figure 3a) partial separation of *para*- and *meta*-xylene, followed by the complete separation of the *ortho*-xylene isomer. The high selectivity (separation factor α_{oxpx} = 16.4) of CD-MOF-2 for *ortho*- over *para*-xylene and the preference (α_{mxpx} = 3.44) for *meta*- over *para*-xylene indicate (Table 2) the potential of CD-MOF-2 as a viable separation medium for the regioisomers of xylenes when

compared (Table 3) to previously published[20-21, 25] separations using MOFs. The resolution of the *para*- and *meta*-xylene signals (resolution factor R_{mxpx} = 0.58), however, exhibits (Figure 3a) peak-merging near the baseline. The low resolution of the *para*- and *meta*-xylene isomers can be attributed to inefficient stationary-phase packing that is a consequence of the large particle size range (Supplementary Figure 1) produced during the preparation of the top-down CD-MOF-2 HPLC column. In a bid to overcome these resolution limitations, a bottom-up protocol for size-controlled growth of CD-MOF was implemented by modification of a previously reported methodology.[32]

Bottom-Up Protocol. The bottom-up synthesis facilitates rapid gram-scale production of 10–15 μm CD-MOF-1 particles. Not only is it attractive on a large scale to use the CD-MOF containing potassium ions, but it also transpires that CD-MOF-1 lends itself to more precise control of the particle size. The control of CD-MOF particle-size for the bottom-up production of HPLC columns was achieved through the modification of a previously reported method[31] where particle-size control, using the mother liquor of the standard CD-MOF synthesis, is determined by short incubation times and the quantities of cetyltrimethylammonium bromide (CTAB) added to the solution.[30, 32] Varying the quantities of CTAB during the crystallization of CD-MOF analogs to form micron-sized crystallites is particularly effective in the synthesis of CD-MOF-1 since increasing the amount of CTAB in each crystallization solution from 20 to 80 mg, reduces the size of CD-MOF-1 crystals from ≥25 to ≤10 μm, respectively. See Table 1. Particle size was evaluated using optical microscopy and SEM (Figure 2, Supplementary Figure 2), while the crystallinity of CD-MOF-1 samples corresponding to varying CTAB additions were confirmed by powder X-ray diffraction (Supplementary Figure 5). Based on these investigations, it was decided to proceed with the scale-up of CD-MOF-1, with each crystallization solution containing 40 mg CTAB, producing particles with a size distribution of 10–15 μm for optimized packing of the CD-MOF within HPLC columns.

Bottom-Up Separations. Baseline separation (Figure 3b) of all three xylene regioisomers was observed using the bottom-up CD-MOF-1 stationary phase. The elution order remains unchanged, with *para*-, followed by *meta*- and finally *ortho*-xylene and retention times similar to those observed for the top-down column. The bottom-up CD-MOF-1 column provides much improved signal resolutions (R_{mxpx} = 2.17 and R_{oxpx} = 6.43) and separation factors (α_{mxpx} = 2.67, α_{oxpx} = 17.9 and α_{oxmx} = 6.73) compared to the values obtained using the top-down approach (Table 2). Comparison of CD-MOF-1 with previously reported MOFs shows that its ability to separate the xylene regioisomers is at least comparable[20, 25] with MIL-53(Fe) and MIL-47 (Table 3). The green nature of CD-MOF-1, however, provides a separation medium with a significantly reduced carbon foot-print compared to that of the terephthalate-based MIL materials.

Bottom-Up BTX and BTEX Separations. As part of an effort to investigate the versatility of CD-MOF-1 as a separation medium, BTX and BTEX mixtures were tested on the bottom-up column. Initial separation runs of BTX after 4 hours of column usage, with hexane as the mobile phase, demonstrated (Figure 4a) that CD-MOF-1 can separate toluene from the xylene isomers at 298 K, but with no separation of benzene from *meta*-xylene. With continued usage of the column in the presence of hexane, however, the separation of toluene and benzene from *meta*-xylene can be achieved (Figure 4b) after 30 hours, resulting in an improvement of the separation factors (Supplementary Table 4) from α_{bmx} = 1.12 and α_{tmx} = 1.58 to α_{bmx} = 3.10 and α_{tmx} = 2.17. We believe that MeOH retained in the framework from the particle preparation, is displaced slowly by hexane. These vacated sites within the framework are selective for toluene and benzene — the retention of benzene on the column is similar (Figure 4c) to that of *ortho*-xylene after 70 hours — preventing the complete separation of the BTX mixture when they are occupied by MeOH.

The foregoing experiment was repeated on a second bottom-up CD-MOF-1 column. Although similar results are observed for toluene and benzene, after flushing the column for 30 hours with hexane, the retention time of ethylbenzene is not influenced (Figure 4d) by the

column activation in the BTEX mixture. This observation suggests that sites within the framework are occupied originally by MeOH and after continued flushing with hexane, the MeOH is removed and these sites become ideal for the retention of toluene and benzene. It would appear that these sites are too small to accommodate larger aromatic hydrocarbons, i.e., those larger than and including ethylbenzene. In order to test this theory of competitive binding of MeOH in sites within the CD-MOF-1 framework, the column was flushed with a mixture of hexane:isopropanol 98/2 v/v. The saturation of the framework with isopropanol results (Figure 4e) in the deactivation of the column, with the retention times for benzene and toluene returning to those observed (Figure 4a) for a freshly prepared column. The retention times of the xylene isomers and ethylbenzene, however, remain the same, indicating that the change in retention times for toluene and benzene are not a consequence of increasing the mobile phase polarity. The CD-MOF-1 column was flushed for 1 hour with CH_2Cl_2 to remove ^{i}PrOH from the framework, followed by priming the column with HPLC-grade hexane for 1 hour. This procedure results in the full activation of the column and complete separation of BTEX mixtures (Table 4).

Bottom-up Separation of the Regioisomers of both Ethyltoluene and Cymene. The significant increase in retention times of small functionalized aromatics upon prolonged column usage is indicative of the removal of highly retained solvent (MeOH) within the CD-MOF-1 framework, allowing further adsorbate-adsorbent interactions. The emergence of this improved separation behavior, and the persistent ability of CD-MOF-1 to separate *para*-, *meta*- and *ortho*-substituted compounds with consistent elution orders, is exemplified by the separation (Figure 3c,d) of the regioisomers of both ethyltoluene and cymene. Here, we observe *para*-ethyltoluene to be the least retained isomer, followed by *meta*-ethyltoluene, whilst *ortho*-ethyltoluene is highly retained with a comparable elution time to that of *ortho*-xylene. The bottom-up CD-MOF-1 column separates the ethyltoluene isomers with separation factors (Table 5), α_{3et4et} = 2.10, α_{2et4et} = 13.8 and α_{2et3et} = 6.56, similar to those observed for the xylene isomers. The separation (Figure 3d) of the regioisomers of cymene highlights the extent of the *ortho*- >> *meta*- > *para*-

selectivity within the CD-MOF-1 framework. The selectivity order is consistent with that observed for the regioisomers of both xylene and ethyltoluene. CD-MOF-1 is capable of separating *para*- and *meta*-cymene from *ortho*-cymene as a consequence of the high *ortho*-selectivity observed within CD-MOFs. Baseline merging of the *para*- and *meta*-cymene signals, however, suggests that the limit of the shape recognition of CD-MOF-1 has been reached as a consequence of the additional steric bulk in the cymene isomers.

Bottom-Up Separation of Cumene from Impurities. The versatility of CD-MOF-1 as a stationary phase is highlighted (Supplementary Figure 12) by the purification of cumene from its impurities, *n*-propylbenzene and diisopropylbenzene, with separation factors (Supplementary Table 7), $\alpha_{npropdiiso}$ = 8.09 and $\alpha_{cumenediiso}$ = 7.12.

Static Vapor Adsorption Studies. Single-component isotherms were obtained for the adsorption of the regioisomers of xylene into CD-MOF-2 in order to be able to investigate the mechanism of vapor-phase adsorption and separation in relation to breakthrough studies.

Adsorption Isotherms. The isotherms for *para*-, *meta*- and *ortho*-xylene adsorption into CD-MOF-2 at 333 K are illustrated in Figure 5a. The isotherms were analyzed using the virial equation[33a] —

$$\ln(n/p) = A_0 + A_1 n + A_2 n^2 \quad \text{- - -} \qquad (1)$$

where p is the pressure, n is the amount of xylene absorbed and A_0, A_1, A_2 etc. are virial coefficients. At low surface coverage, the higher terms (A_2, A_3 --) etc. can be neglected. A plot of $ln(n/p)$ versus n gives a straight line for low uptakes. A_0 describes the adsorbate-adsorbent interaction, while A_1 describes the adsorbate-adsorbate interaction. A_0 values are related to Henry's Law by the equation $K_H = \exp(A_0)$, which quantifies the interaction strength at zero surface coverage.[33a]

Tabulated A_0 and A_1 parameters along with Henry's Law constants are shown (Supplementary Table 12, 13). The A_1 parameters calculated show that the adsorbate-adsorbate interactions are significantly lower for *para*-xylene (–2630.66 ± 209.09 g mol^{-1}) when compared

to the strongly interacting *meta*-xylene (–4640.87± 498.73 g mol^{-1}). and *ortho*-xylene (–4627.50 ± 480.56 g mol^{-1}). These values for A_1 parameters are similar to those reported for benzene, pyridine[33b] and chloroaromatics.[33c] The variation of A_1 parameters is indicative of different molecular interactions and packing arrangements within the nanopores at low uptakes. On the basis of the Henry's Law constants at 60°C, the selectivity follows the trend *para* > *meta* > *ortho* when adsorption is at equilibrium. Dynamic breakthrough usually occurs, however, under non-equilibrium conditions because of mass transfer resistance. Static kinetic measurements were performed to determine the rates of adsorption of each regioisomer as a function of pressure and amount adsorbed.

Kinetic Studies. Fickian,[33d] Linear Driving Force (LDF)[33e,f] and Combined Barrier Resistance Diffusion (CBRD)[33g] models (Supplementary Equation 4-11) were fitted to static mass relaxation profiles in order to establish the diffusional rate-determining process for each regioisomer and to quantify the diffusion coefficients for isothermal adsorption into CD-MOF-2. Fickian diffusion is consistent with diffusion along the pores being the rate-determining process, while the LDF mechanism is indicative of diffusion through a surface barrier. The CBRD model represents an intermediate situation where diffusion is controlled by the presence of a surface barrier, followed by diffusion into a microporous spherical particle. All kinetic calculations were based on a particle radius of 1.75 mm.

It is clear from a perusal of Figure 5b that as the *para*-xylene relative pressure increases, the diffusional mechanism transitions from Fickian to CBRD and finally to LDF. This observation is consistent with diffusion along the pores being the rate-determining process at low relative pressures and diffusion through a surface barrier at high relative pressures. In contrast, *meta*- and *ortho*-xylene follow the LDF diffusional model over the entire relative pressure range investigated (Figure 5b). At low relative pressure the diffusion coefficients are similar for all the regioisomers of xylene. On the plateau of the isotherm, the diffusion of *para*-xylene is much faster compared to that of *meta*- and *ortho*-xylene with diffusion coefficients equal to 1.6 x 10^{-9}

m^2 s^{-1} and 5.7 – 6.4 x 10^{-10} m^2 s^{-1} for *para*-, *meta*- and *ortho*-xylene respectively. The rate-determining process for the adsorption of the xylene regioisomers at high relative pressure/uptake is dependent on two dimensions of the adsorbate for diffusional processes involving a sphericaly shaped surface barrier. The smallest (3.8 − 3.9 Å) xylene regioisomer dimensions are almost identical. The second smallest dimension suggests the order *para* > *meta* ~ *ortho* for kinetics (*para*-xylene = 6.6 Å, *meta*-xylene = 7.3 Å and *ortho*-xylene = 7.3 Å),[32h] an observation which is consistent with static kinetic measurements at high relative pressure and the dynamic breakthrough measurements, demonstrating kinetic molecular sieving of xylenes based on molecular dimensions of the regioisomers.

Breakthrough Experiments. We extended our investigation to include vapor-phase breakthrough experiments, which were performed to evaluate the xylene isomer separation ability of a CD-MOF in the gas phase. A mixture of *para*-, *meta*-, and *ortho*-xylenes in N_2 was passed through a CD-MOF-2 packed breakthrough column at 343 K. The breakthrough curve (Figure 6a) displays an initial phase where all three regioisomers in the feed are adsorbed by the framework. The breakthrough curve for *para*-xylene is very fast and within the time resolution (~ 5 min) of the measurement technique. Once the material is saturated, the elution of *para*- and *meta*-xylene starts simultaneously, with the *para*-isomer concentration exceeding (Figure 6b) the feed concentration as a result of competitive adsorption with the *ortho*-isomer which rapidly displaces the adsorbed *para*-xylene. While the *para*-xylene concentration returns slowly to the feed concentration, the *meta*-xylene concentration continues to increase — presumably resulting from the displacement of adsorbed *meta*-xylene by adsorbing *ortho*-xylene which diffuses more slowly within the framework— until the breakthrough of *ortho*-xylene occurs. This behavior also points to the fact that *meta*-xylene is adsorbed more slowly than the *para*-isomer, an observation which is in agreement with the static vapor-phase measurements and liquid-phase separation results.

Computational Studies. In order to gain a better insight into the experimentally observed adsorption and separation capabilities of CD-MOF, gas phase Grand canonical Monte Carlo (GCMC) simulations were carried out for the adsorption of the xylene regioisomers in CD-MOF-2 at room temperature. Pure component adsorption isotherms (Figure 6c) for all the regioisomers show an initial adsorption at low pressures up to 1 Pa, followed by complete pore filling. The simulations reveal that the initial adsorption takes place in the transverse pores that connect the $(\gamma\text{-CD})_6$ units, and the second step is caused by the filling of the large central cavities. It should be noted that the small triangular pores in the CD-MOF framework are not accessible to any of the xylene isomers, even at saturation capacity. The pure component isotherms show that the total amount of *ortho*-xylene adsorbed is higher than the amount of either *meta*- or *para*-xylene throughout the entire pressure range.

Competitive adsorption of the xylene isomers was also investigated (Figure 6d−f) for binary, equimolar, gas-phase mixtures at 298 K. The order of preferential adsorption was found to be *ortho*- >> *meta*- > *para*-xylene, in very good agreement with the order of adsorption obtained in liquid-phase HPLC and gas-phase breakthrough experiments. CD-MOF-2 adsorbs (Figure 6e,f) *ortho*-xylene preferentially over either *meta*- or *para*-xylene at low loadings up to 0.001 kPa. Near saturation pressures, CD-MOF-2 is able to accommodate even greater amounts of *ortho*-xylene over *meta*- and *para*-xylene. In the case of the *meta*-/*para*-xylene mixture (Figure 6d), there is little difference in uptake between the isomers until 0.001 kPa, with *meta*-xylene adsorbed preferentially at higher pressures. The difference in the saturation loadings of *meta*- and *para*-xylene is not as significant as that observed between *ortho*-xylene and its regioisomers.

Snapshots from simulations (Figure 7) of the pure components and mixtures (Figure 8) at saturation pressures reveal that *ortho*-xylene packs in the optimum slipped geometry, arranged in π-π stacking arrays within the transverse channels throughout the CD-MOF-2 framework. The siting analysis also reveals that the orientation of *ortho*-xylene maximizes its retention within

CDMOF-2 by allowing interaction between both its methyl groups and the γ-CD rings. This particular stacking of *ortho*-xylene has been observed in AEL and AFI zeolites.[34] The constitution of methyl groups in *meta*- and *para*-xylene, however, prevents similar positioning of them with respect to the γ-CD rings without partial overlap (steric interactions) with the framework (Supplementary Figure 13). Therefore, *meta*- and *para*-xylene adsorb primarily inside the larger cavities and pack in disordered arrays throughout the transverse nanopores. The simulation snapshots (Figure 8) for the *ortho*-/*meta*- and *ortho*-/*para*-xylene mixtures show that *ortho*-xylene adsorbs almost exclusively in the available space in γ-CD rings that constitute the transverse pores. The ability of *ortho*-xylene to dominate site occupancy throughout the framework explains the high *ortho*-xylene affinities with respect to *meta*- and *para*-xylene observed in both the liquid- and gas-phase chromatographic experiments.

In an effort to understand the energetics of xylene interactions with CD-MOF-2, we calculated (Supplementary Table 11) the breakdown of the total potential energy into framework–xylene and xylene–xylene interactions. The potential energy is the sum of a dispersion-repulsion term calculated by the Lennard-Jones potential plus a Coulombic term. The contribution of Coulombic interactions is found to be small. The breakdown of energies also reveals that vdW interactions between xylene molecules and the framework are the major contributor to the total potential energy for all of the xylene mixtures. In the cases of *ortho*-/*para*- and *ortho*-/*meta*-xylene mixtures, the vdW energy between *ortho*-xylene and the framework is greater than that of *para*- or *meta*-xylene and the framework by ~10 and 5 kJ mol^{-1}, respectively, at higher pressures. Moreover, the vdW interactions among *ortho*-xylene molecules is also greater than that among *para*- and *meta*-xylene molecules by ~4−5 kJ mol^{-1}, indicating more efficient packing of *ortho*-xylene.

Examination of the simulation configurations shows that *ortho*-xylene can interact strongly with CD-MOF-2 by sitting perpendicular to the γ-CD units. To gain another perspective into the interaction energies between the xylenes and the γ-CD ring, we turned to quantum

mechanical calculations. We performed single-point density functional theory (DFT) calculations for different orientations of xylenes with respect to the γ-CD ring and scanned the binding energies of each xylene isomer as it was moved away from the center of the ring (Supplementary Figure 16,17). The interaction energies (Figure 9a− c) for xylene isomers at three different orientations, namely, 90°, 45° and 0° were compared. In the case where xylene isomers sit within the plane of the γ-CD ring (Figure 8a), *ortho*-xylene has a strong interaction with the framework. In contrast, there is an energy penalty for *meta*-xylene, and more prominently for *para*-xylene, to adopt this orientation (90°) within the γ-CD ring. Similar favorable binding energies towards *ortho*-xylene were observed (Figure 8b,c) when different orientations of the xylene isomers were used. This observation further supports our GCMC simulations that *ortho*-xylene has the highest affinity for the γ-CD rings in CD-MOF-2. For *meta*- and *para*-xylene, although the binding energy becomes favorable as the orientation of both isomers changes from 90° to 0°, *ortho*-xylene still has higher affinity for the γ-CD ring.

■ CONCLUSIONS

Our findings demonstrate that CD-MOFs, composed of green, readily available starting materials, can be tailor-made on the kilogram scale and used as a separation medium for aromatic hydrocarbons. CD-MOFs address the most challenging separations of petrochemical feedstocks, including benzene, toluene, ethylbenzene and the regioisomers of xylenes with separation factors and resolutions superior to those reported for other extended-framework materials. The versatility of CD-MOFs as separation media was demonstrated by exploring the purification of other aromatic hydrocarbons, with the preference of the stationary phase for *ortho*- >> *meta*- > *para*- retained in the separation of the regioisomers of both ethyltoluene and cymene. CD-MOFs are capable of separating *para*- and *meta*- from *ortho*-cymene, with baseline merging of the *para*- and *meta*-cymene signals, suggesting that the limit of the shape recognition of CD-MOFs has been reached. Although isotherm measurements indicate selective adsorption

of the *para*-xylene vapor at low relative pressure, breakthrough experiments contain a dynamic front at which component vapor pressures vary, resulting in non-equilibrium competitive adsorption, i.e. adsorption kinetics play a vital role in the separation of regioisomers. Diffusion along the pores is the rate-determining mechanism for *para*-xylene vapor at low relative pressure, while *meta*- and *ortho*-xylene adsorption is controlled by diffusion through a surface barrier. The variance in mechanisms of adsorption can be attributed to the smaller cross-sectional dimensions for *para*-xylene which enters the transverse pores parallel to the cyclodextrin ring more favorably. At high relative pressure, the mechanism changes to a linear driving force for all regioisomers and diffusion through a surface barrier is the rate-determining process. The diffusion coefficients measured under static conditions, which follow the order *para*- > *meta*- > *ortho*-xylene on the isotherm plateau, are consistent with breakthrough measurements. Molecular simulations suggest that the γ-cyclodextrin rings enable *ortho*-selectivity primarily through favorable adsorbent–adsorbate interactions and a highly efficient packing of the *ortho*-isomer within the framework which is confirmed by the adsorbate-adsorbate interactions from virial equation analysis. The larger size and steric bulk of the cymene isomers most likely decreases their ability to adopt more favorable relative orientations, resulting in (i) weaker interactions within the framework, (ii) shorter retention times and (iii) prevention of discrimination between *para*- and *meta*-cymene. The ability of CD-MOFs to separate cumene from its major impurities (benzene, *n*-propylbenzene and diisopropylbenzene), highlights the specificity of their shape-selectivity and potential for applications in the petrochemical industry. Considering the green and economical nature of CD-MOFs, one can envisage obtaining pure fractions of alkylaromatic hydrocarbons and using them as an *ortho*-selective adsorbents on the industrial scale.

■ ASSOCIATED CONTENT

Supplementary Information

Supplementary information is available in the online version of the paper. Reprints and permission information is available online at http://pubs.acs.org.

■ AUTHOR INFORMATION

Corresponding Author

stoddart@northwestern.edu

Author Contribution

‡ These authors contributed equally to this work

Notes

R. Q. S has a financial interest in the start-up company NuMat Technologies, which is seeking to commercialize metal-organic frameworks.

■ ACKNOWLEDGEMENTS

This research is part (Project 34-947) of the Joint Center of Excellence in Integrated Nano-Systems (JCIN) at King Abdulaziz City for Science and Technology (KACST) and Northwestern University (NU). The authors would like to thank both KACST and NU for their continued support of this research. R. Q. S. acknowledges support from the Army Research Office (W911NF-12-1-0130). Computational work was supported by Northwestern University's shared computer system, Quest (Project: P20261). The breakthrough experiments, performed at the University of California, Berkeley, were supported through the Center for Gas Separations Relevant to Clean Energy Technologies, an Energy Frontier Research Center funded by the U.S. Department of Energy, Office of Science, Office of Basic Energy Sciences under Award DE-SC0001015. G. B. thanks the Miller Institute for Basic Research in Science, University of California, Berkeley for a postdoctoral fellowship. J. G. B and K. M. T. thank the ESPRC (Project EP/K005499/1) for supporting the single component gas adsorption measurements preformed at the Wolfson Northern Carbon Laboratories, Newcastle University.

■ REFERENCES

(1) (a) Hoskins, B. F.; Robson, R., *J. Am. Chem. Soc.* **1989**, *111*, 5962. (b) Hoskins, B. F.; Robson, R., *J. Am. Chem. Soc.* **1990**, *112*, 1546. (c) Fujita, M.; Kwon, Y. J.; Washizu, S.; Ogura, K., *J. Am. Chem. Soc.* **1994**, *116*, 1151. (d) Li, H.; Eddaoudi, M.; O'Keeffe, M.; Yaghi, O. M., *Nature* **1999**, *402*, 276. (e) Eddaoudi, M.; Moler, D. B.; Li, H.; Chen, B.; Reineke, T. M.; O'Keeffe, M.; Yaghi, O. M., *Acc. Chem. Res.* **2001**, *34*, 319. (f) Moulton, B.; Zaworotko, M. J., *Chem. Rev.* **2001**, *101*, 1629. (g) Eddaoudi, M.; Kim, J.; Rosi, N.; Vodak, D.; Wachter, J.; O'Keeffe, M.; Yaghi, O. M., *Science* **2002**, *295*, 469. (h) Kitagawa, S.; Kitaura, R.; Noro, S.-i., *Angew. Chem., Int. Ed.* **2004**, *43*, 2334. (i) Ferey, G., *Chem. Soc. Rev.* **2008**, *37*, 191. (j) Han, S.; Wei, Y.; Valente, C.; Forgan, R. S.; Gassensmith, J. J.; Smaldone, R. A.; Nakanishi, H.; Coskun, A.; Stoddart, J. F.; Grzybowski, B. A., *Angew. Chem. Int. Ed.* **2011**, *50*, 276. (k) Wei, Y.; Han, S.; Walker, D. A.; Fuller, P. E.; Grzybowski, B. A., *Angew. Chem. Int. Ed.* **2012**, *51*, 7435. (l) Bernini, M. C.; Jimenez, D. F.; Pasinetti, M.; Ramirez - Pastor, A. J.; Snurr, R. Q., *J. Mater. Chem. B* **2014**, *2*, 766. (m) Yoon, S. M.; Warren, S. C.; Grzybowski, B. A., *Angew. Chem. Int. Ed.* **2014**, *53*, 4437. (n) Fracaroli, A. M.; Furukawa, H.; Suzuki, M.; Dodd, M.; Okajima, S.; Gándara, F.; Reimer, J. A.; Yaghi, O. M., *J. Am. Chem. Soc.* **2014**, *136*, 8863. (o) Furukawa, H.; Mueller, U.; Yaghi, O. M., *Angew. Chem. Int. Ed.* **2015**, *54*, 3417. (p) Fei, H.; Cohen, S. M., *J. Am. Chem. Soc.* **2015**, *137*, 2191.

(2) (a) Dincă, M.; Yu, A. F.; Long, J. R., *J. Am. Chem. Soc.* **2006**, *128*, 8904. (b) Latroche, M.; Surblé, S.; Serre, C.; Mellot-Draznieks, C.; Llewellyn, P. L.; Lee, J.-H.; Chang, J.-S.; Jhung, S. H.; Férey, G., *Angew. Chem., Int. Ed.* **2006**, *45*, 8227. (c) Liu, Y.; Eubank, J. F.; Cairns, A. J.; Eckert, J.; Kravtsov, V. C.; Luebke, R.; Eddaoudi, M., *Angew. Chem., Int. Ed.* **2007**, *46*, 3278. (d) Murray, L. J.; Dinca, M.; Long, J. R., *Chem. Soc. Rev.* **2009**, *38*, 1294. (e) Farha, O. K.; Eryazici, I.; Jeong, N. C.; Hauser, B. G.; Wilmer, C. E.; Sarjeant, A. A.; Snurr, R. Q.; Nguyen, S. T.; Yazaydın, A. Ö.; Hupp, J. T., *J. Am. Chem. Soc.* **2012**, *134*, 15016. (f) Wang, H.; Cao, D., *J. Phys. Chem. C* **2015**, *119*, 6324. (g) Zhao, X.; Bu, X.; Zhai, Q. C.; Tran, H.; Feng, P., *J. Am. Chem. Soc.* **2015**, *137*, 1396.

(3) (a) Fletcher, A. J.; Thomas, K. M.; Rosseinsky, M. J., *J. Solid State Chem.* **2005**, *178*, 2491. (b) Matsuda, R.; Kitaura, R.; Kitagawa, S.; Kubota, Y.; Belosludov, R. V.; Kobayashi, T. C.; Sakamoto, H.; Chiba, T.; Takata, M.; Kawazoe, Y.; Mita, Y., *Nature* **2005**, *436*, 238. (c) Hayashi, H.; Cote, A. P.; Furukawa, H.; O/'Keeffe, M.; Yaghi, O. M., *Nature Mater.* **2007**, *6*, 501. (d) Keskin, S.; Sholl, D. S., *J. Phys. Chem. C* **2007**, *111*, 14055. (e) Li, B.; Wen, H.-M.; Wang, H.;

Wu, H.; Tyagi, M.; Yildirim, T.; Zhou, W.; Chen, B., *J. Am. Chem. Soc.* **2014**, *136*, 6207. (f) Hu, J.; Sun, T.; Ren, X.; Wang, S., *Micropor. Mesopor. Mater.* **2015**, *204*, 73.

(4) (a) Demessence, A.; D'Alessandro, D. M.; Foo, M. L.; Long, J. R., *J. Am. Chem. Soc.* **2009**, *131*, 8784. (b) Zheng, B.; Bai, J.; Duan, J.; Wojtas, L.; Zaworotko, M. J., *J. Am. Chem. Soc.* **2010**, *133*, 748. (c) Goeppert, A.; Czaun, M.; Surya Prakash, G. K.; Olah, G. A., *Energy & Environ. Sci.* **2012**, *5*, 7833. (d) Yang, S.; Lin, X.; Lewis, W.; Suyetin, M.; Bichoutskaia, E.; Parker, J. E.; Tang, C. C.; Allan, D. R.; Rizkallah, P. J.; Hubberstey, P.; Champness, N. R.; Mark Thomas, K.; Blake, A. J.; Schröder, M., *Nature Mater.* **2012**, *11*, 710. (e) Beyzavi, M. H.; Klet, R. C.; Tussupbayev, S.; Borycz, J.; Vermeulen, N. A.; Cramer, C. J.; Stoddart, J. F.; Hupp, J. T.; Farha, O. K., *J. Am. Chem. Soc.* **2014**, *136*, 15861. (f) Gassensmith, J. J.; Kim, J. Y.; Holcroft, J. M.; Farha, O. K.; Stoddart, J. F.; Hupp, J. T.; Jeong, N. C., *J. Am. Chem. Soc.* **2014**, *136*, 8277. (g) Sato, H.; Kosaka, W.; Matsuda, R.; Hori, A.; Hijikata, Y.; Belosludov, R. V.; Sakaki, S.; Takata, M.; Kitagawa, S., *Science* **2014**, *343*, 167. (h) Al-Maythalony, B. A.; Shekhah, O.; Swaiden, R.; Belmabkhout, Y.; Pinnau, I.; Eddaoudi, M., *J. Am. Chem. Soc.* **2015**, *137*, 1754.

(5) (a) Maes, M.; Alaerts, L.; Vermoortele, F.; Ameloot, R.; Couck, S.; Finsy, V.; Denayer, J. F. M.; De Vos, D. E., *J. Am. Chem. Soc.* **2010**, *132*, 2284. (b) Herm, Z. R.; Wiers, B. M.; Mason, J. A.; van Baten, J. M.; Hudson, M. R.; Zajdel, P.; Brown, C. M.; Masciocchi, N.; Krishna, R.; Long, J. R., *Science* **2013**, *340*, 960.

(6) (a) Bradshaw, D.; Prior, T. J.; Cussen, E. J.; Claridge, J. B.; Rosseinsky, M. J., *J. Am. Chem. Soc.* **2004**, *126*, 6106. (b) Vaidhyanathan, R.; Bradshaw, D.; Rebilly, J.-N.; Barrio, J. P.; Gould, J. A.; Berry, N. G.; Rosseinsky, M. J., *Angew. Chem., Int. Ed.* **2006**, *45*, 6495. (c) Nuzhdin, A. L.; Dybtsev, D. N.; Bryliakov, K. P.; Talsi, E. P.; Fedin, V. P., *J. Am. Chem. Soc.* **2007**, *129*, 12958. (d) Liu, Y.; Xuan, W.; Cui, Y., *Adv. Mater.* **2010**, *22*, 4112. (e) Padmanaban, M.; Muller, P.; Lieder, C.; Gedrich, K.; Grunker, R.; Bon, V.; Senkovska, I.; Baumgartner, S.; Opelt, S.; Paasch, S.; Brunner, E.; Glorius, F.; Klemm, E.; Kaskel, S., *Chem. Commun.* **2011**, *47*, 12089. (f) Das, M. C.; Guo, Q.; He, Y.; Kim, J.; Zhao, C.-G.; Hong, K.; Xiang, S.; Zhang, Z.; Thomas, K. M.; Krishna, R.; Chen, B., *J. Am. Chem. Soc.* **2012**, *134*, 8703. (g) Wang, W.; Dong, X.; Nan, J.; Jin, W.; Hu, Z.; Chen, Y.; Jiang, J., *Chem. Commun.* **2012**, *48*, 7022. (h) Kuang, X.; Ma, Y.; Su, H.; Zhang, J.; Dong, Y.-B.; Tang, B., *Anal. Chem.* **2013**, *86*, 1277.

(7) (a) Mueller, U.; Schubert, M.; Teich, F.; Puetter, H.; Schierle-Arndt, K.; Pastre, J., *J. Mater. Chem.* **2006**, *16*, 626. (b) Li, J.-R.; Kuppler, R. J.; Zhou, H.-C., *Chem. Soc. Rev.* **2009**, *38*, 1477. (c) Jiang, H.-L.; Xu, Q., *Chem. Commun.* **2011**, *47*, 3351. (d) Lee, C. Y.; Bae, Y.-S.; Jeong, N. C.; Farha, O. K.; Sarjeant, A. A.; Stern, C. L.; Nickias, P.; Snurr, R. Q.; Hupp, J. T.; Nguyen, S.

T., *J. Am. Chem. Soc.* **2011**, *133*, 5228. (e) Bloch, E. D.; Queen, W. L.; Krishna, R.; Zadrozny, J. M.; Brown, C. M.; Long, J. R., *Science* **2012**, *335*, 1606. (f) He, Y.; Zhang, Z.; Xiang, S.; Fronczek, F. R.; Krishna, R.; Chen, B., *Chem. Commun.* **2012**, *48*, 6493.

(8) Keskin, S.; Kızılel, S., *Ind. Eng. Chem. Res.* **2011**, *50*, 1799.

(9) (a) Hulme, R.; Rosensweig, R. E.; Ruthven, D. M., *Ind. Eng. Chem. Res.* **1991**, *30*, 752. (b) Cottier, V.; Bellat, J.-P.; Simonot-Grange, M.-H.; Méthivier, A., *J. Phys. Chem. B* **1997**, *101*, 4798. (c) Kulprathipanja, S. J., James R. B., *Zeolites in Industrial Separation*. Wiley - VCH, Weinheim: **2010**. (d) Jee, S. E.; Sholl, D. S., *J. Am. Chem. Soc.* **2009**, *131*, 7896.

(10) (a) Cheremisinoff, P. N., Ellerbush F., *Carbon Adsorption Handbook*. Ann Arbor Science Publishers, Science, Michigan: **1978**. (b) Mattson, J. S. M., Mark, H.B., *Activated Carbon*. Marcel Dekker, New York: **1971**.

(11) (a) Ferey, G.; Serre, C., *Chem. Soc. Rev.* **2009**, *38*, 1380. (b) O'Keeffe, M., *Chem. Soc. Rev.* **2009**, *38*, 1215.

(12) (a) Minceva, M.; Rodrigues, A. E., *AIChE J.* **2007**, *53*, 138. (b) Othmer, K., *Separation Technology, 2 Volume Set, 2nd Edition*. Wiley, Hoboken, New Jersey: **2008**; Vol. 1.

(13) (a) Broughton, D. B.; Gerhold, C. G., Patent: US2985589, **1961**. (b) Eccli, W. D.; Fremuth, A. D. S., Patent: US5498822A, **1996**. (c) Lima, R. M.; Grossmann, I. E., *AIChE J.* **2009**, *55*, 354.

(14) Minceva, M.; Rodrigues, A. E., *Chem. Eng. Res. Des.* **2004**, *82*, 667.

(15) (a) Lindley, J.; McLeod, A. J., Patent: US3959978A, **1976**. (b) Hubbell, D. S.; Rutten, P. W. M., Patent: US5811629A, **1998**.

(16) Lusi, M.; Barbour, L. J., *Angew. Chem., Int. Ed.* **2012**, *51*, 3928.

(17) (a) Tozawa, T.; Jones, J. T. A.; Swamy, S. I.; Jiang, S.; Adams, D. J.; Shakespeare, S.; Clowes, R.; Bradshaw, D.; Hasell, T.; Chong, S. Y.; Tang, C.; Thompson, S.; Parker, J.; Trewin, A.; Bacsa, J.; Slawin, A. M. Z.; Steiner, A.; Cooper, A. I., *Nature Mater.* **2009**, *8*, 973. (b) Mitra, T.; Jelfs, K. E.; Schmidtmann, M.; Ahmed, A.; Chong, S. Y.; Adams, D. J.; Cooper, A. I., *Nature Chem.* **2013**, *5*, 276.

(18) (a) Munch, A. S.; Mertens, F. O. R. L., *J. Mater. Chem.* **2012**, *22*, 10228. (b) Sarkisov, L., *Phys. Chem. Chem. Phys.* **2012**, *14*, 15438.

(19) Luebbers, M. T.; Wu, T.; Shen, L.; Masel, R. I., *Langmuir* **2010**, *26*, 11319.

(20) Alaerts, L.; Kirschhock, C. E. A.; Maes, M.; van der Veen, M. A.; Finsy, V.; Depla, A.; Martens, J. A.; Baron, G. V.; Jacobs, P. A.; Denayer, J. F. M.; De Vos, D. E., *Angew. Chem., Int. Ed.* **2007**, *46*, 4293.

(21) Alaerts, L.; Maes, M.; Giebeler, L.; Jacobs, P. A.; Martens, J. A.; Denayer, J. F. M.; Kirschhock, C. E. A.; De Vos, D. E., *J. Am. Chem. Soc.* **2008**, *130*, 14170.

(22) Alaerts, L.; Maes, M.; Jacobs, P. A.; Denayer, J. F. M.; De Vos, D. E., *Phys. Chem. Chem. Phys.* **2008**, *10*, 2979.

(23) Maes, M.; Vermoortele, F.; Boulhout, M.; Boudewijns, T.; Kirschhock, C.; Ameloot, R.; Beurroies, I.; Denoyel, R.; De Vos, D. E., *Micropor. Mesopor. Mater.* **2012**, *157*, 82.

(24) Remy, T.; Ma, L.; Maes, M.; De Vos, D. E.; Baron, G. V.; Denayer, J. F. M., *Ind. Eng. Chem. Res.* **2012**, *51*, 14824.

(25) El Osta, R.; Carlin-Sinclair, A.; Guillou, N.; Walton, R. I.; Vermoortele, F.; Maes, M.; de Vos, D.; Millange, F., *Chem. Mater.* **2012**, *24*, 2781.

(26) Vermoortele, F.; Maes, M.; Moghadam, P. Z.; Lennox, M. J.; Ragon, F.; Boulhout, M.; Biswas, S.; Laurier, K. G. M.; Beurroies, I.; Denoyel, R.; Roeffaers, M.; Stock, N.; Düren, T.; Serre, C.; De Vos, D. E., *J. Am. Chem. Soc.* **2011**, *133*, 18526.

(27) Torres-Knoop, A.; Krishna, R.; Dubbeldam, D., *Angew. Chem., Int. Ed.* **2014**, *53*, 7774.

(28) Warren, J. E.; Perkins, C. G.; Jelfs, K. E.; Boldrin, P.; Chater, P. A.; Miller, G. J.; Manning, T. D.; Briggs, M. E.; Stylianou, K. C.; Claridge, J. B.; Rosseinsky, M. J., *Angew. Chem., Int. Ed.* **2014**, *53*, 4592.

(29) (a) Bender. M. L.; Komiyama, M., *Cyclodextrin Chemistry*. Springer-Verlag, New York: **1978**. (b) Tamaki, T.; Kokubu, T., *J. Incl. Phenom. Macrocyclic Chem.* **1984**, *2*, 815. (c) Harada, A.; Li, J.; Kamachi, M., *Macromolecules* **1993**, *26*, 5267. (d) Harada, A.; Li, J.; Kamachi, M., *Nature* **1994**, *370*, 126. (e) Wenz, G., *Angew. Chem., Int. Ed. Engl.* **1994**, *33*, 803. (f) Vajda, S.; Jimenez, R.; Rosenthal, S. J.; Fidler, V.; Fleming, G. R.; Castner, E. W., *J. Chem. Soc. Faraday Trans.* **1995**, *91*, 867. (g) Rekharsky, M. V.; Inoue, Y., *Chem. Rev.* **1998**, *98*, 1875. (h) Takei, M.; Yui, H.; Hirose, Y.; Sawada, T., *J. Phys. Chem. A* **2001**, *105*, 11395. (i) Douhal, A., *Chem. Rev.* **2004**, *104*, 1955. (j) Ikeda, H.; Nihei, T.; Ueno, A., *J. Org. Chem.* **2005**, *70*, 1237. (k) Ke, C.; Yang, C.; Mori, T.; Wada, T.; Liu, Y.; Inoue, Y., *Angew. Chem., Int. Ed.* **2009**, *48*, 6675. (l) Wang, H. M.; Wenz, G., *Chem. Asian J.* **2011**, *6*, 2390. (m) Wang, H. M.; Wenz, G., *Beilstein J. Org. Chem.* **2012**, *8*, 1644. (n) Liu, Z.; Stoddart, J. F., *Pure Appl. Chem.* **2014**, 86, 1323.

(30) Smaldone, R. A.; Forgan, R. S.; Furukawa, H.; Gassensmith, J. J.; Slawin, A. M. Z.; Yaghi, O. M.; Stoddart, J. F., *Angew. Chem., Int. Ed.* **2010**, *49*, 8630.

(31) Forgan, R. S.; Smaldone, R. A.; Gassensmith, J. J.; Furukawa, H.; Cordes, D. B.; Li, Q.; Wilmer, C. E.; Botros, Y. Y.; Snurr, R. Q.; Slawin, A. M. Z.; Stoddart, J. F., *J. Am. Chem. Soc.* **2011**, *134*, 406.

(32) Furukawa, Y.; Ishiwata, T.; Sugikawa, K.; Kokado, K.; Sada, K., *Angew. Chem., Int. Ed.* **2012**, *51*, 10566.

(33) (a) Cole, J. H.; Everett, D. H.; Marshall, C. T.; Paniego, A. R.; Powl, J. C.; Rodriguez-Reinoso, F., *J. Chem. Soc. Faraday Trans.* **1974**, *70*, 2154. (b) Reid, C. R.; Thomas, K. M., *J. Phys. Chem. B* **2001**, *105*, 10619. (c) Bell, J. G.; Zhao, X.; Uygur, Y.; Thomas, K. M., *J. Phys. Chem. C* **2011**, *115*, 2776. (d) Crank, J., *The mathematics of diffusion*; 2nd ed.; Clarendon Press: Oxford, **1975**. (e) Glueckauf, E.; Coates, J. I., *J. Chem. Soc.* **1947**, 1315. (f) Glueckauf, E., *Trans. Faraday Soc.* **1955**, *51*, 1540. (g) Loughlin, K. F.; Hassan, M. M.; Fatehi, A. I.; Zahur, M., *Gas Sep. Purif.* **1993**, *7*, 264. (h) Webster, C. E.; Drago, R. S.; Zerner, M. C., *J. Am. Chem. Soc.* **1998**, *120*, 5509. (i) Li, L. J.; Bell, J. G.; Tang, S. F.; Lv, X. X.; Wang, C.; Xing, Y. L.; Zhao, X. B.; Thomas, K. M., *Chem. Mat.* **2014**, *26*, 4679. (j) Wang, C.; Li, L.; Bell, J. G.; Lv, X. X.; Tang, S.; Zhao, X. B.; Thomas, K. M., *Chem. Mater* **2015**, *27*, 1502.

(34) Lucena, S. M. P.; Snurr, R. Q.; Cavalcante Jr., C. L., *Adsorption* **2007**, *13*, 477.

Table 1. CD-MOF-1 Particle Size Ranges with Varying CTAB Concentrations

Material	CTAB / mg	Particle Size / μm	Image
CD-MOF-1-Micro1	20	25	2a / S2a
CD-MOF-1-Micro2	40	10–15	2b / S2b
CD-MOF-1-Micro3	60	5–15	2c / S2c
CD-MOF-1-Micro4	80	1–10	2d / S2d

Table 2. CD-MOF Column Separation Factors of 50 mg mL^{-1} Xylene Mixtures in HPLC-grade Hexane at a Flow Rate of 1 mL min^{-1}

Adsorbent	Solvent		*j*		
		i	*ortho*-Xylene	*meta*-Xylene	*para*-Xylene
CD-MOF-2	Hexane	*ortho*-Xylene	–	4.76	16.37
Top-down		*meta*-Xylene	0.21	–	3.44
Column		*para*-Xylene	0.06	0.29	–
CD-MOF-1	Hexane	*ortho*-Xylene	–	6.73	17.93
Bottom-up		*meta*-Xylene	0.15	–	2.67
Column		*para*-Xylene	0.06	0.38	–
CD-MOF-1	Pure	*ortho*-Xylene	–	5.72	10.76
Bottom-up	Xylene	*meta*-Xylene	0.17	–	1.88
Column	Mixture	*para*-Xylene	0.09	0.53	–

Table 3. Separation Factors of Known Frameworks Taken from the Literature for the Three Xylene Isomers and Ethylbenzene

Adsorbent	Solvent		*j*				
		i	*ortho*-Xylene	*meta*-Xylene	*para*-Xylene	Ethyl-benzene	Ref.
HKUST-1 [$Cu_3(BTC)_2$]	Hexane	*ortho*-Xylene	–	0.4	0.7	0.7	[20]
		meta-Xylene	2.4	–	1.1	1.4	
		para-Xylene	1.4	0.9	–	1.2	
		Ethyl-benzene	1.4	0.7	0.8	–	
MIL-47	Hexane	*ortho*-Xylene	–	2.0	1.4	10.9	[21]
		meta-Xylene	0.5	–	0.4	4.2	
		para-Xylene	0.7	2.9	–	9.7	
		Ethyl-benzene	0.1	0.2	0.1	–	
MIL-53(Al)	Hexane	*ortho*-Xylene	–	2.7	3.5	10.9	[20-21]
		meta-Xylene	0.4	–	1.2	3.8	
		para-Xylene	0.3	0.8	–	3.1	
		Ethyl-benzene	0.1	0.3	0.3	–	
MIL-53(Fe)	Heptane	*ortho*-Xylene	–	1.3	3.5	12.3	[25]
		meta-Xylene	0.7	–	2.5	9.2	
		para-Xylene	0.3	0.4	–	3.5	
		Ethyl-benzene	0.1	0.1	0.3	–	

Table 4. Activated Bottom-up CD-MOF Column Separation Factors of 50 mg mL^{-1} BTEX Mixtures in HPLC-grade Hexane at a Flow Rate of 1 mL min^{-1}

Adsorbent		*j*					
	i	*ortho*-Xylene	*meta*-Xylene	*para*-Xylene	Benzene	Toluene	Ethylbenzene
CD-MOF-1 Bottom-up Column	*ortho*-Xylene	–	6.68	11.26	0.76	1.61	4.75
	meta-Xylene	0.15	–	1.69	0.11	0.24	0.71
	para-Xylene	0.09	0.59	–	0.07	0.14	0.42
	Benzene	1.32	8.82	14.88	–	2.13	6.27
	Toluene	0.62	4.14	6.98	0.47	–	2.94
	Ethylbenzene	0.21	1.41	2.37	0.21	0.34	–

Table 5. Bottom-up CD-MOF-1 Column Separation Factors of 50 mg mL^{-1} Mixtures of *para*-, *meta*- and *ortho*-Ethyltoluene in HPLC-grade Hexane at 1 mL min^{-1}

Adsorbent	Solvent		*j*		
		i	*para*-Ethyltoluene	*meta*-Ethyltoluene	*ortho*-Ethyltoluene
CD-MOF-1	Hexane	*para*-Ethyltoluene	–	0.47	0.07
Bottom-up		*meta*-Ethyltoluene	2.10	–	0.15
Column		*ortho*-Ethyltoluene	13.77	6.56	–

Captions to Figures

Figure 1. Representations of the solid-state structure of CD-MOF-1. **(a)** A space-filling representation, viewed along the <1 0 0> axis, revealing the extended structure of the body-centered cubic packing arrangement in CD-MOF-1 (C-light grey, O red, K purple). Note that CD-MOF-2 has an identical extended structure but with Rb^+ instead of K^+ ions. **(b)** A space-filling representation of CD-MOF-1, viewed along the <1 1 1> axis, revealing the triangular windows. The large cavities are filled will yellow spheres. **(c)** The cuboidal topology of the $(\gamma\text{-CD})_6$ units, viewed along the <1 1 1>, where each γ-CD is represented as a space-filling display in a contrasting color. **(d)** Illustration of the pore void within CD-MOF-1, viewed along the <1 1 1> axis, where the void is colored purple and the atoms of CD-MOF-1 are removed for the sake of clarity.

Figure 2. Representations scanning electron micrographs (SEMs) of CD-MOF-1 particles crystallized in the presence of **(a)** 20 mg, **(b)** 40 mg, **(c)** 60 mg, **(d)** 80 mg of CTAB.

Figure 3. Liquid-phase chromatographic separations using CD-MOFs as the stationary phase. CD-MOF Column separations of 50 mg mL^{-1} xylene mixtures in HPLC-grade hexane at a flow rate of 1 mL min^{-1} at 298 K. **(a)** Top-down CD-MOF-2 column (particle size 10 – 37 μm). **(b)** Bottom-up CD-MOF-1 column (particle size 10 – 15 μm). The separation profiles display the assignment of the elution order from a mixture (**red**) of xylene isomers and pure-components of *para*- (**black**), *meta*- (**green**) and *ortho*-xylene (**blue**). **(c)** Bottom-up CD-MOF-1 column (particle size 10–15 μm) where the separation profiles display the assignment of the elution order from the mixture **(red)** of ethyltoluene isomers, and pure-components of *para*- **(black)**, *meta*- **(green)** and *ortho*-ethyltoluene **(blue)**. **(d)** The separation profile of, *para*- **(black)**, *meta*- **(green)** and *ortho*-cymene **(blue)**.

Figure 4. Bottom-up CD-MOF-1 column (particle size 10 – 15 µm) separations of 50 mg mL^{-1} BTX and BTEX mixtures in HPLC-grade hexane at a flow rate of 1 mL min^{-1} at 298 K. BTX after activating the column for **(a)** 4 h, **(b)** 30 h, **(c)** 60 h. **(d)** BTEX after activating the column for 30 h, **(e)** BTEX after deactivating the column using hexane:^{i}PrOH (98/2, v/v) and **(f)** BTEX after reactivation using CH_2Cl_2.

Figure 5. Vapor-phase xylene static adsorption experiments on CD-MOF-2 at 333 K. **(a)** Adsorption isotherms for *para*- **(black)**, *meta*- **(green)** and *ortho*-xylene **(blue). (b)** Diffusion coeffecients for Fickian **(filled)**, CBRD **(half-filled)** and LDF **(empty)** mechanisms as a function of pressure for *para*- **(black)**, *meta*- **(green)** and *ortho*-xylene **(blue)** adsorption on CD-MOF-2.

Figure 6. Vapor-phase xylene breakthrough experiments on CD-MOF-2. **(a)** Concentration plot and **(b)** the blown-up plot of the initial breakthrough region between 390–410 min for *para*- **(black)**, *meta*- **(green)** and *ortho*-xylene **(blue). (c)** Molecular simulation of the pure-component adsorption isotherms for the xylene isomers within the CD-MOF-2 framework. Simulated adsorption isotherms for 50 / 50 binary mixtures of **(d)** *para*-/*meta*-, **(e)** *para*-/*ortho*- and **(f)** *meta*-/*ortho*-xylene.

Figure 7. Molecular simulation snapshots of the xylene isomers within the CD-MOF-2 framework viewed down the <1 0 0> axis. With *para*- **(black)**, *meta*- **(green)**, *ortho*-xylene **(blue)** and their corresponding methyl-groups colored **(yellow)** for the sake of clarity.

Figure 8. Molecular simulation snapshots of the xylene isomers within the CD-MOF-2 framework viewed down the <1 0 0> axis. Equimolar mixture snapshots of xylene isomers **(a)** *meta*-/*para*-, **(b)** *ortho*-/*meta*- and **(c)** *ortho*-/*para*-xylene. With *para*- **(black)**, *meta*- **(green)**, *ortho*-xylene **(blue)** and their corresponding methyl-groups colored **(yellow)** for the sake of clarity.

Figure 9. Interaction energies for the xylene isomers for three different orientations of **(a)** 90°, **(b)** 45° and **(c)** 0° with respect to the γ-CD ring. The schematics show the scanned energy path for each orientation.

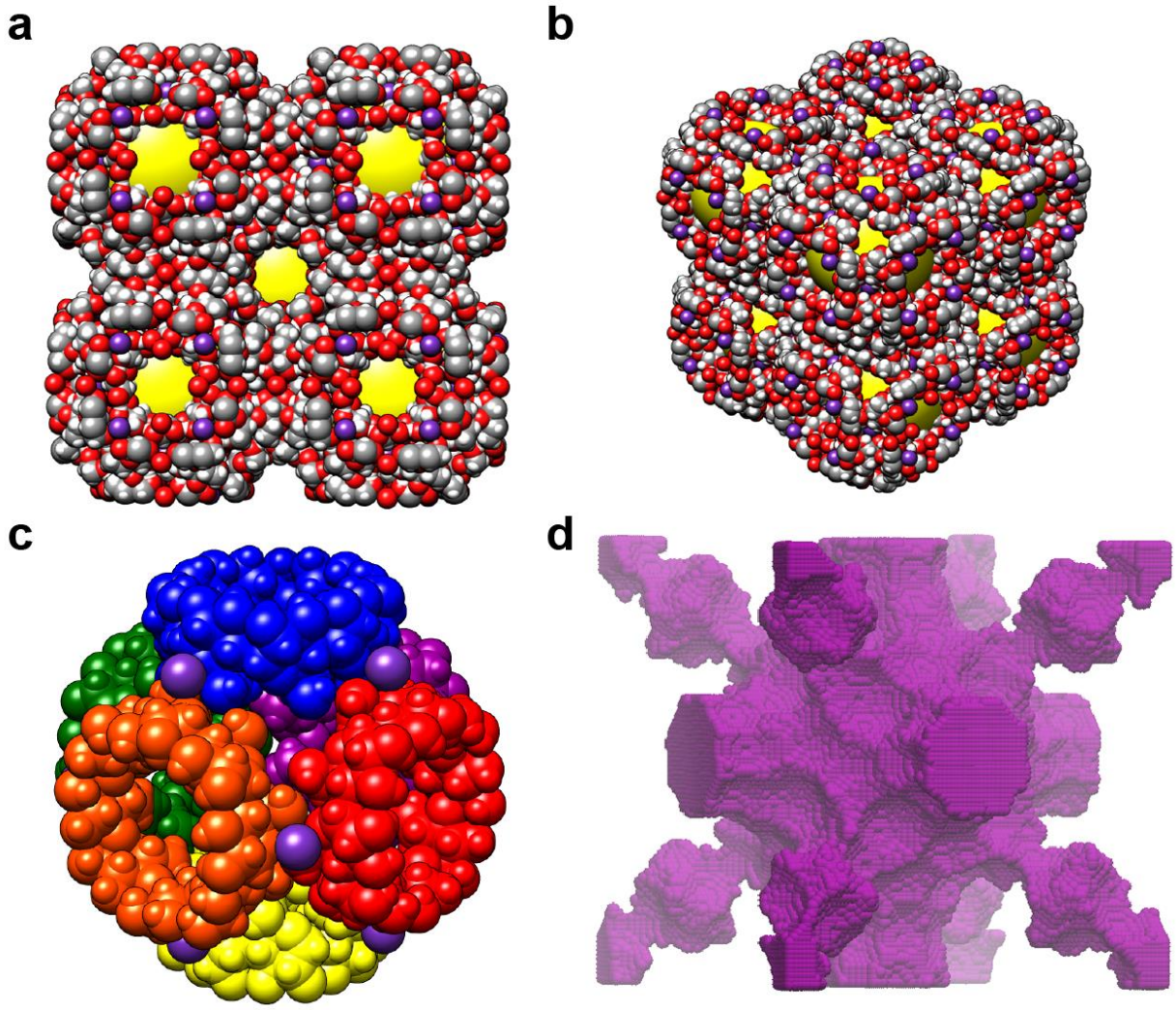

Figure 1

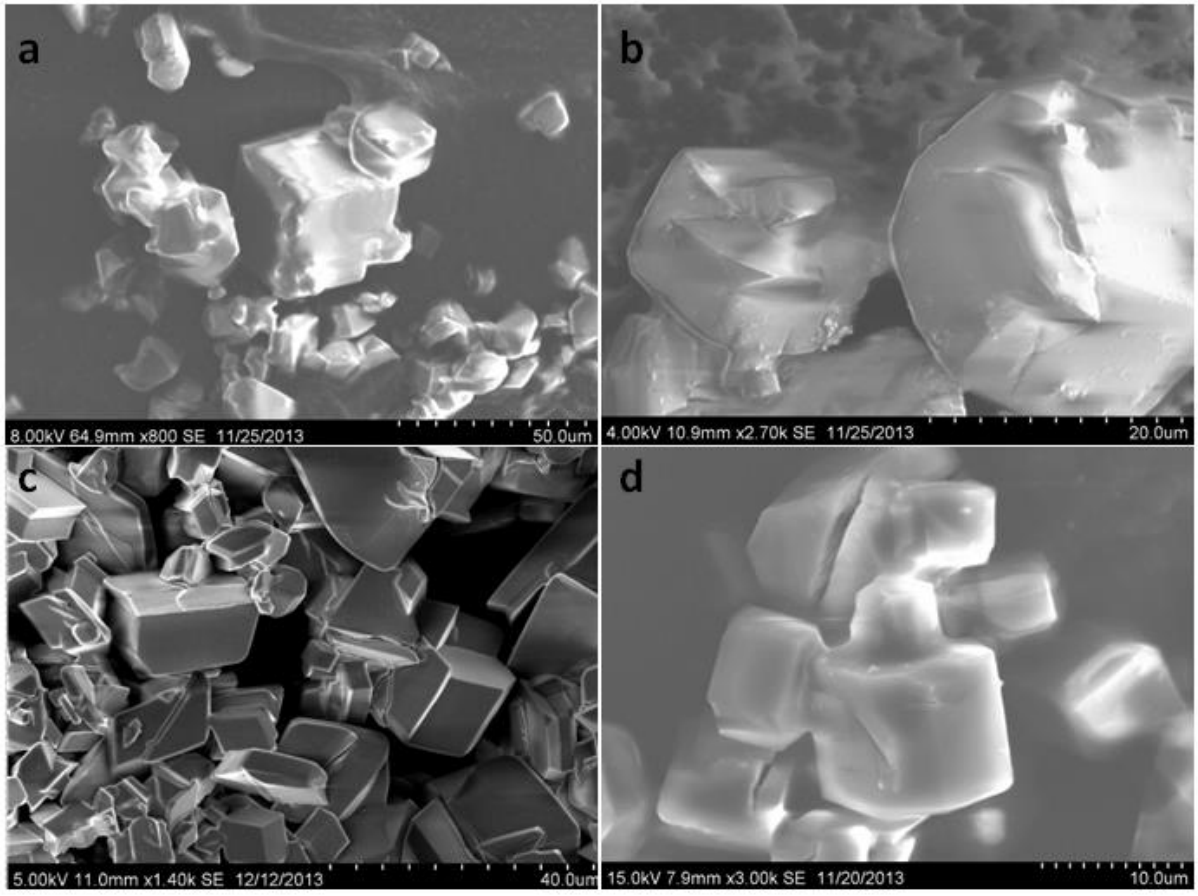
a
8.00kV 64.9mm x800 SE 11/25/2013
50.0um
b
4.00kV 10.9mm x2.70k SE 11/25/2013
20.0um
c
5.00kV 11.0mm x1.40k SE 12/12/2013
40.0um
d
15.0kV 7.9mm x3.00k SE 11/20/2013
10.0um

Figure 2

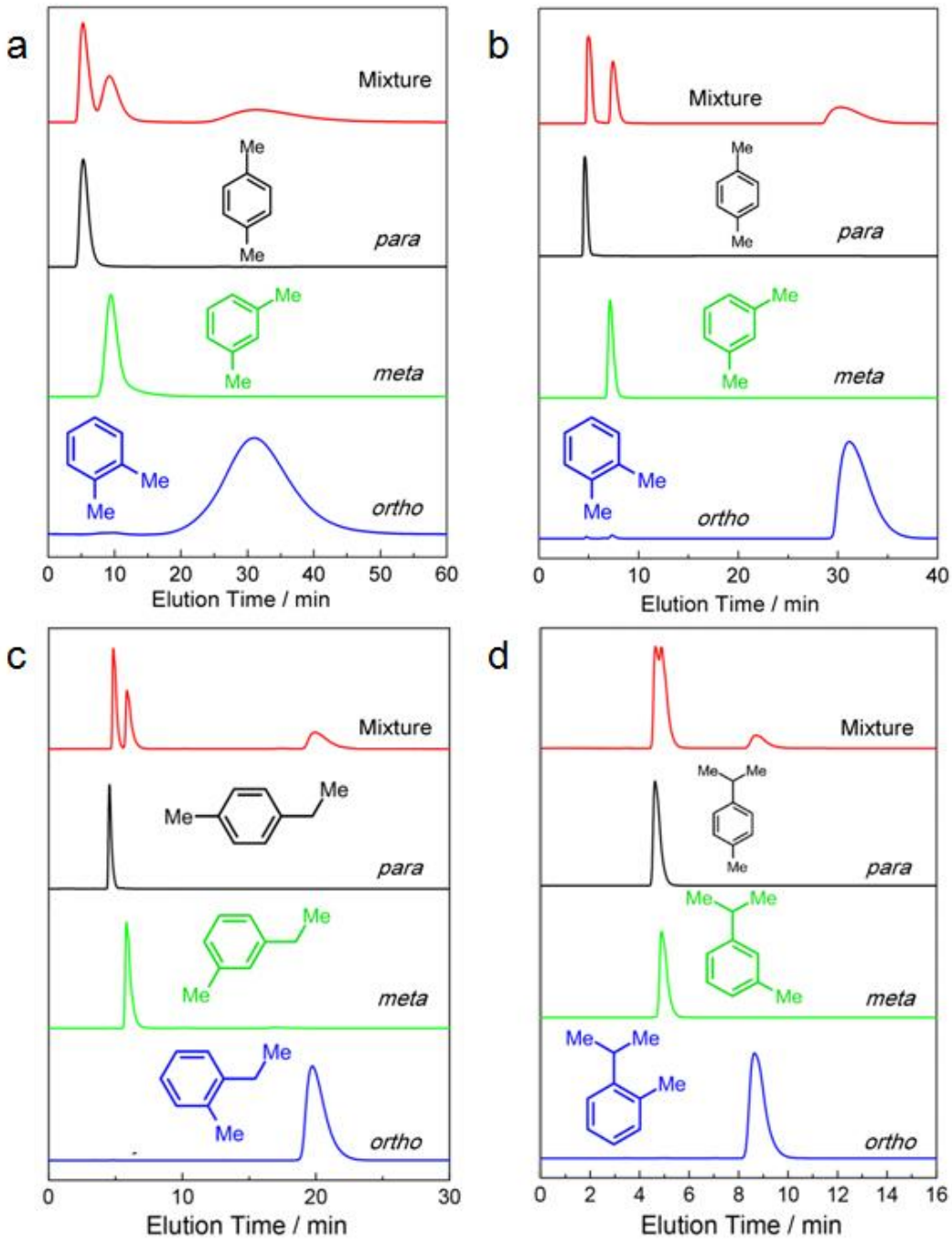
a
Mixture
para
meta
ortho
0 10 20 30 40 50 60
Elution Time / min
b
Mixture
para
meta
ortho
0 10 20 30 40
Elution Time / min
c
Mixture
para
meta
ortho
0 10 20 30
Elution Time / min
d
Mixture
para
meta
ortho
0 2 4 6 8 10 12 14 16
Elution Time / min

Figure 3

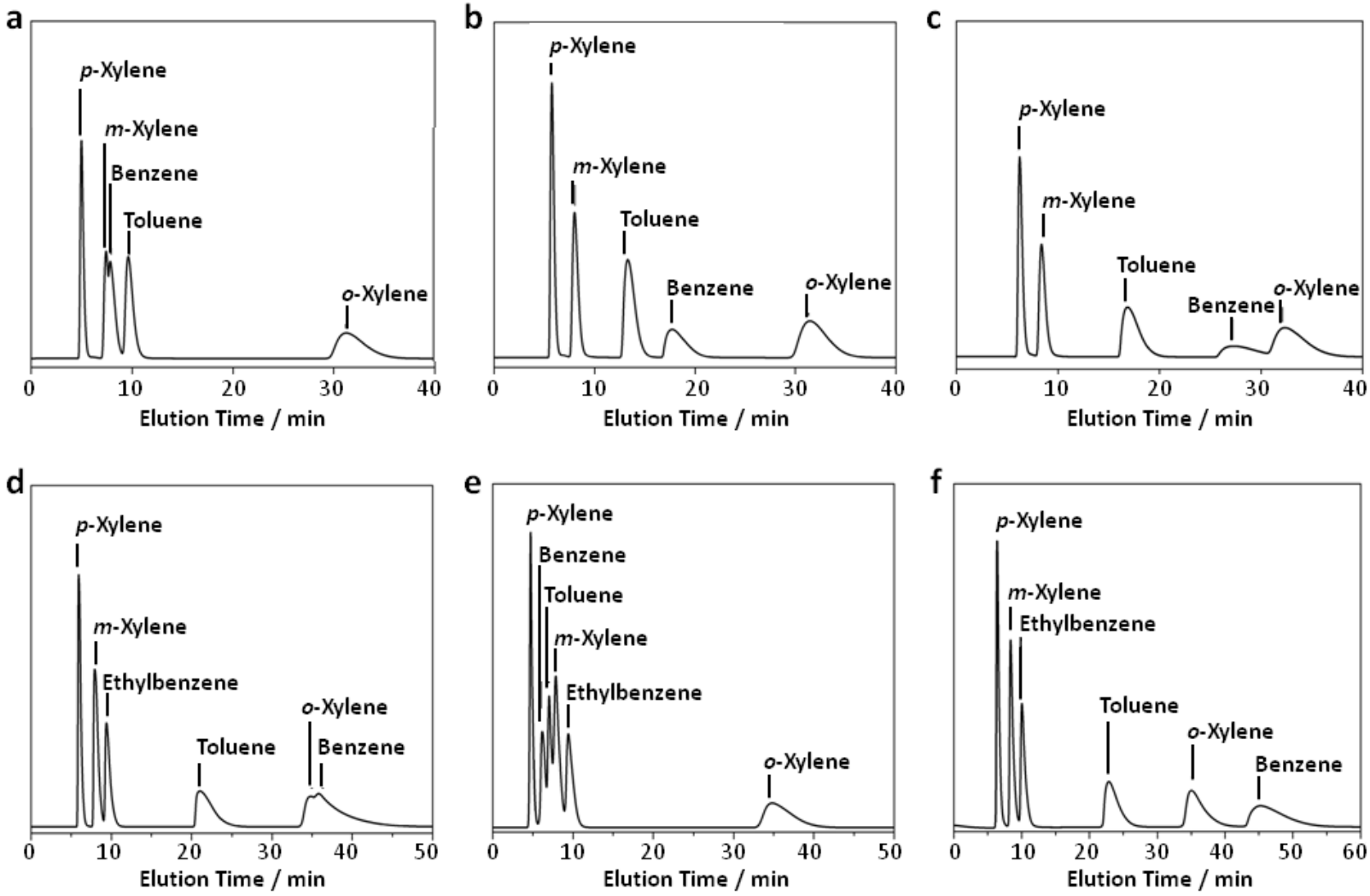
a
p-Xylene
m-Xylene
Benzene
Toluene
o-Xylene
0 10 20 30 40
Elution Time / min
b
p-Xylene
m-Xylene
Toluene
Benzene
o-Xylene
0 10 20 30 40
Elution Time / min
c
p-Xylene
m-Xylene
Toluene
Benzene
o-Xylene
0 10 20 30 40
Elution Time / min
d
p-Xylene
m-Xylene
Ethylbenzene
Toluene
o-Xylene
Benzene
0 10 20 30 40 50
Elution Time / min
e
p-Xylene
Benzene
Toluene
m-Xylene
Ethylbenzene
o-Xylene
0 10 20 30 40 50
Elution Time / min
f
p-Xylene
m-Xylene
Ethylbenzene
Toluene
o-Xylene
Benzene
0 10 20 30 40 50 60
Elution Time / min

Figure 4

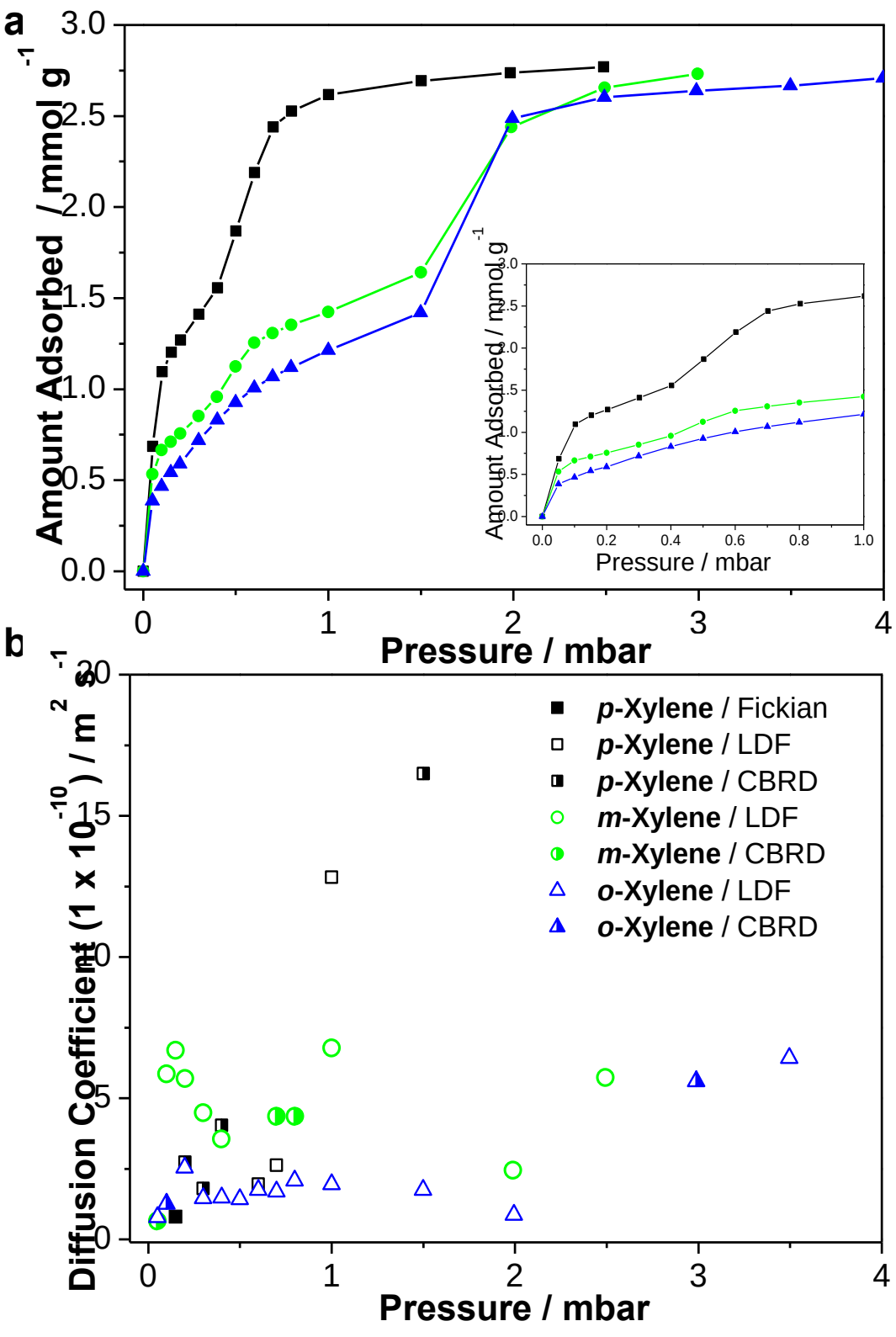
a
Amount Adsorbed / mmol g-1
Pressure / mbar
Amount Adsorbed / mmol g-1
Pressure / mbar
b
Diffusion Coefficient (1 x 10-10) / m2 s-1
Pressure / mbar
p-Xylene / Fickian
p-Xylene / LDF
p-Xylene / CBRD
m-Xylene / LDF
m-Xylene / CBRD
o-Xylene / LDF
o-Xylene / CBRD

Figure 5

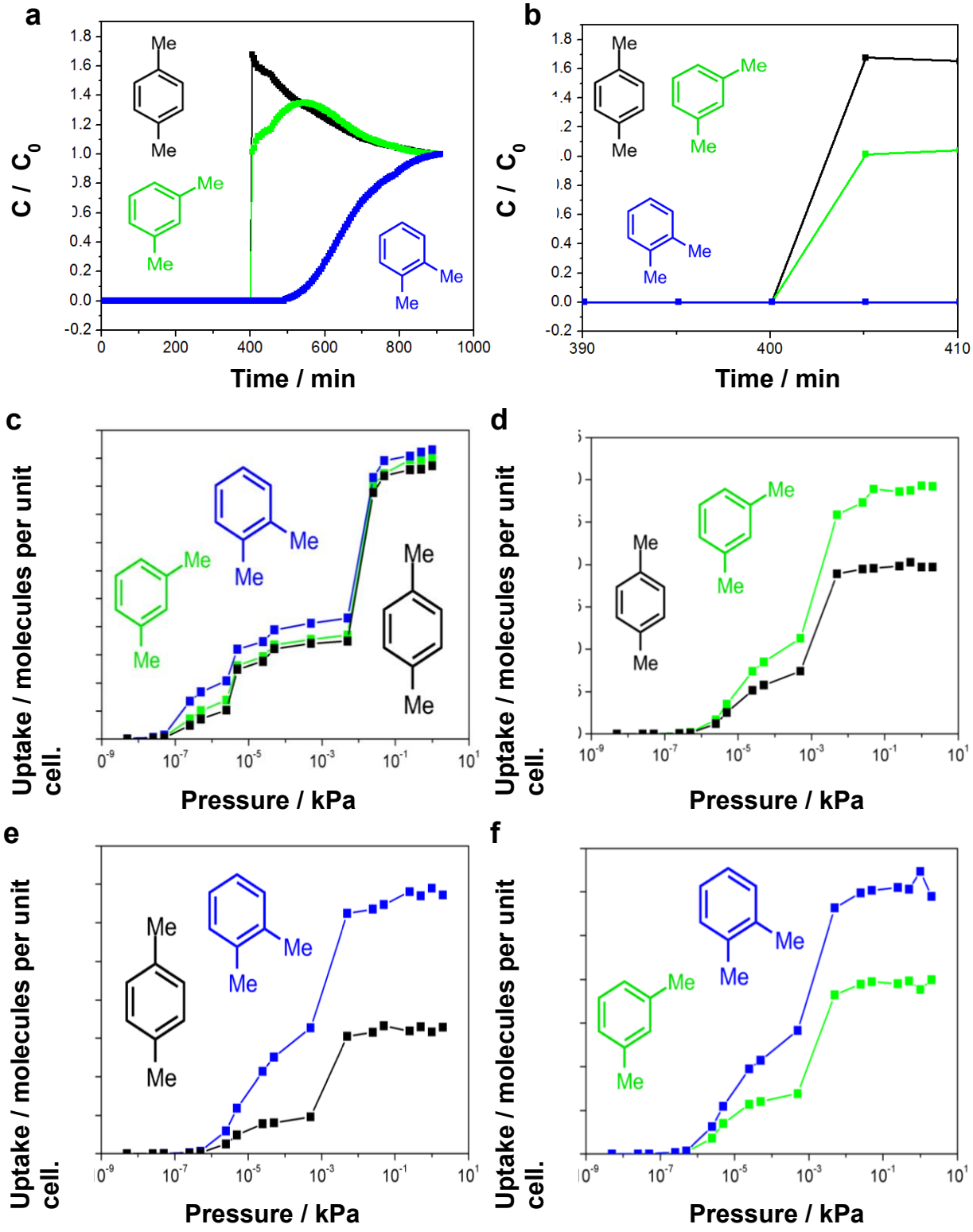
a
b
c
d
e
f
C / C0
Time / min
Uptake / molecules per unit cell.
Pressure / kPa
Me

Figure 6

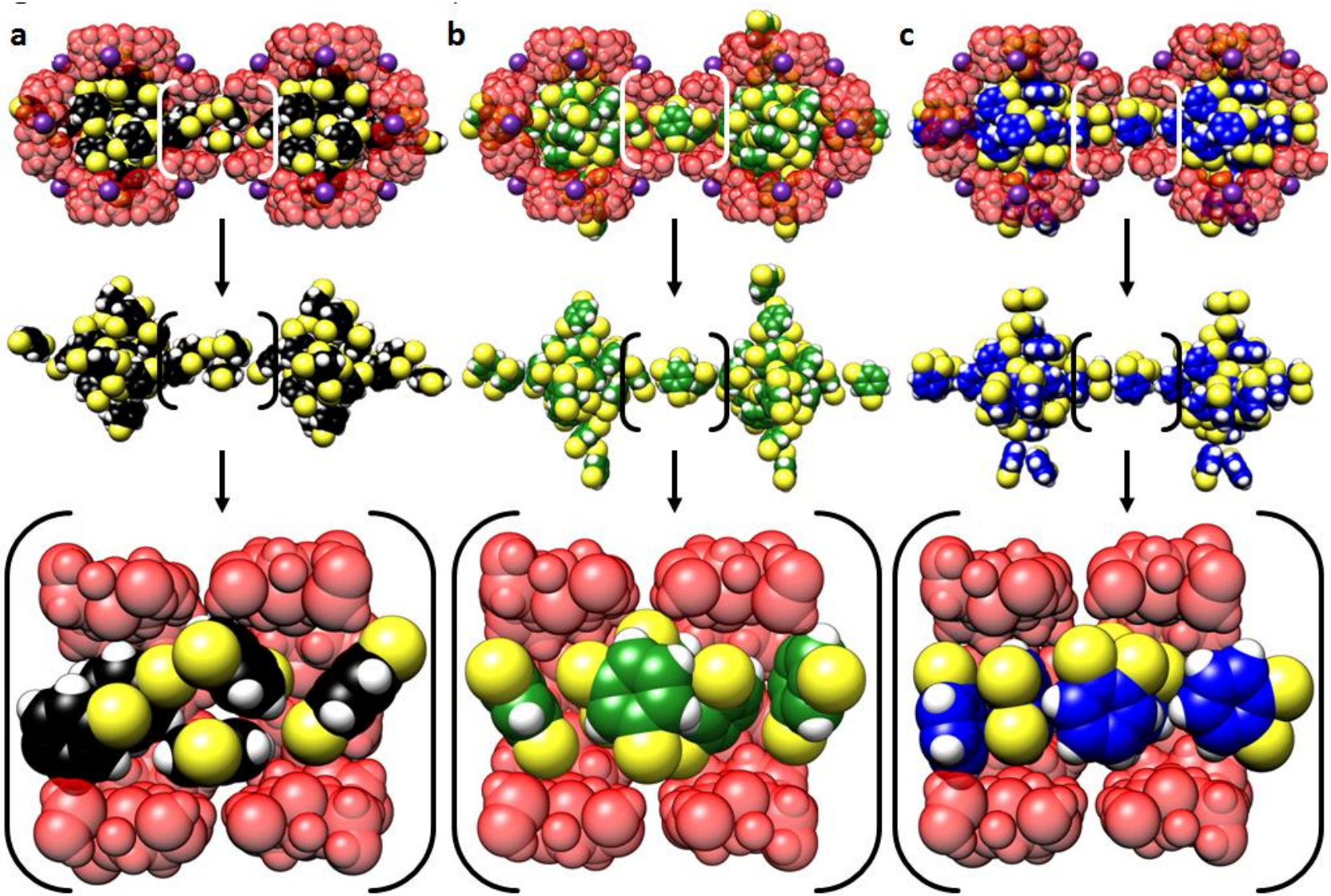

Figure 7

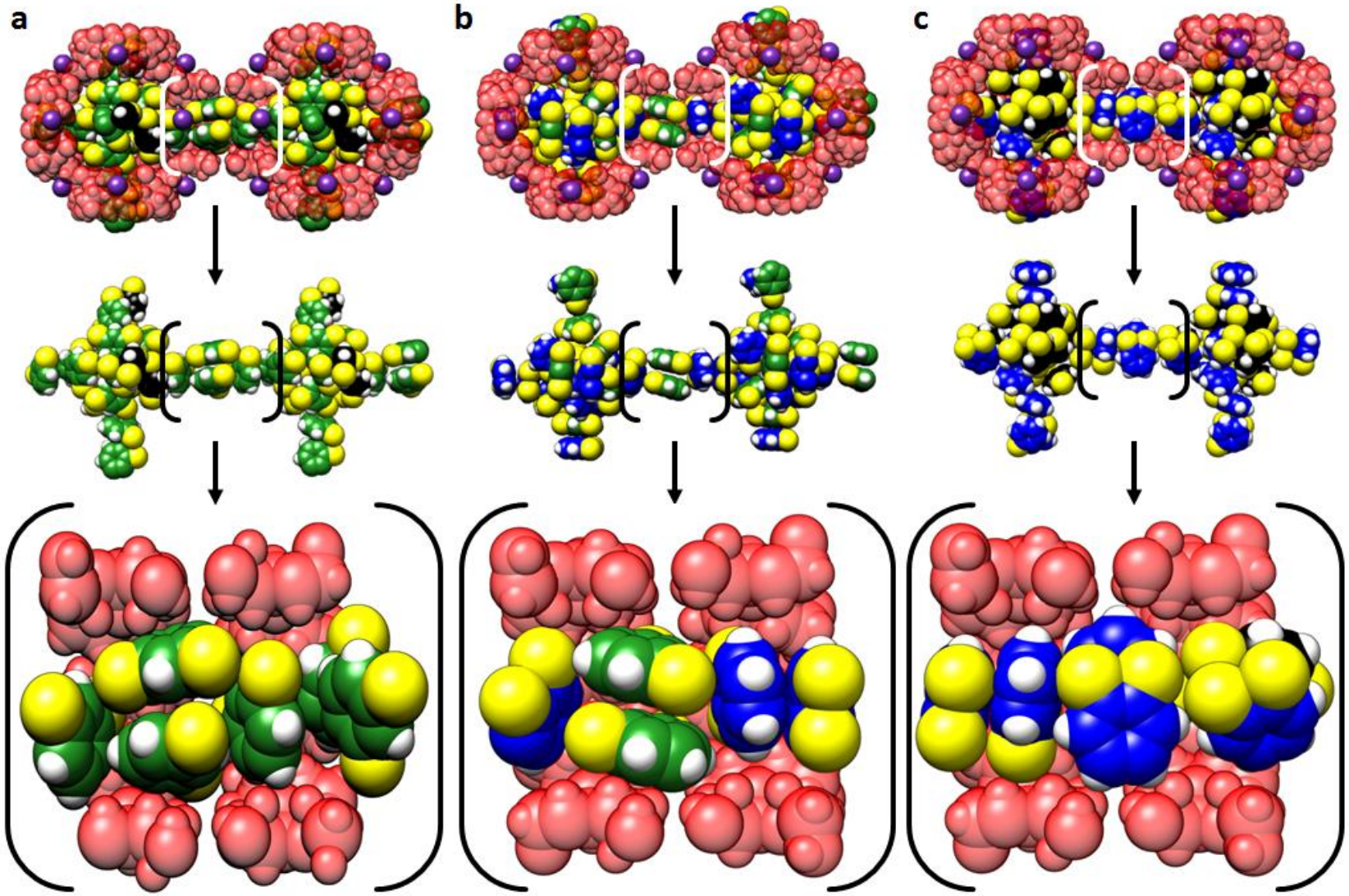

Figure 8

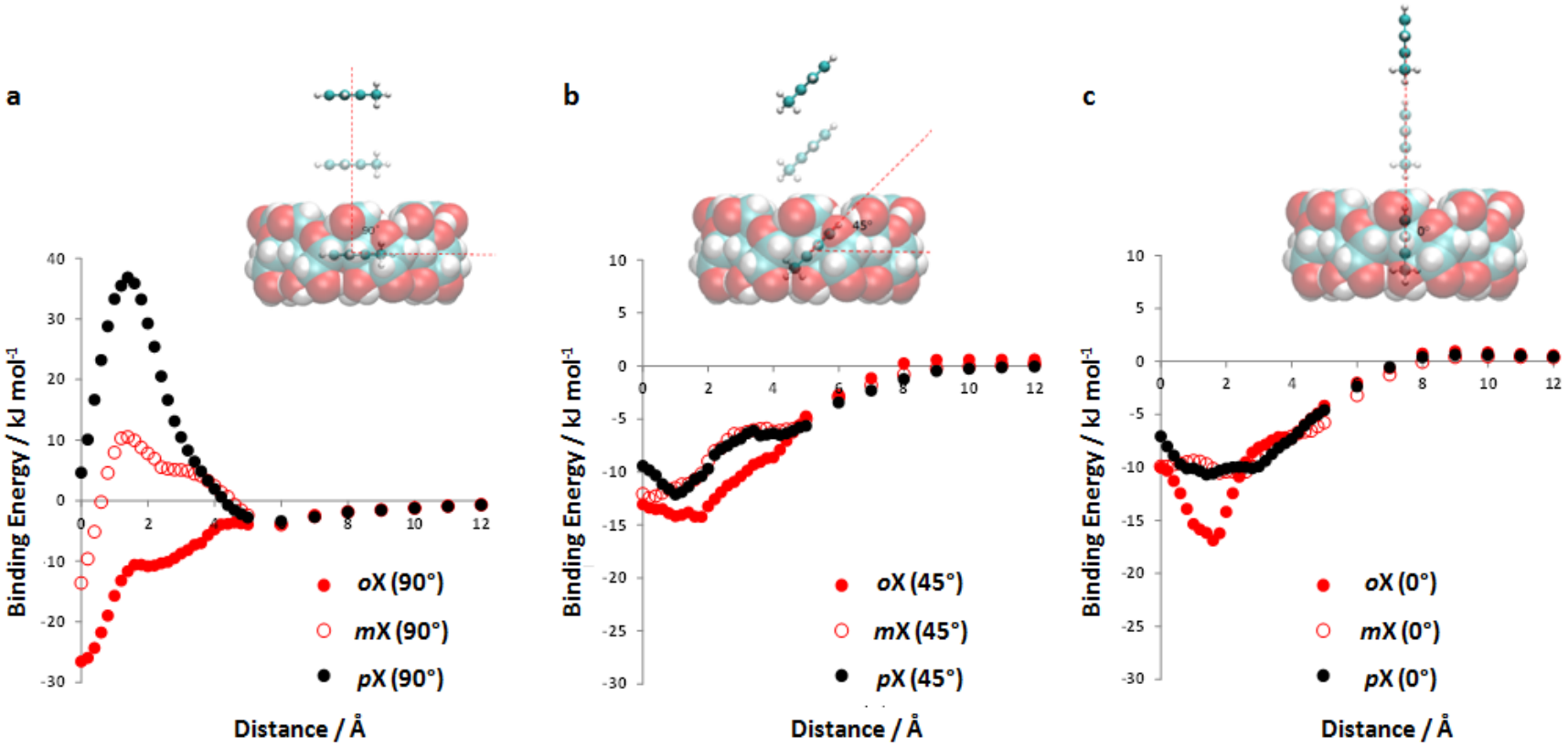
a
b
c
Binding Energy / kJ mol-1
Distance / Å
oX (90°)
mX (90°)
pX (90°)
oX (45°)
mX (45°)
pX (45°)
oX (0°)
mX (0°)
pX (0°)

Figure 9

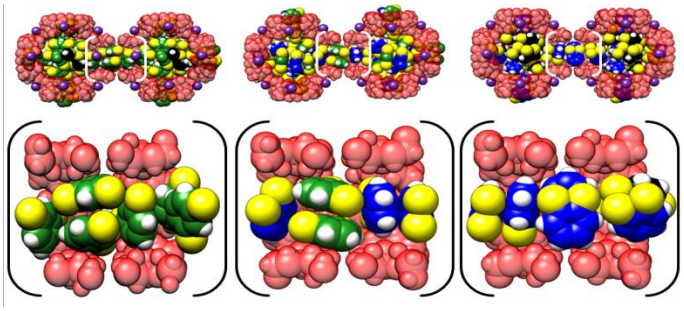

TOC Graphical Abstract

JACS
JOURNAL OF THE AMERICAN CHEMICAL SOCIETY

Carbohydrate-Mediated Purification of Petrochemicals

James M. Holcroft[†‡], Karel J. Hartlieb[†‡], Peyman Z. Moghadam[§], Jon G. Bell[×], Gokhan Barin[ᵚ], Daniel P. Ferris[†], Eric D. Bloch[ᵚ], Mohammed M. Algaradah[¶], Majed S. Nassar[¶], Youssry Y. Botros[¶ǂ], K. Mark Thomas[×], Jeffrey R. Long[ᵚ], Randall Q. Snurr[§], J. Fraser Stoddart[†*]

[†]*Department of Chemistry, Northwestern University, 2145 Sheridan Road, Evanston, IL 60208−3113, USA*

[§]*Department of Chemical & Biological Engineering, Northwestern University, 2145 Sheridan Road, Evanston, IL 60208−3120, USA*

[ᵚ]*Department of Chemistry, University of California, Berkeley, CA 94720−1460, USA*

[×] *Wolfson Northern Carbon Research Laboratories, School of Chemical Engineering and Advanced Materials, Newcastle University, Newcastle upon Tyne NE1 7RU, UK*

[¶] *Joint Center of Excellence in Integrated Nano-Systems (JCIN), King Abdul-Aziz City for Science and Technology (KACST), P. O. Box 6086, Riyadh 11442, KSA*

[ǂ] *University Research Office, Intel Corporation, Building RNB-6-64, 2200 Mission College Boulevard, Santa Clara, CA 95054−1549, USA*

[*]E-mail: stoddart@northwestern.edu

Supporting Information

Table of Contents

Carbohydrate-Mediated Purification of Petrochemicals

James M. Holcroft, Karel J. Hartlieb, Peyman Z. Moghadam, Gokhan Barin, Daniel P. Ferris, Eric D. Bloch, Mohammed M. Algaradah, Majed S. Nassar, Youssry Y. Botros, Jeffrey R. Long, Randall Q. Snurr, J. Fraser Stoddart

ADD Newcastle Authors

But you already have authors on the front page so it could be deleted

1. Materials / General Methods / Instrumentation

Potassium hydroxide, rubidium hydroxide hydrate, cetyltrimethylammonium bromide (CTAB) and MeOH were all purchased from Sigma Aldrich, while γ-cyclodextrin (γ-CD) was obtained from WACKER (CAVAMAX W8 PHARMA). All chemicals were used as received without further purification. CD-MOF-1 and CD-MOF-2 were prepared according to the literature procedures.[S1,S2] Particle size control experiments on CD-MOF-1 were undertaken using a modified protocol from the literature.[S2] Large CD-MOF-2 crystals were harvested and ground using a KRUPS type F203 blender prior to grinding with a pestle and mortar. The ground particles were sieved under an atmosphere of nitrogen through Gilson Company Inc. membrane sieves, #170, #230 and #400, to obtain final particle sizes between 10–37 μm that were unable to pass through a 10 μm sieve. Optical microscope (OM) images for CD-MOF-1 size-controlled particles and CD-MOF-2 particles after grinding were obtained using an Olympus BX53 microscope with an Olympus DP25-mounted camera. Scanning electron microscopy (SEM)

images were collected on a Hitachi S-3400N-II variable pressure SEM, with a tungsten filament and ESED II detector. Samples used for SEM images were suspended in MeOH and diluted to 1 mg mL^{-1} using serial dilutions before deposition onto a carbon tape. The samples were then dried under vacuum for 30 min before imaging them at 30 kV under high vacuum. Powder X-ray diffraction patterns of CD-MOF-1 and CD-MOF-2 were collected on a Bruker AXS APEX2 diffractometer, equipped with a CCD detector and a CuKα IμS microfocus source with MX optics. Data were collected with an area detector as rotation frames over 180° in φ at 2θ values of 12 and 24° and exposed for 10 min for each frame. At a distance of 150 mm, the detector area covers 24° in 2θ. Overlapping sections of data were matched and the resulting pattern integrated using the Bruker APEX2 Phase ID program. Powder pattern data were treated for amorphous background scatter. HPLC was carried out using a Shimadzu analytical normal-phase HPLC, equipped with a Shimadzu SIL-20A HT prominence auto-sampler, SPD-M20A prominence diode array detector, LC-20AB prominence LC and a DGU-20A3 degasser. The normal phase HPLC was fitted with CD-MOF packed columns with dimensions 250 mm length, 4.6 mm internal diameter x 1/4" outer diameter. Unless otherwise stated, chromatography was carried out using HPLC grade hexane as the mobile phase at a flow rate of 1 mL min^{-1}, with 10 μL injection volumes of 50 mg mL^{-1} solutions. Breakthrough experiments were carried out in a 4-mm glass U-tube with CD-MOF-2 crystals. CD-MOF-2 (1.46 g) was used in order to fill the tube at a length of 16 cm. The sample was purged with dry N_2 at 60 ºC overnight to ensure the complete activation of the sample prior to breakthrough measurements. Dry N_2 at a rate of 20 mL/min was bubbled through a mixture of the xylene isomers (15 mL each) at atmospheric pressure. The effluent was passed through a VICI Valco 6-way sampling valve. An aliquot (0.25 mL) of gas was sampled every 5 min and delivered to a Perkin Elmer Clarus 500 Gas Chromatograph fitted with a Supelco SCOT capillary GC column (Sigma-Aldrich 23813-U, 50 ft long, 0.02 in. outside diameter) maintained at 90 ºC. The analyses were performed using an injector and detector (FID) temperature of 220 ºC and N_2 was used as the carrier gas which was maintained at an inlet

pressure of 1.5 psi with a split ratio of 10:1. Baseline separation of the xylene isomers was achieved and all peaks were easily integrated in the resulting GC trace. Single component gas adsorption isotherms were conducted on an IGA gravimetric analyser (Hiden Isochema, IGA-001, Warrington, UK). The analyzer is an ultra-high vacuum (UHV) instrument comprising of a computer controlled microbalance with both pressure and temperature regulation systems. The microbalance had a long-term stability of ± 1 μg with a weighing resolution of 0.2 μg. The CD-MOF-2 sample was outgassed for 12 h until a constant weight was achieved, at < 10^{-6} Pa, at 60°C prior to adsorption measurements. The pressure transducers had ranges of 0 – 2, 2 – 100 and 100 – 1000 mbar. Vapor sorption isotherms were obtained using a circulating water-ethylene glycol bath controlled by a computer using IGA software. The xylene regioisomers used to generate the vapor for the isotherm measurements were degassed fully by repeated evacuation and equilibration cycles of the vapor reservoir. The vapor pressure was gradually increased to the desired value during ~ 30 s in order to prevent disruption of the microbalance. It follows that the period during which the pressure change occurs is small when compared with the adsorption kinetics, allowing isotherm adsorption kinetics to be obtained for each pressure step. The sample temperature was obtained using a thermocouple located 5 mm from the sample. The pressure set point was maintained by computer control throughout the duration of the experiment.

2. Synthetic Protocols

The extended metal-organic frameworks, CD-MOF-1 and CD-MOF-2, were prepared according to literature procedures.[S1,S2]

2.1. *Synthesis of CD-MOF Analogs*

CD-MOF-1: γ-CD (1.30 g, 1 mmol) and KOH (0.45 g, 8 mmol) were dissolved in H_2O (20 mL). The solution was filtered through a 45-µm syringe filter and decanted into separate vials. MeOH was allowed to diffuse slowly into the solution over a period of a week.

CD-MOF-2: γ-CD (1.30 g, 1 mmol) and RbOH (0.82 g, 8 mmol) were dissolved in H_2O (20 mL). The solution was filtered through a 45-µm syringe filter and decanted into separate vials. MeOH was allowed to diffuse slowly into the solution over a period of a week.

2.2. *Particle Preparation and Activation*

The crystals were harvested and crushed to sizes of approximately 100–500 µm. The crystals were filtered and washed with MeOH (4 x 50 mL) under vacuum. Additional washing with CH_2Cl_2 (3 x 50 mL) was carried out to remove the excess of MeOH. The crystals were then left to vacuum dry for 12 h. The crystals were transferred to a N_2 glove box where they were finely ground using a KRUPS type F203 blender, prior to being ground further using a pestle and mortar. The resulting particles were sieved through Gilson Company Inc. membrane sieves, #170, #230 and #400 with repeated grinding between sieving through each membrane to ensure particles smaller than 37 µm were attained. The milled CD-MOF-2 particles were checked for crystallinity and structural integrity using powder X-ray crystallography before being dry loaded or slurry loaded using any non-aqueous solvent into the column (SI B4).

2.3. *Particle Size Control Synthesis of CD-MOF-1*

CD-MOF-1 was synthesized using a modified literature proceedure.[S2]

CD-MOF-1-Micro: γ-CD (8.15 g, 6.2 mmol) and KOH (2.8 g, 49.7 mmol) were dissolved in H_2O (250 mL). The solution was filtered through a 45-µm syringe filter and decanted into separate vials (5 mL in each vial). MeOH was allowed to diffuse slowly into the solutions for 24 h. Each solution was decanted into a fresh vial before cetyltrimethylammonium bromide (CTAB) was added, and after the complete dissolution of CTAB, MeOH was diffused into the solution for an additional 24 h. The solutions were combined together, and centrifuged at 5000 rpm for 10

min before the supernatant was removed and replaced with MeOH. This process was repeated five times in order to ensure CTAB was completely removed from the sample.

Varying the amount of CTAB during the synthesis of CD-MOF-1 can be used to control the size of the CD-MOF-1 particles as confirmed (**Table S1**) by optical microscopy and SEM. The size of the CD-MOF-1 particles is utilized in this system to control the elution times of the aliphatic and aromatic compounds by optimizing packing conditions to prevent the bypassing of the solid phase.

Table S1. CD-MOF-1 Particle Size Ranges with Varying CTAB Concentrations

Material	CTAB / mg	Particle Size / µm	Image
CD-MOF-1-Micro1	20	25	S2a / S3a
CD-MOF-1-Micro2	40	10–15	S2b / S3b
CD-MOF-1-Micro3	60	5–15	S2c / S3c
CD-MOF-1-Micro4	80	1–10	S2d / S3d

The particle size modified column was prepared using CD-MOF-1-Micro-2 , where CTAB (40 mg) was added to the reaction mixture after the first incubation period. This protocol facilitated the formation of CD-MOF-1 crystallites of 10–15 µm.

2.4. *HPLC Column Loading*

HPLC was carried out using a Shimadzu analytical normal-phase HPLC, fitted with a CD-MOF packed column with dimensions 250 mm in length and 4.6 mm internal diameter and 1/4" outer diameter. Chromatography was carried out using HPLC-grade hexane as the mobile phase at a flow rate of 1 mL min^{-1}, with 10 µL injection volumes of 50 mg mL^{-1} solutions, unless otherwise stated. The CD-MOF particles were checked for their crystallinity and structural integrity using powder X-ray crystallography before being packed into the column. The blended CD-MOF-2 particles can be dry loaded or slurry loaded — using any non-aqueous solvent — into the column, whilst the 10–15 µm particles of CD-MOF-1 were slurry loaded using a non-aqueous solvent.

3. Spectroscopic Characterization of CD-MOF Samples

3.1. *Optical Microscopy (OM)*

Optical Microscope (OM) images were obtained using an Olympus BX53 microscope with an Olympus DP25-mounted camera.

3.1.1. *CD-MOF-2 Particles*

Particle images were analyzed using optical microscopy in order to determine particle size and shape distributions. In an effort to prevent degradation of the particles by solvent loss, they were mounted onto glass slides using paratone oil. The images of CD-MOF-2 particles employed in the top-down column investigations are illustrated under an optical microscope in **Figure S1**. We believe the variation in particle shape and size arising from the grinding phases is the primary reason for inefficient particle packing, resulting in poor separations.

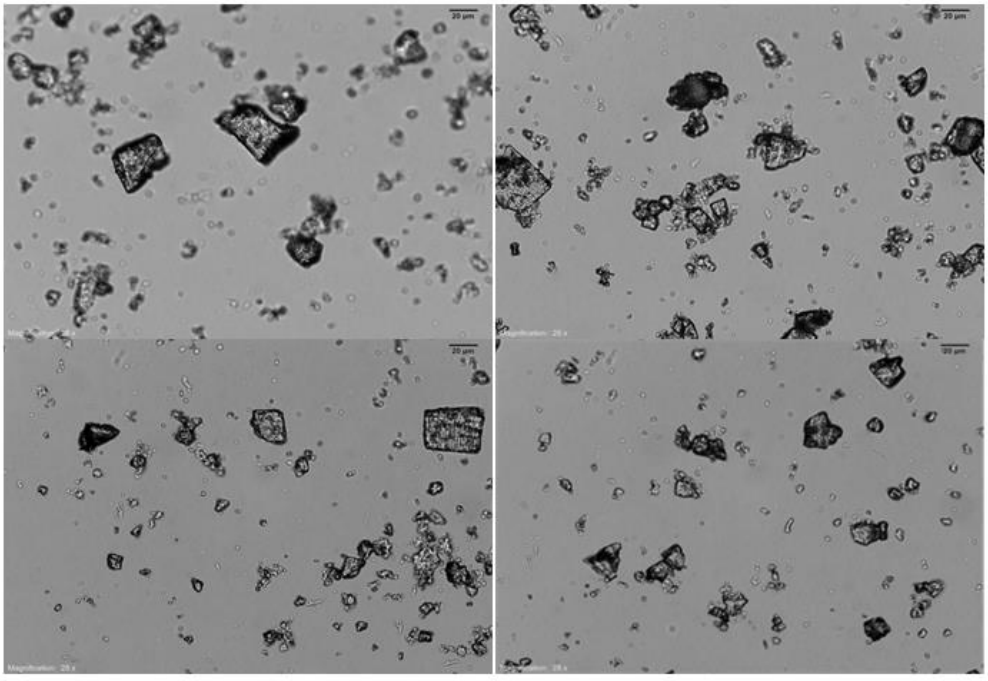

Figure S1. CD-MOF-2 Particles viewed under an optical microscope at x25 magnification after fine grinding, prior to packing the top-down HPLC column.

The particles of CD-MOF-2 observed under an optical microscope have irregular shapes and sizes, ranging from 0.5 – 37 µm in cross section. Although the observed CD-MOF-2 particles were fragmented, they remained crystalline as confirmed visually using plane polarized light under an optical microscope while their bulk crystallinity was established using powder X-ray diffraction techniques.

3.1.2. *CD-MOF-1 Particles*

Size distributions of CD-MOF-1 crystallizations with CTAB were monitored by both optical microscopy (**Figure S2**) and SEM (**Figure S3**).

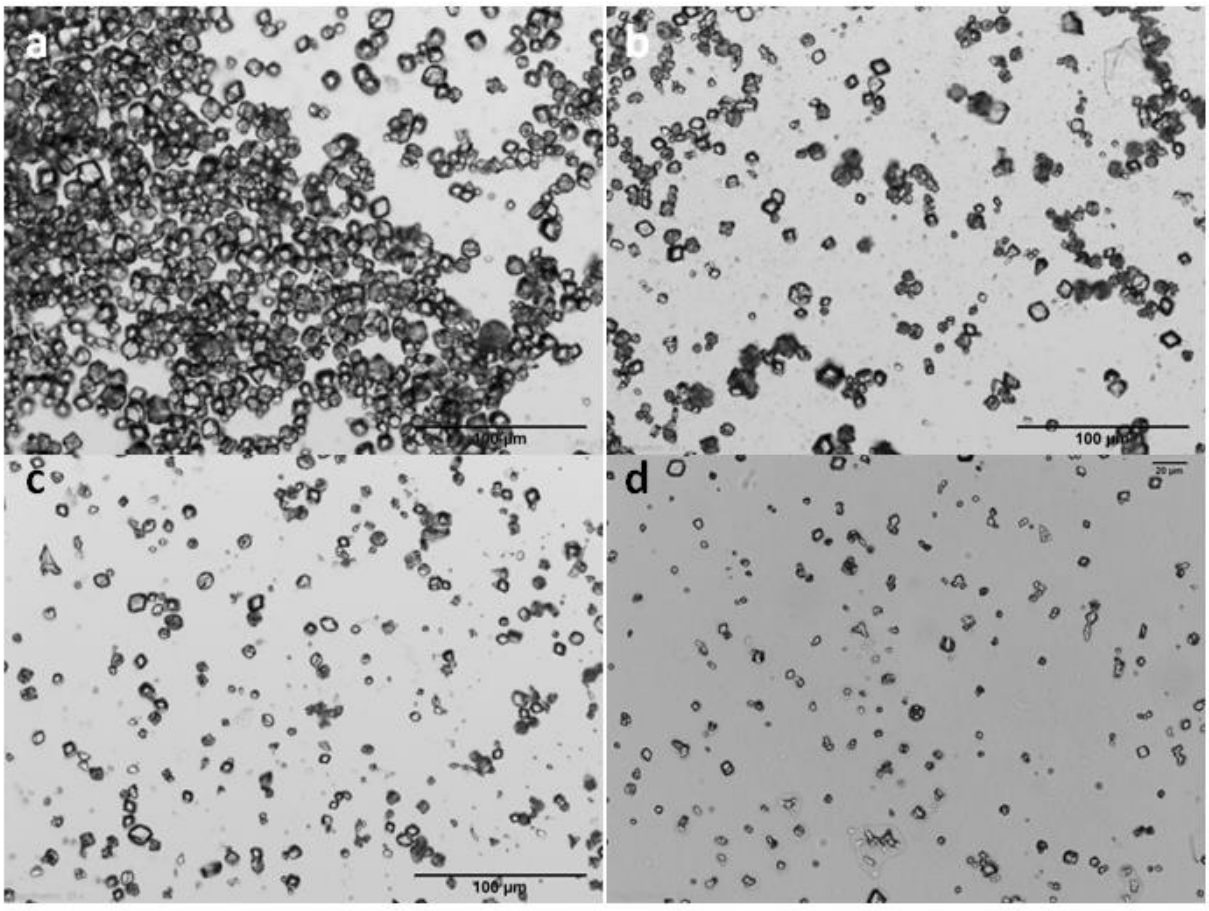

Figure S2. Optical micrographs of CD-MOF-1 particles crystallized in the presence of **(a)** 20 mg, **(b)** 40 mg, **(c)** 60 mg, **(d)** 80 mg of CTAB.

CD-MOF-1 Crystallizations with CTAB, monitored by optical microscopy, highlight the consistent formation of regular cubic-shaped CD-MOF-1 particles with size distributions at varying concentrations of CTAB recorded in **Table S1**. Confirmation of the size variation ranges was gained using SEM imaging techniques to measure the cross sections of the CD-MOF-1 particles.

3.2. *Scanning Electron Microscopy (SEM)*

SEM Images were collected on a Hitachi S-3400N-II variable pressure SEM, with a tungsten filament and ESED II detector. The SEM images portrayed in **Figure S3** confirm the size variation associated with CD-MOF-1 growth in the presence of CTAB.

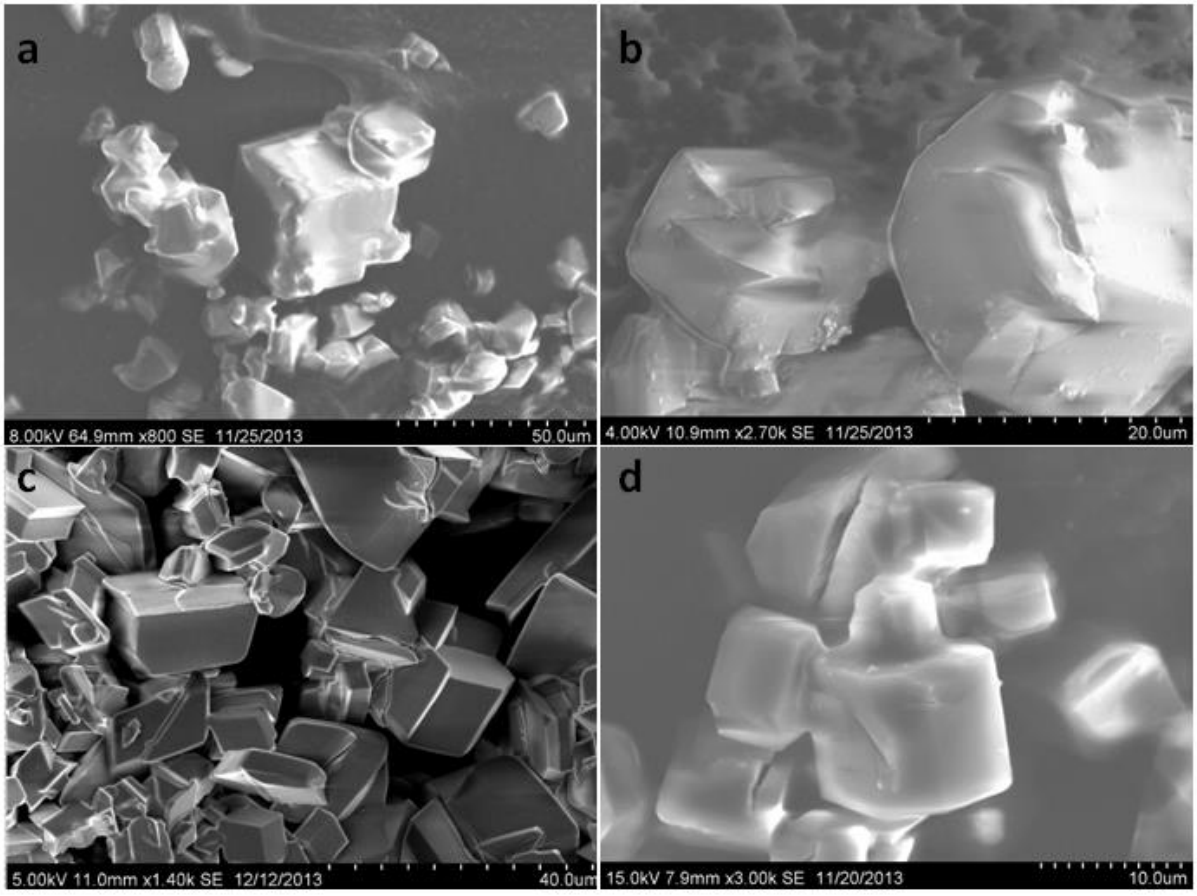

Figure S3. SEM images of CD-MOF-1 particles crystallized in the presence of **(a)** 20 mg, **(b)** 40 mg, **(c)** 60 mg, **(d)** 80 mg of CTAB.

CD-MOF-1 Crystallizations with CTAB monitored by SEM show the subtle differences in the size and shape of the CD-MOF-1 particles. The particles exhibit cubic morphology consistently with small defects at the crystal surfaces. The non-conductive nature of CD-MOF-1 crystals results in the presence of surface charging, giving rise to the 'white glowing' of particles. Surface charging is reduced partially **(Figure S3 c)** using sputtering techniques.

3.3. *Powder X-Ray Diffraction*

Powder patterns for CD-MOF-1 and CD-MOF-2 (**Figure S4**) were collected on a Bruker AXS APEX2 diffractometer equipped with a CCD detector and a CuKα IμS microfocus source with MX optics. Overlapping sections of data were matched and the resulting pattern integrated using the Bruker APEX2 Phase ID program, before the powder pattern data was treated for amorphous background scattering.

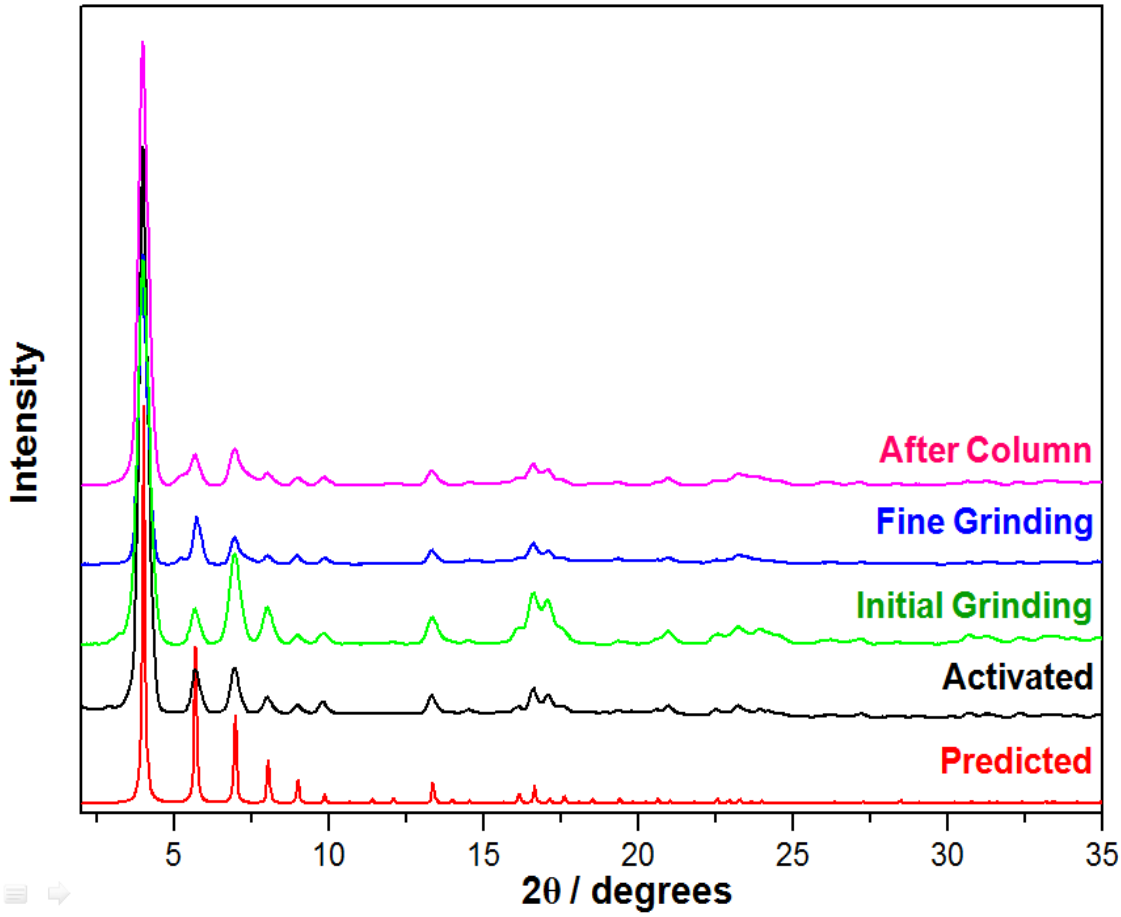

Figure S4. Powder X-ray diffraction patterns of CD-MOF-2 at different intervals of processing when preparing to pack the CD-MOF-2 column, Red — calculated powder diffraction pattern from single crystal X-ray diffraction, Black — after harvesting and activation under vacuum, Green — CD-MOF-2 after initial grinding using automated grinder, Blue — CD-MOF-2 after intensive fine grinding under a nitrogen atmosphere, Pink — CD-MOF-2 after usage in the HPLC column for 72 h.

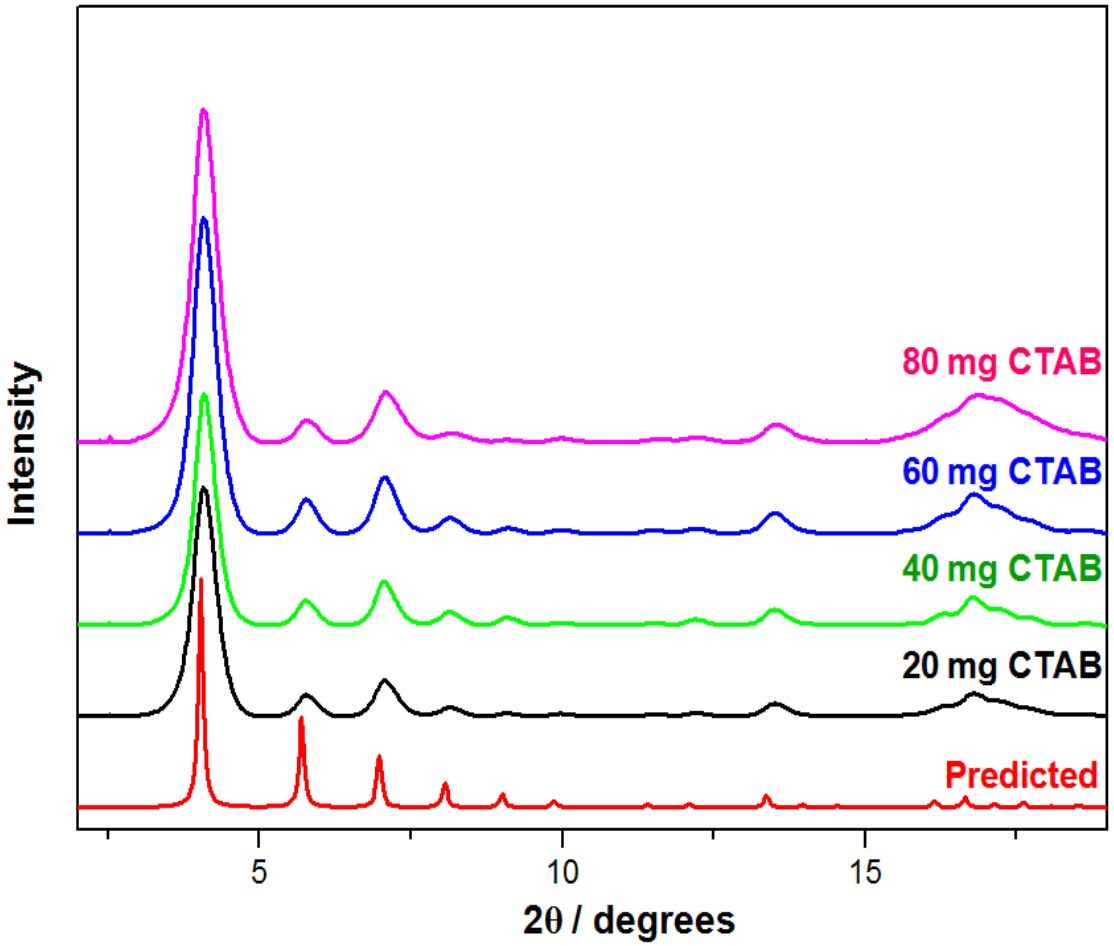

Figure S5. Powder X-ray diffraction patterns of CD-MOF-1 employed in the packing of the CD-MOF-1 Bottom-up column. The different samples were crystallized in the presence of varying amounts of CTAB, Red — calculated powder diffraction pattern from the single crystal X-ray diffraction pattern, Black — CD-MOF-1 crystallized with 20 mg CTAB, Green — CD-MOF-1 crystallized with 40 mg CTAB, Blue — CD-MOF-1 crystallized with 60 mg CTAB, Pink — CD-MOF-1 crystallized with 80 mg CTAB.

Although the powder X-ray diffraction patterns (**Figure S5**) for CD-MOF-1 exhibit line broadening as the particle sizes decrease, crystallinity remains consistent with that observed for the predicted powder diffraction pattern calculated from the CD-MOF-1 single crystal diffraction data. This observation confirms the formation of CD-MOF-1 regardless of the CTAB concentration.

4. HPLC Analysis using CD-MOF-1 and CD-MOF-2 Columns

4.1. *Xylene Separations*

4.1.1. *Xylene Isomers*

The similar physical properties (**Table S2**) of the BTEX molecules (Benzene, Toluene, Ethylbenzene and the Xylene isomers) gives rise to considerable challenges when conducting separations using conventional techniques such as distillation,[S3] crystallisation[S4,S5] and simulated moving bed technologies.[S6]

Table S2. Physical Properties of BTEX (Benzene, Toluene, Ethylbenzene and the Xylene isomers) Components

Adsorbant	Boiling Point / °C	Melting Point / °C	Kinetic Diameter / nm
Benzene	80.1	5.5	0.58
Toluene	110.6	– 95	0.61
Ethylbenzene	136.2	– 95	0.62
ortho-Xylene	144.4	– 27.2	0.68
meta-Xylene	139.1	– 47.9	0.68
para-Xylene	138.3	13.4	0.58

Separations (**Figure S6**) of the three xylene isomers using both a top-down HPLC column and a bottom-up HPLC column revealed (**Table S3**) significant differences in their corresponding resolutions and separation factors (defined in section E). The improved resolution and separation factors between the top-down and bottom-up columns coincide with the control over small regular particle formation, resulting in more efficient packing inside the column. Liquid-phase separations in hexane of 10 µL injections of 50 mg mL^{-1} xylene mixtures exhibited base-line separation with the retention order *ortho* > *meta* > *para*. Separation of the xylene isomers is maintained upon injection of 10 µL of a neat solution of xylenes **Figure S7** . The separation of the xylene isomers is accompanied by the separation of BTEX with the elution order, *para* > *meta* > ethylbenzene > toluene > *ortho* > benzene.

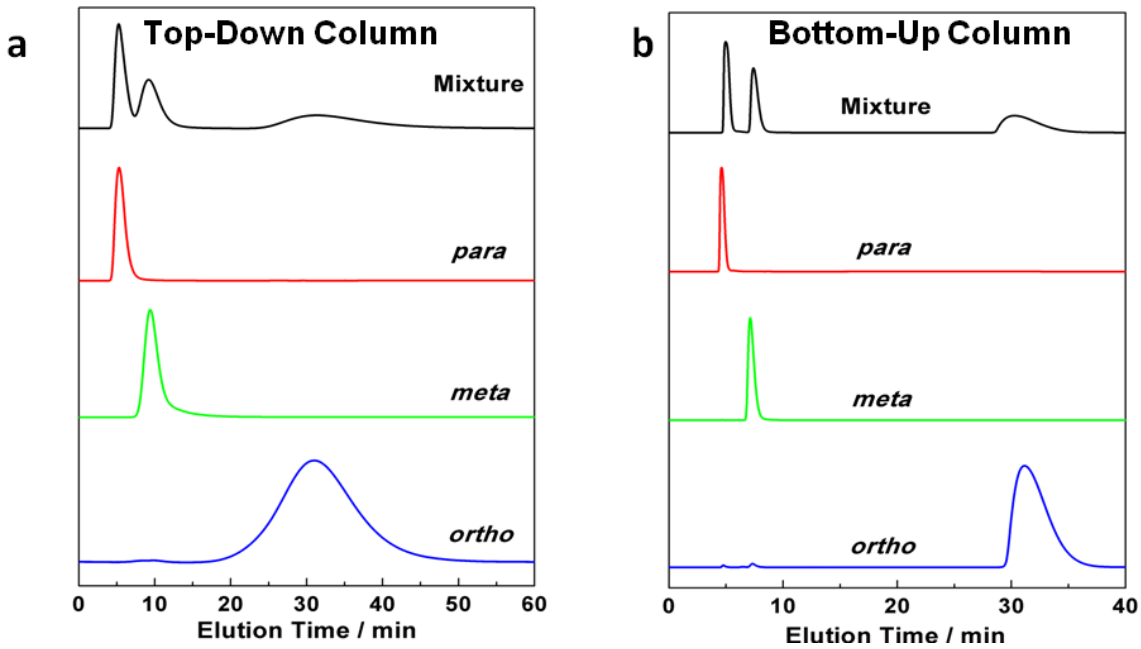

Figure S6. CD-MOF Column separations of 50 mg mL^{-1} xylene mixtures in HPLC-grade hexane at a flow rate of 1 mL min^{-1} **(a)** Top-down CD-MOF-2 column — particle sizes 10–37 μm — and **(b)** Bottom-up CD-MOF-1 column — particle sizes 10–15 μm. The stacking of separation profiles shows the assignment of the elution order from the mixture of xylene isomers (**black**) as *para*-xylene (**red**), *meta*-xylene (**green**) and *ortho*-xylene (**blue**) at 255 nm

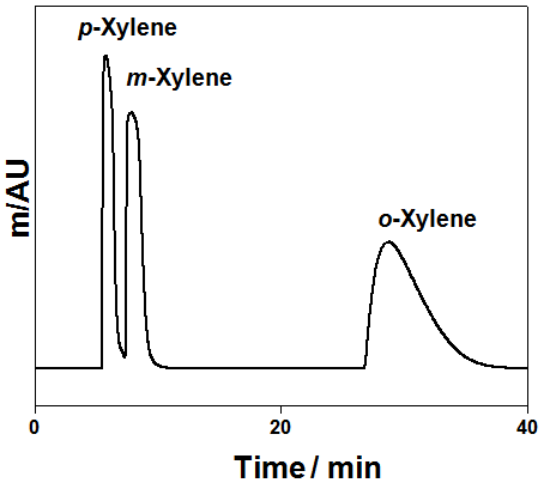

Figure S7. Bottom-up CD-MOF-1 column — particle sizes 10–15 μm — separation of 10 μL of neat xylene mixture at a flow rate of 1 mL min^{-1}, shows the elution order of *para*-xylene, *meta*-xylene and *ortho*-xylene.

4.1.2. *BTX Mixture*

Separation (**Figure S8**) of BTX (Benzene, toluene, and the three xylene isomers) was achieved after 6 h. Separation (**Figure S9**) of BTEX was achieved after removing MeOH from the framework using ^{i}PrOH, the bottom-up CD-MOF-1 column is then reactivated by removing the ^{i}PrOH using CH_2Cl_2 before running the BTEX mixtures in HPLC-grade hexane.

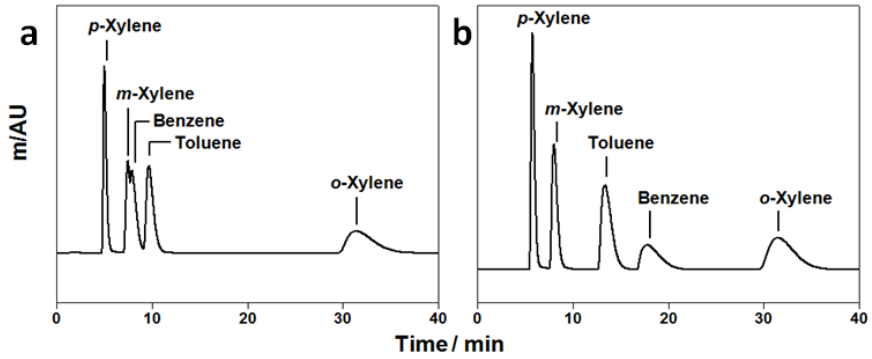

Figure S8. Bottom-up CD-MOF-1 column — particle sizes 10–15 µm — separations of 50 mg mL^{-1} BTX mixtures in HPLC-grade hexane at a flow rate of 1 mL min^{-1} **(a)** BTX separation after running the column for 4 h and **(b)** BTX separation after running the column for 30 h

4.1.3. *BTEX Mixture*

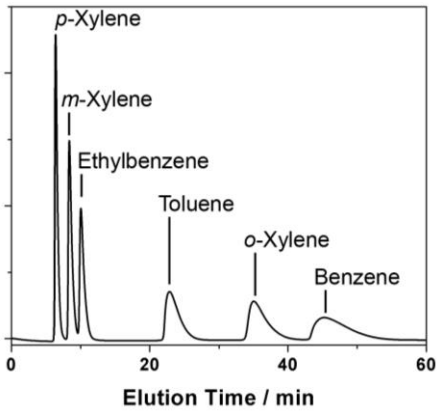

Figure S9. Bottom-up CD-MOF-1 column — particle sizes 10–15 µm — separations of 50 mg mL^{-1} BTEX mixtures using HPLC-grade hexane as the mobile phase at a flow rate of 1 mL min^{-1} after activation of the column by a CH_2Cl_2, detected at 255 nm

4.2. *Ethyltoluene Separations*

Separation (**Figure S10**) of the regioisomers of ethyltoluene highlight the columns selectivity of *ortho>meta>para*, with isomers eluting at similar times to those observed for their respective xylene isomers. This separation is indicative of the guests ability to pack within the transverse pores of the γ-CD rings, revealing CD-MOFs ability to shape-select the regioisomers of extended substituted aromatic hydrocarbons.

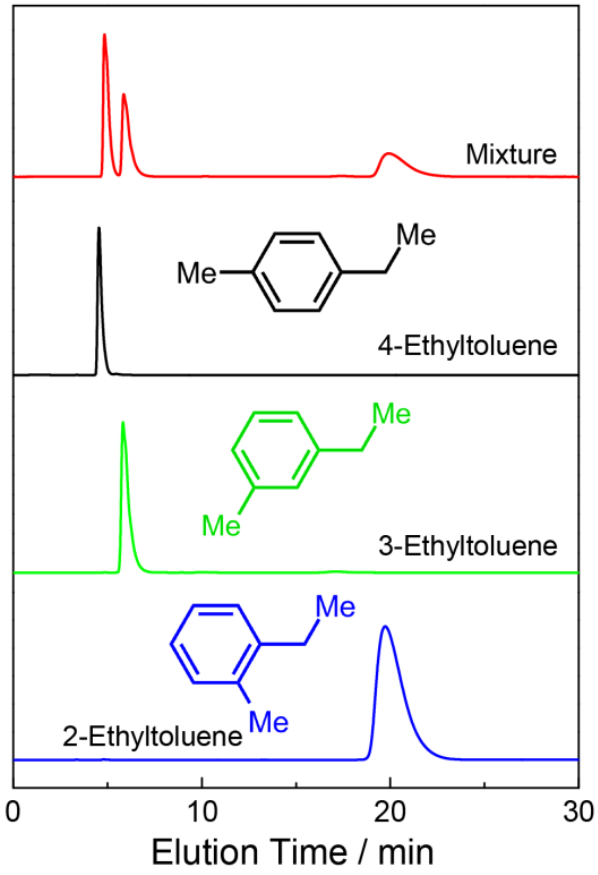

Figure S10. Bottom-up CD-MOF-1 column separation of 50 mg mL^{-1} 4-ethyltoluene, 3-ethyltoluene and 2-ethyltoluene in HPLC-grade hexane at a flow rate of 1 mL min^{-1} using — particle sizes 10–15 µm — detected at 266 nm.

4.3. *Cymene Separations*

Separation (**Figure S11**) of the regioisomers of cymene were used to investigate the extent of the *ortho>meta>para* selectivity within CD-MOF. Although the selectivity order is consistent with that observed for the other regioisomers of compounds separated using CD-MOF, the ability to separate the regioisomers is reduced, with baseline merging for the *para*- and *meta*-cymene signals. This suggests the limit of CD-MOFs shape recognition has been reached, with the additional branching preventing efficient packing of both the *para*- and *meta*-cymene isomers.

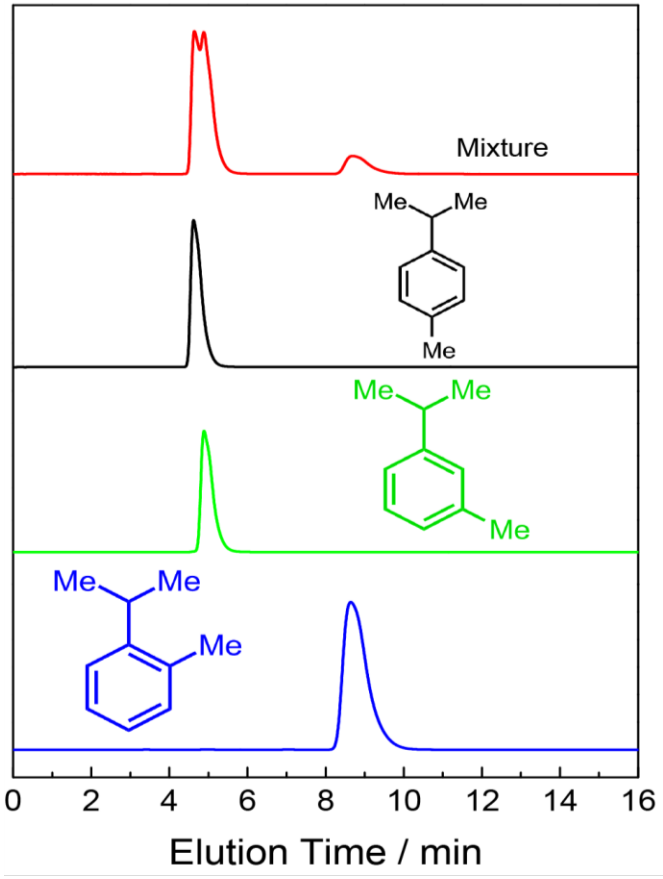

Figure S11. Bottom-up CD-MOF-1 column separation of 50 mg mL^{-11} 4-cymene, 3-cymene and 2-cymene in HPLC-grade hexane at a flow rate of 1 mL min^{-1} using — particle sizes 10–15 µm — detected at 266 nm.

4.4. *Cumene Separations*

Separation (**Figure S12**) of the valuable petrochemical feedstock cumene from impurities *n*-propylbenzene and 1,4-diisopropylbenzene was achieved using an activated bottom-up CD-MOF-1 column.

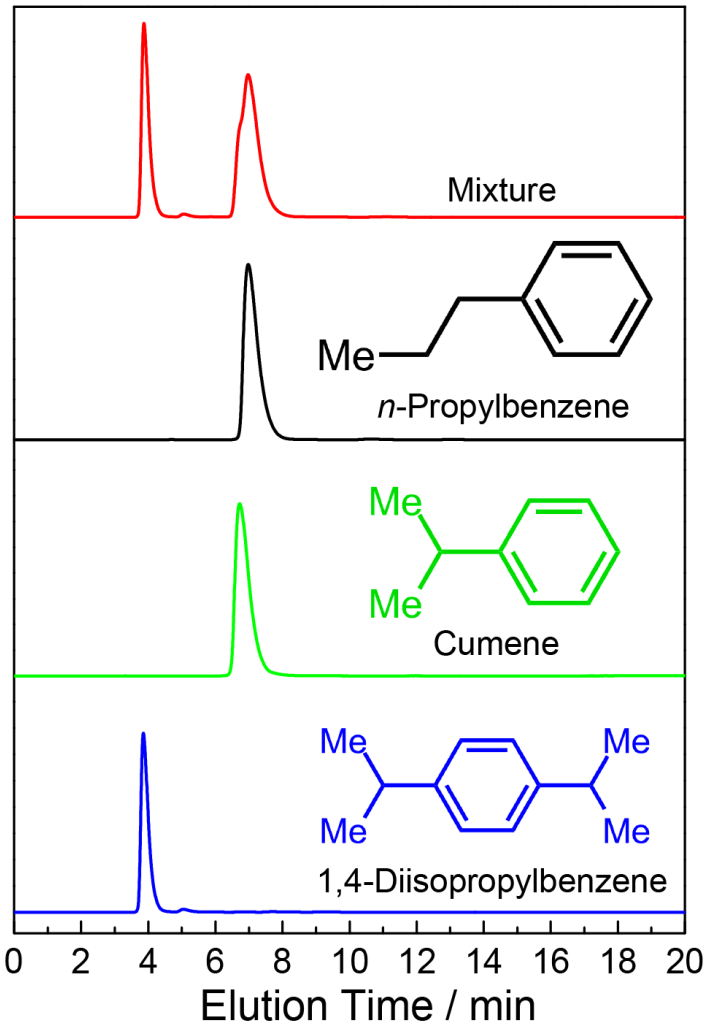

Figure S12. Bottom-up CD-MOF-1 column separation of 50 mg mL^{-1} cumene, n-propylbenzene and 1,4-disopropylbenzene mixture in HPLC-grade hexane at a flow rate of 1 mL min^{-1} using — particle sizes 10–15 µm— detected at 255 nm.

5. Selectivity Calculations and Separation Factors

5.1. *Calculations for Capacity and Separation Factors*

Capacity factors (*k*) for liquid phase analytical chromatographic data recorded for the separations of compounds in **Section D** were calculated[S9,S11] using **Equation 1**. The capacity factor (*k*) defines the amount of time a compound spends in the stationary phase versus the mobile phase.

$$k_i = \frac{tr_i - t_{res}}{t_{res}} \quad \textbf{(1)}$$

k_i Capacity factor tr_i Retention time t_{res} Bed void time

The separation ability of a material is determined by the separation factor[9] (α_{ij}) which measures the difference in interactions between the two compounds in question and the stationary phase. The separation factor (α_{ij}) is calculated[9] as a ratio between capacity factors of the two compounds using **Equation 2**.

$$\alpha_{ij} = \frac{k_i}{k_j} \quad \textbf{(2)}$$

α_{ij} Separation factor k_i Capacity factor *i* k_j Capacity factor *j*

The resolution factor (*R*) of the peaks is calculated using **Equation 3**. It determines[11] the difference in retention times, whilst taking account of the peak width.

$$R = \frac{2[tr_i - tr_j]}{W_i + Wj} \quad \textbf{(3)}$$

R Resolution factor tr_i Retention time *i* W_i Peak width *i*

5.2. *Separation Factor Tables*

The separation factors for xylene isomers for both the CD-MOF-2 top-down column and CD-MOF-1 bottom-up column are recorded in **Table S3**. BTX separation factors are recorded in **Table S4**. The full activation of the bottom-up CD-MOF-1 column resulted in the separation of BTEX mixtures with separation factors recorded in **Table S5**, these can be compared to the separation factors of currently available MOFs, some of which are recorded in **Table S6**.

Table S3. CD-MOF Column Separation Factors of 50 mg mL^{-1} Xylene Mixtures in HPLC-grade Hexane at a Flow Rate of 1 mL min^{-1}

Adsorbent	Solvent		*j*		
		i	*ortho*-Xylene	*meta*-Xylene	*para*-Xylene
CD-MOF-2	Hexane	*ortho*-Xylene	–	4.76	16.37
Top-down		*meta*-Xylene	0.21	–	3.44
Column		*para*-Xylene	0.06	0.29	–
CD-MOF-1	Hexane	*ortho*-Xylene	–	6.73	17.93
Bottom-up		*meta*-Xylene	0.15	–	2.67
Column		*para*-Xylene	0.06	0.38	–
CD-MOF-1	Pure	*ortho*-Xylene	–	5.72	10.76
Bottom-up	Xylene	*meta*-Xylene	0.17	–	1.88
Column	Mixture	*para*-Xylene	0.09	0.53	–

Table S4. CD-MOF Column Separation Factors of 50 mg mL^{-1} BTX Mixtures in HPLC-grade Hexane at a Flow Rate of 1 mL min^{-1}

Adsorbent		***J***				
	i	*ortho*-Xylene	*meta*-Xylene	*para*-Xylene	Benzene	Toluene
CD-MOF-1	*ortho*-Xylene	–	7.08	17.89	6.29	4.49
Bottom-up	*meta*-Xylene	0.14	–	2.53	0.89	0.63
Column	*para*-Xylene	0.06	0.39	–	0.35	0.25
4 Hours	Benzene	0.16	1.12	2.85	–	0.71
	Toluene	0.22	1.58	3.99	1.40	–
CD-MOF-1	*ortho*-Xylene	–	6.11	12.19	1.96	2.82
Bottom-up	*meta*-Xylene	0.16	–	1.99	0.32	0.46
Column	*para*-Xylene	0.08	0.50	–	0.16	0.23
30 Hours	Benzene	0.50	3.10	6.19	–	1.43
	Toluene	0.35	2.17	4.33	0.69	–

Table S5. Activated Bottom-up CD-MOF Column Separation Factors of 50 mg mL^{-1} BTEX mixtures in HPLC-grade Hexane at a Flow Rate of 1 mL min^{-1}

Adsorbent							
	i			***j***			
		ortho-Xylene	*meta*-Xylene	*para*-Xylene	Benzene	Toluene	Ethylbenzene
CD-MOF-1	*ortho*-Xylene	–	6.68	11.26	0.76	1.61	4.75
Bottom-up	*meta*-Xylene	0.15	–	1.69	0.11	0.24	0.71
Column	*para*-Xylene	0.09	0.59	–	0.07	0.14	0.42
	Benzene	1.32	8.82	14.88	–	2.13	6.27
	Toluene	0.62	4.14	6.98	0.47	–	2.94
	Ethylbenzene	0.21	1.41	2.37	0.21	0.34	–

Table S6. Separation Factors of Known Frameworks Taken from the Literature for the Three Xylene Isomers and Ethylbenzene

Adsorbent	Solvent						
		i	***j***				
			ortho-Xylene	*meta*-Xylene	*para*-Xylene	Ethyl-benzene	Ref.
HKUST-1	Hexane	*ortho*-Xylene	–	0.4	0.7	0.7	S7
[$Cu_3(BTC)_2$]		*meta*-Xylene	2.4	–	1.1	1.4	
		para-Xylene	1.4	0.9	–	1.2	
		Ethyl-benzene	1.4	0.7	0.8	–	
MIL-47	Hexane	*ortho*-Xylene	–	2.0	1.4	10.9	S8
		meta-Xylene	0.5	–	0.4	4.2	
		para-Xylene	0.7	2.9	–	9.7	
		Ethyl-benzene	0.1	0.2	0.1	–	
MIL-53(Al)	Hexane	*ortho*-Xylene	–	2.7	3.5	10.9	S7,S8
		meta-Xylene	0.4	–	1.2	3.8	
		para-Xylene	0.3	0.8	–	3.1	
		Ethyl-benzene	0.1	0.3	0.3	–	
MIL-53(Fe)	Heptane	*ortho*-Xylene	–	1.3	3.5	12.3	S9
		meta-Xylene	0.7	–	2.5	9.2	
		para-Xylene	0.3	0.4	–	3.5	
		Ethyl-benzene	0.1	0.1	0.3	–	
UiO-66	Heptane	*ortho*-Xylene	–	1.8	2.4	–	S10
		meta-Xylene	0.6	–	–	–	
		para-Xylene	0.4	–	–	–	
		Ethyl-benzene	–	–	–	–	

The separation factors for the bottom-up CD-MOF-1 column of cumene from impurity mixtures are recorded in **Table S7**. Separation factors are recorded for the regioisomers of ethyltoluene (**Table S8**) for comparison to those recorded for the regioisomers of xylene.

Table S7. Bottom-up CD-MOF-1 Column Separation Factors of 50 mg mL^{-1} Cumene from Impurity Mixtures of *n*-Propylbenzene and 1,4-Diisopropylbenzene in HPLC-grade Hexane at a Flow Rate of 1 mL min^{-1}

Adsorbent	Solvent			*j*	
		i	Diisopropylbenzene	Cumene	propylbenzene
CD-MOF-1	Hexane	Diisopropylbenzene	–	0.14	0.12
Bottom-up		Cumene	7.12	–	0.88
Column		*n*-propylbenzene	8.09	1.13	–

Table S8. Bottom-up CD-MOF-1 Column Separation Factors of 50 mg mL^{-1} Mixtures of 4-, 3- and 2-Ethyltoluene in HPLC-grade Hexane at 1 mL min^{-1}

Adsorbent	Solvent			*j*	
		i	4-Ethyltoluene	3-Ethyltoluene	2-Ethyltoluene
CD-MOF-1	Hexane	4-Ethyltoluene	–	0.47	0.07
Bottom-up		3-Ethyltoluene	2.10	–	0.15
Column		2-Ethyltoluene	13.77	6.56	–

6. Computational Modeling and Analysis

Vapor phase pure component and mixture adsorption isotherms in CDMOF-2 were calculated from grand canonical Monte Carlo (GCMC) simulations using the Multipurpose Simulation Code,[S12] MuSiC. GCMC moves used were insertion, deletion, translation and rotation and, in the case of binary mixtures, we also employed identity swap moves. For each pressure point we used 150 $\times 10^6$ GCMC steps for equilibration, after which another 150 $\times$ 10^6 steps were employed to calculate the average properties. We used one unit cell of CDMOF-2 with dimensions of 31.07 x 31.07 x 31.07 Å. Framework atoms were kept fixed at their crystallographic coordinates during the simulations. The Universal Force Field[S13] (UFF) was employed for the Lennard-Jones parameters of the framework atoms. The OPLS[S14] force field was used to model xylene isomers.

Cross Lennard-Jones parameters (**Table S9,10**) were calculated using Lorentz-Berthelot mixing rules, and a cut-off distance of 12.8 Å was used for all Lennard-Jones interactions. The partial atomic charges for the framework were obtained from the EQeq[S15] charge equilibrium method. Long range electrostatic interactions (**Table S11**) for adsorbate-adsorbate and adsorbent-adsorbate were calculated using the Ewald technique[S16].

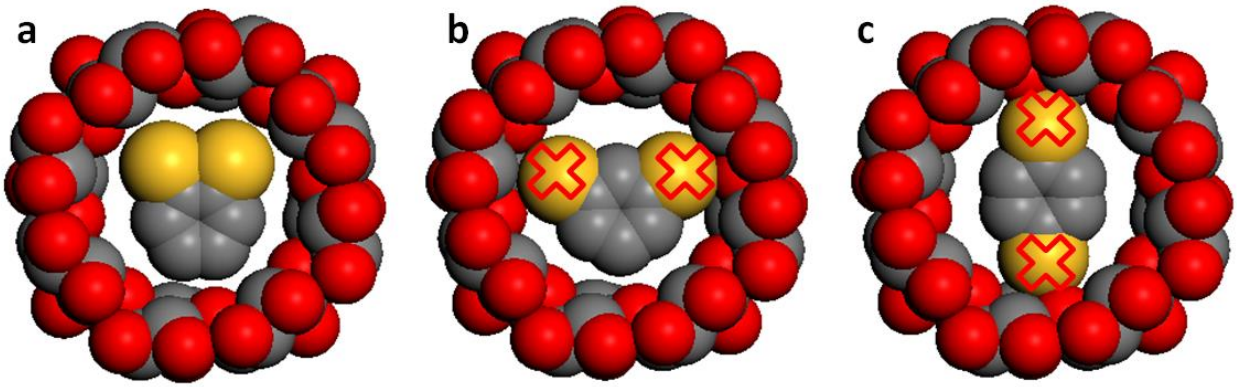

Figure S13. Schematic illustration of the γ-CD rings with **(a)** *ortho*-xylene, **(b)** *meta*-xylene and **(c)** *para*-xylene adsorbed in the ring. Crosses emphasize that methyl groups may overlap with the ring atoms in this orientation. The methyl groups in xylenes are illustrated as single yellow spheres, carbons and oxygens are shown in grey and red, respectively. All hydrogen atoms are removed for the sake of clarity.

Table S9. Lennard-Jones Parameters for CD-MOF-2

Atom	ϵ/k (K)	σ (Å)	Force field
Rb	26.67	2.60	UFF[13]
O	30.19	3.11	UFF
C	52.83	3.43	UFF
H	22.14	2.57	UFF

Table S10. Lennard-Jones Parameters and Partial Charges for Xylene Isomers

Atom	ϵ/k (K)	σ (Å)	Charge (e)	Force field
C	35.24	3.55	-0.115	OPLS[14]
H	15.08	2.42	0.115	OPLS
CH_3	85.47	3.80	0.115	OPLS

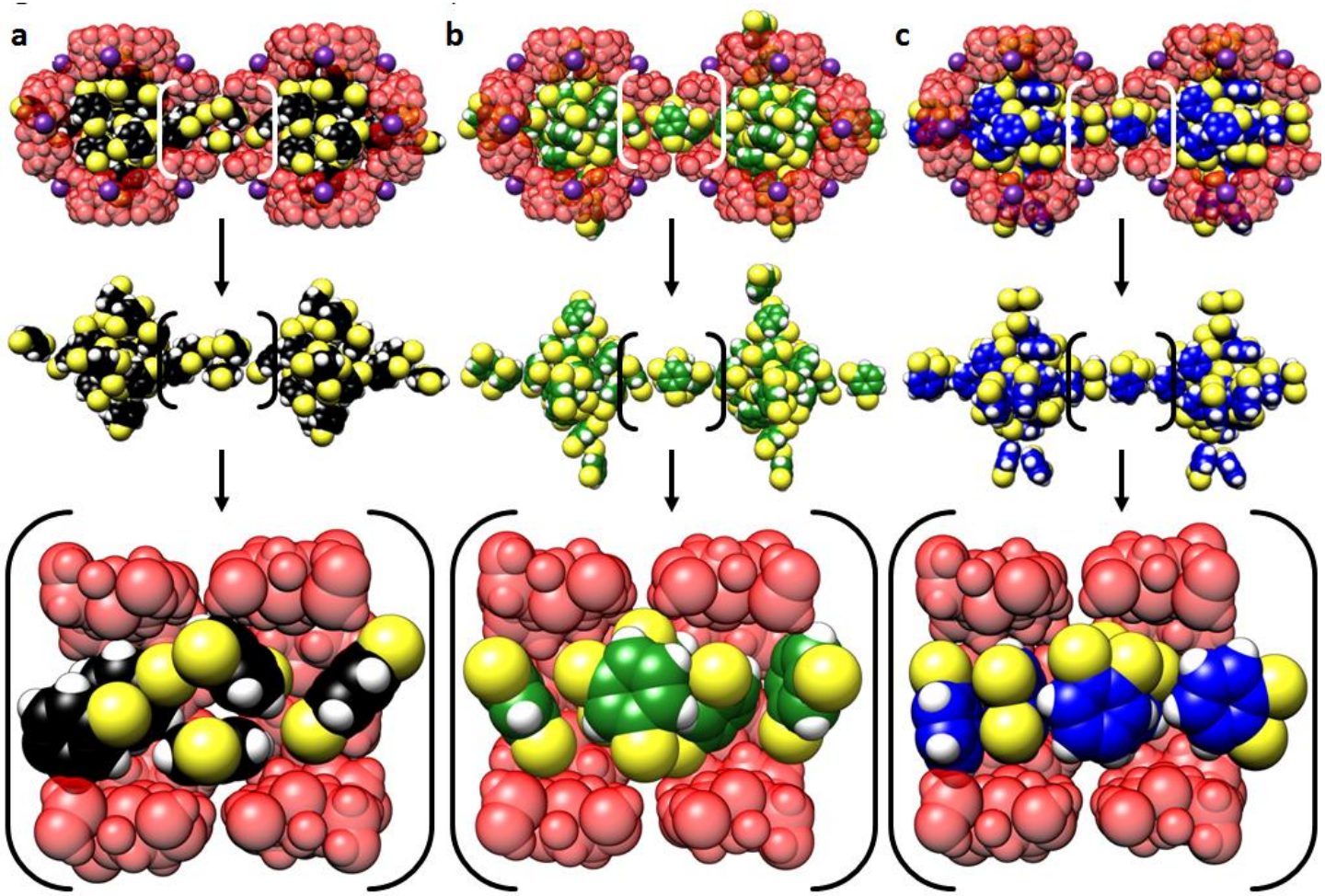

Figure S14. Molecular simulation snapshots of the xylene isomers within the CD-MOF-2 framework viewed down the <1 0 0> axis. Pure components **(a)** *para*-, **(b)** *meta*- and **(c)** *ortho*-xylene. With *para*- **(black)**, *meta*- **(green)**, *ortho*-xylene **(blue)** and their corresponding methyl-groups colored **(yellow)** for the sake of clarity.

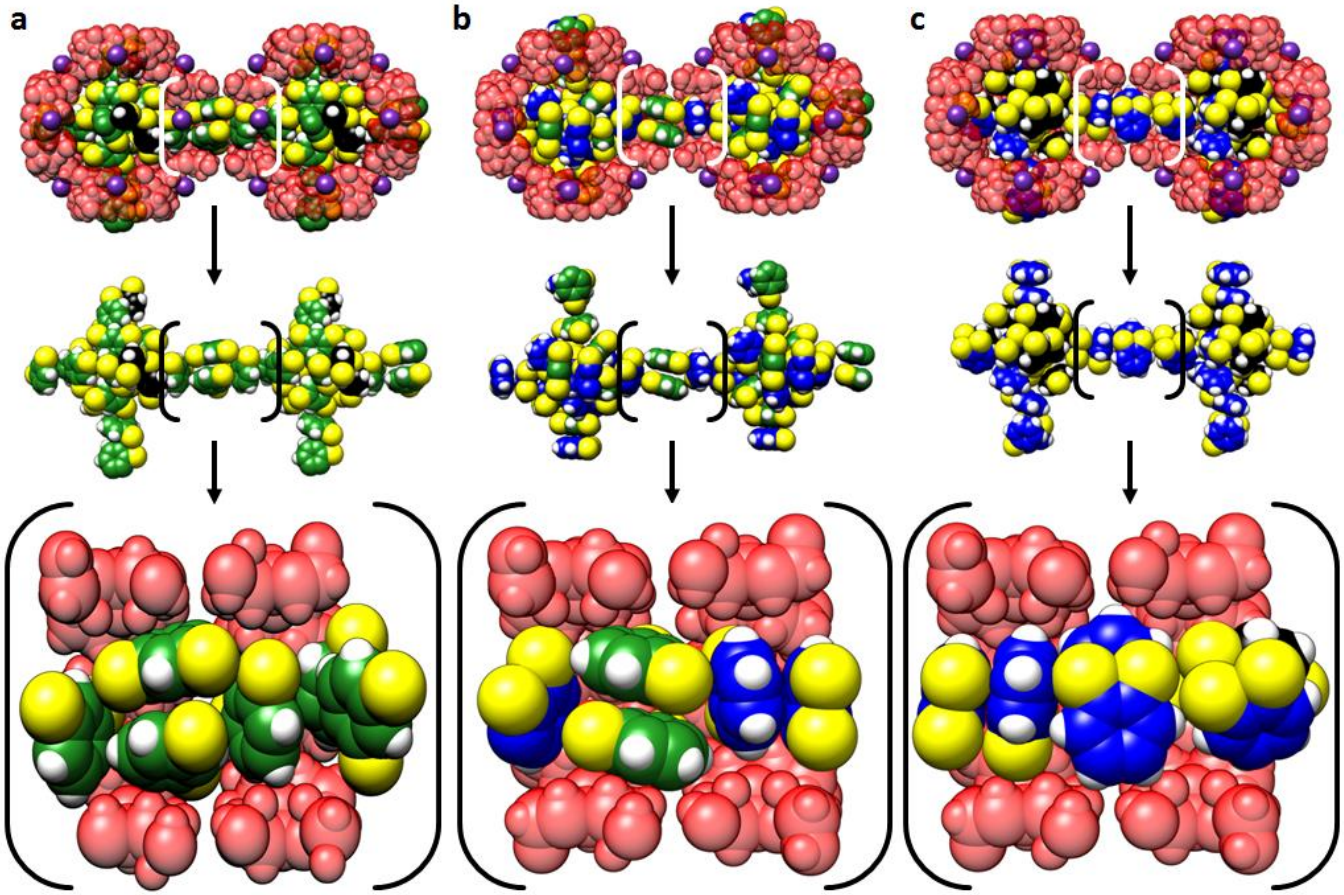

Figure S15. Molecular simulation snapshots of the xylene isomers within the CD-MOF-2 framework viewed down the <1 0 0> axis. Equimolar mixture snapshots of xylene isomers **(a)** *meta-/para-*, **(b)** *ortho-/meta-* and **(c)** *ortho-/para-*xylene. With *para-* **(black)**, *meta-* **(green)**, *ortho-*xylene **(blue)** and their corresponding methyl-groups colored **(yellow)** for the sake of clarity.

Table S11. Breakdown of Interaction Energies for Equimolar Xylene Mixtures at 1 kPa and 298 K in CD-MOF-2

	Potential energy kJ mol^{-1}			
	***ortho*-xylene**		***para*-xylene**	
	vdW	**Coulomb**	**vdW**	**Coulomb**
Adsorbate-Framework	-49.1	-1.2	-39.4	-1.1
Adsorbate-Adsorbate	-12.3	0.3	-7.5	-0.08
	***ortho*-xylene**		***meta*-xylene**	
	vdW	**Coulomb**	**vdW**	**Coulomb**
Adsorbate-Framework	-47.7	-1.2	-43.8	-1
Adsorbate-Adsorbate	-11.4	0.3	-7.8	0.08
	***meta*-xylene**		***para*-xylene**	
	vdW	**Coulomb**	**vdW**	**Coulomb**
Adsorbate-Framework	-47.3	-0.9	-43.2	-0.9
Adsorbate-Adsorbate	-10.7	0.01	-8.2	-0.13

6.1. *Quantum Chemical Calculations*

Single-point calculations at the M06/6-31G level of theory were performed for 32 points to sample interaction regions as each xylene isomer gradually moves away from the center of γ-CD ring as represented in **Figure S16** and **Figure S17**. In these calculations, the geometries of the γ-CD rings as well as the xylenes' geometries are held fixed at their isolated optimal geometries. To account for the orientation dependence of the binding energies, we repeated the above calculations for three different initial orientations of xylenes inside an isolated γ-CD ring. For each approach the orientation of xylene molecule is held fixed with respect to the γ-CD ring. All single point calculations were carried out with Gaussian 09 program package.[S17]

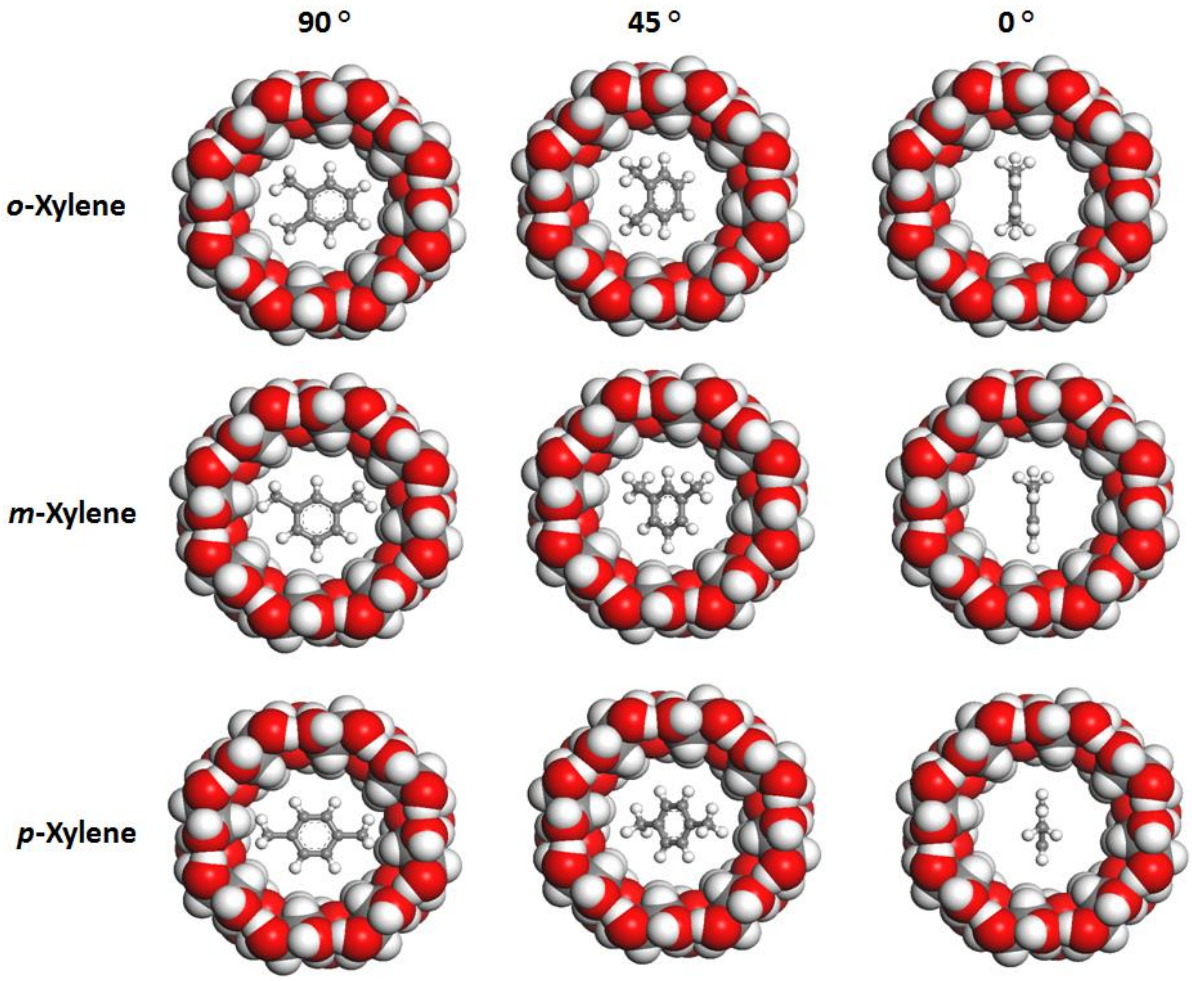

Figure S16. Different orientations of xylene isomers inside the γ-CD rings

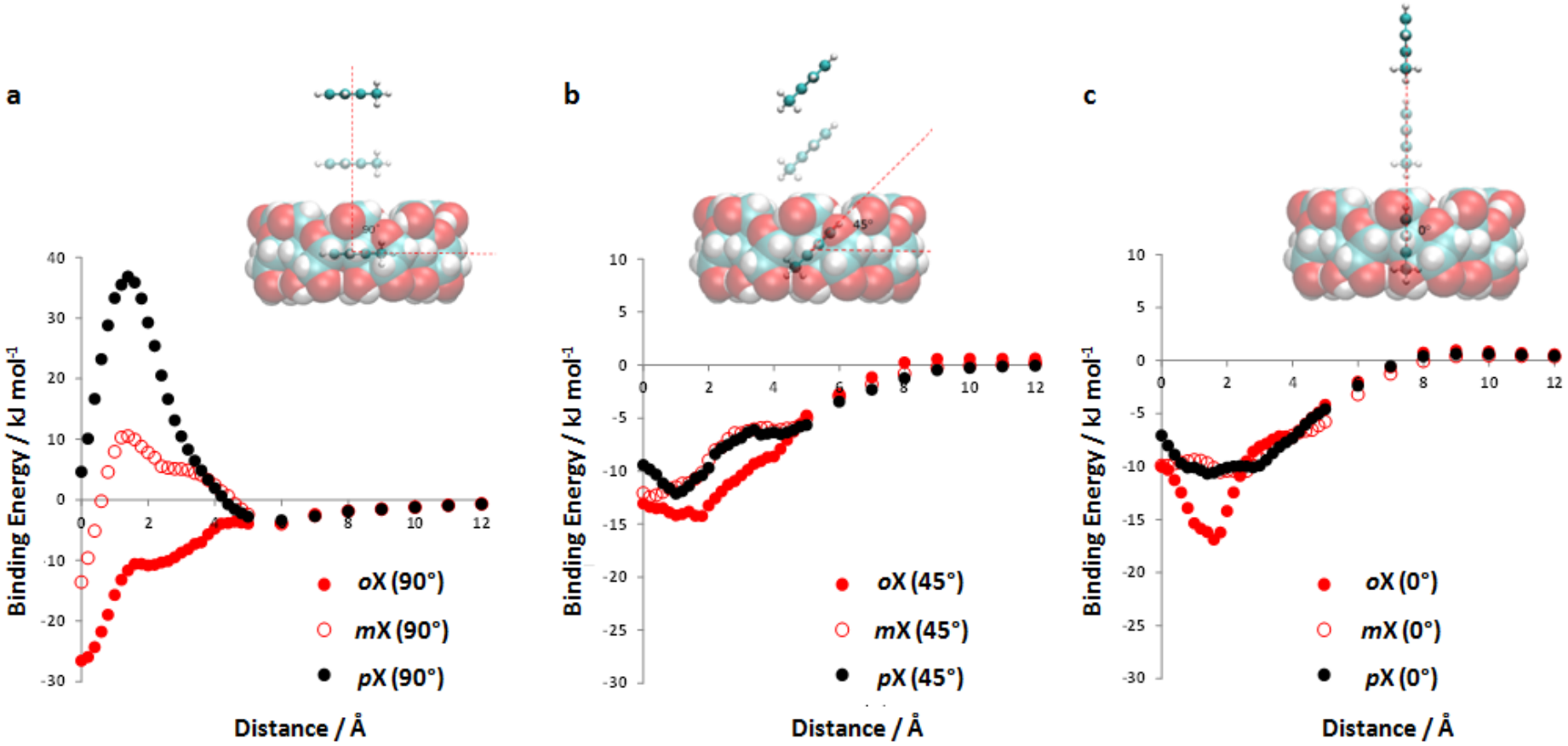

Figure S17. Interaction energies for the xylene isomers for three different orientations of **(a) 9**0°, **(b)** 45° and **(c)** 0° with respect to the γ-CD ring. The schematics show the scanned energy path for each orientation.

7. Vapor-Phase Adsorption Studies

7.1. *Static Vapor Adsorption Studies*

Single component isotherms were obtained for the adsorption of regioisomers of xylene on CD-MOF-2 in order to be able to investigate the mechanism of vapor-phase adsorption and separation. The mass relaxation profiles were analyzed with the Fickian, CBRD and stretched exponential (LDF) models in order to determine the rate limiting mass transfer step and also to determine diffusion coefficients.

7.1.1. *Isotherms, Thermodynamics and Selectivity's*

The adsorption isotherms (**Figure S18**) were analyzed using virial analysis to determine adsorbate-adsorbate and adsorbate-adsorbent interactions (**Table S12**) and selectivity's (**Table S13**) based on Henry's Law which is a fundamental measure of the interaction strength at zero surface coverage.

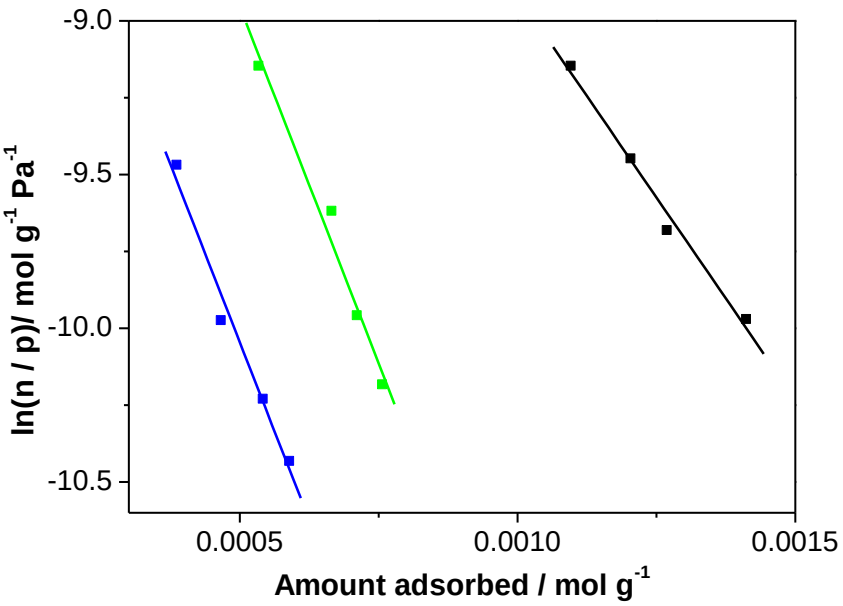

Figure S18. Virial plots for the adsorption of xylene regioisomers on CD-MOF-2 in the low uptake region at 60°C, *para*-xyelne (**black**), *meta*-xylene (**green**) and *ortho*-xylene (**blue**).

Table S12. Virial Parameters for Adsorption of Xylene Regioisomers on CD-MOF-2 at 333K

Regioisomer	A_0 (mol g^{-1} Pa^{-1})	A_1 (g mol^{-1})	K_H (x 10^{-3}) /(mol g^{-1} Pa^{-1})
Para-Xylene	-6.286 ± 0.261	-2630.661 ± 209.091	1.86
Meta-Xylene	-6.634 ± 0.335	-4640.876 ± 498.738	1.31
Ortho-Xylene	-7.733 ± 0.241	-4627.504 ± 480.560	0.44

Limit number of decimal places

A_0 values are related to Henry's Law by the equation $K_H = \exp(A_0)$, which quantifies the interaction strength at zero surface coverage.

Table S13. Xylene Regioisomer Selectivity on CD-MOF-2 based on Henry's Constants at 333 K

Ratio of Henry's constants	Selectivity
K_{para}/K_{meta}	1.42
K_{para}/K_{ortho}	4.25
K_{meta}/K_{ortho}	3.00

7.1.2. *Adsorption Kinetics*

Diffusion of molecules into pores may be influenced by molecular sieving through constrictions in the pore structure and surface chemistry and by surface diffusion via a site-to-site hopping mechanism. Molecular sieving depends on the critical dimension(s) of the adsorbate relative to the shape of the pore(s). In the case of slit shaped pores, one dimension is critical, whereas for pores with circular cross-section, two critical dimensions are significant. Surface diffusion is controlled by adsorbate-adsorbent and adsorbate-adsorbate interactions, and related to the enthalpy of adsorption.

Linear driving force (LDF),[S18,S19] combined barrier resistance/Fickian diffusion,[S20] Fickian[S21] and stretched exponential[S22] models have been used to describe diffusion of molecules into porous particles. Surface diffusion of molecules is an activated process involving hopping between adjacent sites and is affected by interaction between the adsorbed molecule and surface sites. In the case of small pores electrostatic interaction and steric effects become important and, may result in very large differences in molecular diffusivity for similar molecules. Klafter and Shlesinger showed[S22] that the stretched exponential model is a common underlying mathematical structure relating the Forster direct-transfer mechanism,[S23] which involves relaxation via parallel channels and the serial hierarchically constrained dynamics[S24] and defect-diffusion models.[S25-S27] The unifying mathematical feature of the models is a scale-invariant distribution of relaxation times. Surface diffusion of molecules constrained in pores has similar characteristics. The stretched exponential (SE) model is described by the following equation:

$$\frac{M_t}{M_e} = 1 - e^{-(kt)^{\beta}} \qquad \textbf{(4)}$$

where M_t is the mass at time t, M_e is the mass at equilibrium, k is the mass transfer rate constant (s^{-1}) and t is the time(s). The exponent parameter β equilibrium is material dependent and reflects the width of the distribution of relaxation times. The SE model is 3-dimensional with a single relaxation time when β = 1 (Linear Driving Force (LDF) model)[S22] and 1-dimensonal with a distribution of relaxation times when β = 0.5.

There are similarities in models based on molecular surface diffusion and macroscopic diffusion into particles. The stretched exponential model can describe the range of kinetic profiles with the exponent β quantifying the shape of the kinetic profile in comparison to Fickian (β ~ 0.65 for spherical particles) and LDF (β = 1). Furthermore, the SE model also provides a good description of Fickian diffusion into a one-dimensional slab and cylindrical particles. A stretched exponential model has been used to describe the adsorption and desorption kinetics of a wide

range of gases and vapors on metal organic framework materials[S28, S29] and activated carbons.[S30-S33] Hence, the SE model has a wide applicability for studying adsorption dynamics for porous materials with widely different particle shapes. This model can serve as a link between models based diffusion into particles and surface diffusion of molecules with a hierarchical scale invariant properties. Previous studies of MOFs with windows in pores has shown that the adsorption kinetics can be described by either double exponential or double stretched exponential models corresponding to two processes a) diffusion through barriers due to narrow windows with a high activation energy and b) diffusion along the pores with a lower barrier to diffusion[S29, S34] and also, diffusion along two types of pores with different shapes.[S28]

In real systems, particle size distributions and irregular particle shapes may make the determination of diffusion coefficients difficult. The kinetic profiles for each adsorption isotherm pressure increment were measured for small pressure increments where the diffusivities may be considered constant, to understand the dynamics associated with the adsorption isotherms. All kinetic profiles were initially fit using the SE model. Based on the values of the exponent, the Fickian, CBRD or LDF mass transfer model was used in order to determine the diffusion coefficients.

The LDF model describes the adsorption/desorption kinetic profiles when diffusion through a surface layer is the rate determining process and is described by the following equation:

$$\frac{M_t}{M_e} = 1 - e^{-kt} \qquad \textbf{(5)}$$

where M_t is mass uptake at time t, M_e is mass uptake at equilibrium and k is the mass transfer rate constant. The adsorption kinetics can be compared using the rate constants (k) determined either from the gradients of graphs of $\ln(1-M_t/M_e)$ versus time or by fitting the adsorption uptake curves to equation (5). The values of the LDF intraparticle mass transfer coefficient (k) can be converted to effective intraparticle diffusion coefficients (D_c) using the equation below:[S35]

$$k = 15D_c/r^2 \quad \textbf{(6)}$$

where r is the radius of the particle.

Fick's law for isothermal diffusion into a homogeneous sphere is given by the following equation:[S21]

$$\frac{M_t}{M_e} = 1 - \frac{6}{\pi^2}\sum_{n=1}^{\infty}\left(\frac{1}{n^2}\right)\exp\left(\frac{-Dn^2\pi^2 t}{r^2}\right) \quad \textbf{(7)}$$

where M_t is mass uptake at time t , M_e is mass uptake at equilibrium, D is diffusivity and r is radius of the particle. The series in the above equation converges very rapidly and a graph of ln(1 - M_t/M_e) versus time is close to linearity in the uptake region $M_t/M_e > 0.6$. Therefore, the graph only differs from the LDF model in the initial uptake region where $M_t/M_e < 0.6$. Fickian diffusion was only observed for *para*-xylene adsorption on CD-MOF-2 at low pressure.

The combined barrier resistance/diffusion (CBRD) model is based on the assumption of the presence of a surface barrier resistance and subsequent diffusion in a spherical microporous system by Fick's law. The partial differential equation, initial condition and boundary conditions for isothermal diffusion into a spherical particle are as follows:[S20]

$$\frac{\partial C}{\partial t} = D\left[\left(\frac{\partial^2 C}{\partial r^2}\right) + \left(\frac{2}{r}\right)\left(\frac{\partial C}{\partial r}\right)\right] \quad \textbf{(8)}$$

where D is the crystallite diffusivity ($cm^2\ s^{-1}$), C is the sorbate concentration in the crystallite (mmol cm^{-3}), r is the radial co-ordinate and t is the time. The initial condition is

$$C(r, 0) = 0 \quad \textbf{(9)}$$

The boundary condition at the surface of the particle is

$$D\frac{\partial C(r_S t)}{\partial r} = k_b\,(C^*(t) - C(r,t)) \qquad \textbf{(10)}$$

while the boundary condition at the center is

$$\frac{\partial C(r_c t)}{\partial r} = 0 \qquad \textbf{(11)}$$

where D is the crystallite diffusivity ($m^2\ s^{-1}$), k_b is the surface barrier resistance ($m\ s^{-1}$), r is the radial co-ordinate, r_s is the surface radial co-ordinate and r_c is the center radial co-ordinate (m), t is time(s), C is the sorbate concentration in the crystallite (mol m^{-3}) and C^* the surface concentration in equilibrium with the gas phase (mol m^{-3}). The parameters derived from the model are k_b the barrier resistance constant and k_d resistance due to diffusion in the pores. The partial differential equation was solved using MATLAB with PDEPE solver coupled with a non-linear least squares function in order to fit the PDE solution to the experimental kinetic profiles. The adjustable parameters were the diffusion coefficient k_D and the surface barrier resistance constant k_B.

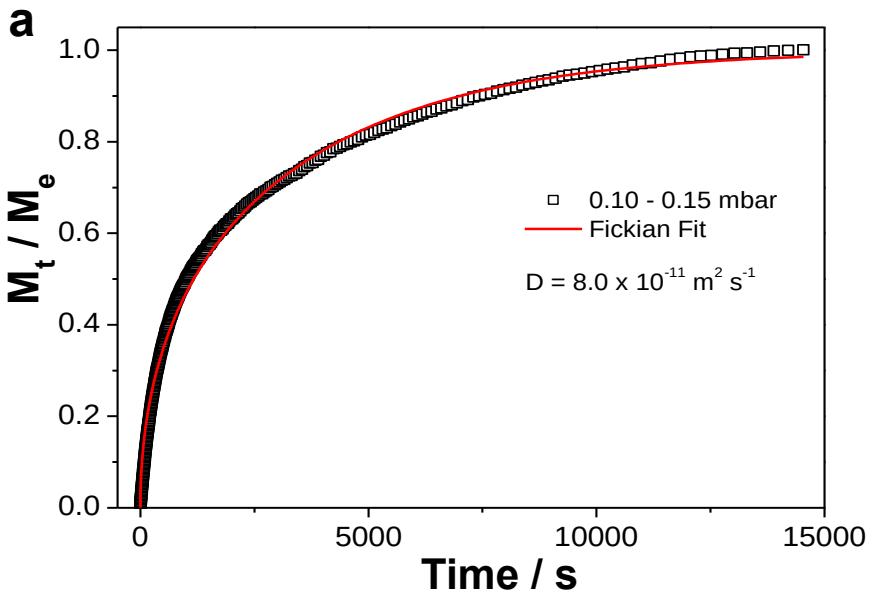
a
1.0
0.8
0.6
0.4
0.2
0.0
M_t / M_e
0
5000
10000
15000
Time / s
0.10 - 0.15 mbar
Fickian Fit
D = 8.0 x 10^{-11} m^2 s^{-1}

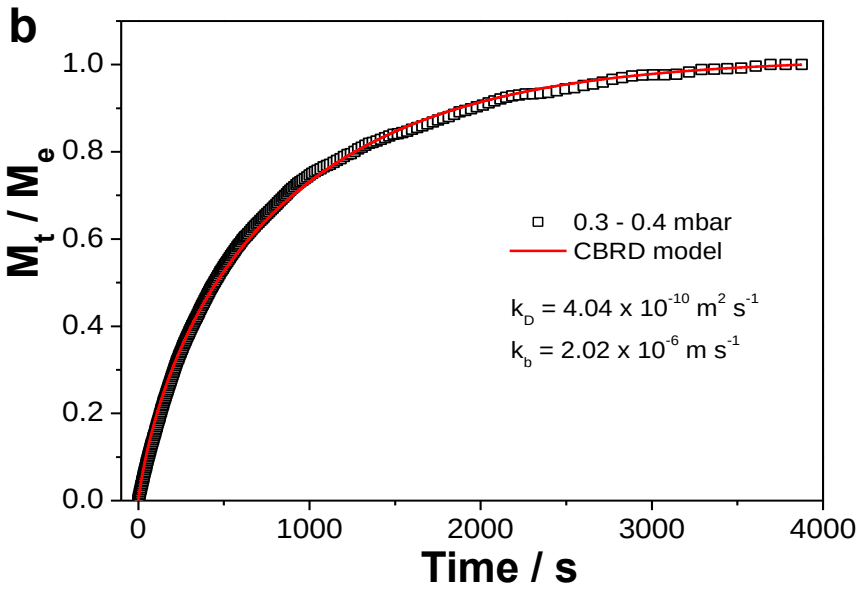
b
1.0
0.8
0.6
0.4
0.2
0.0
M_t / M_e
0
1000
2000
3000
4000
Time / s
0.3 - 0.4 mbar
CBRD model
k_D = 4.04 x 10^{-10} m^2 s^{-1}
k_b = 2.02 x 10^{-6} m s^{-1}

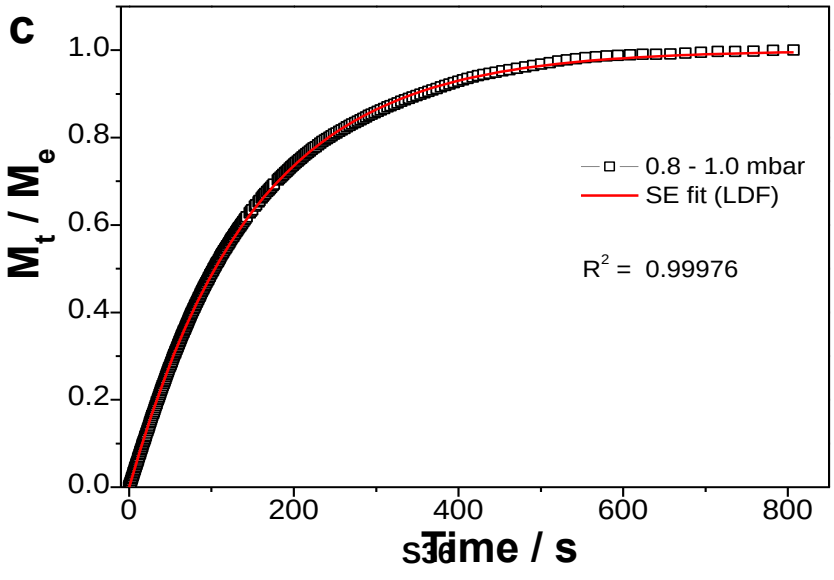
c
1.0
0.8
0.6
0.4
0.2
0.0
M_t / M_e
0
200
400
600
800
Time / s
0.8 - 1.0 mbar
SE fit (LDF)
R^2 = 0.99976

Figure S19. Kinetic profiles and models for fitting for *para*-xylene vapor adsorption on CD-MOF-2 at 333K **(a)** Fickian model at 0.1–0.15 mbar **(b)** CBRD model 0.3–0.4 mbar **(c)** Stretched Exponential (SE) model at 0.8–1 mbar..

Details of the SE fit are required for profile c)

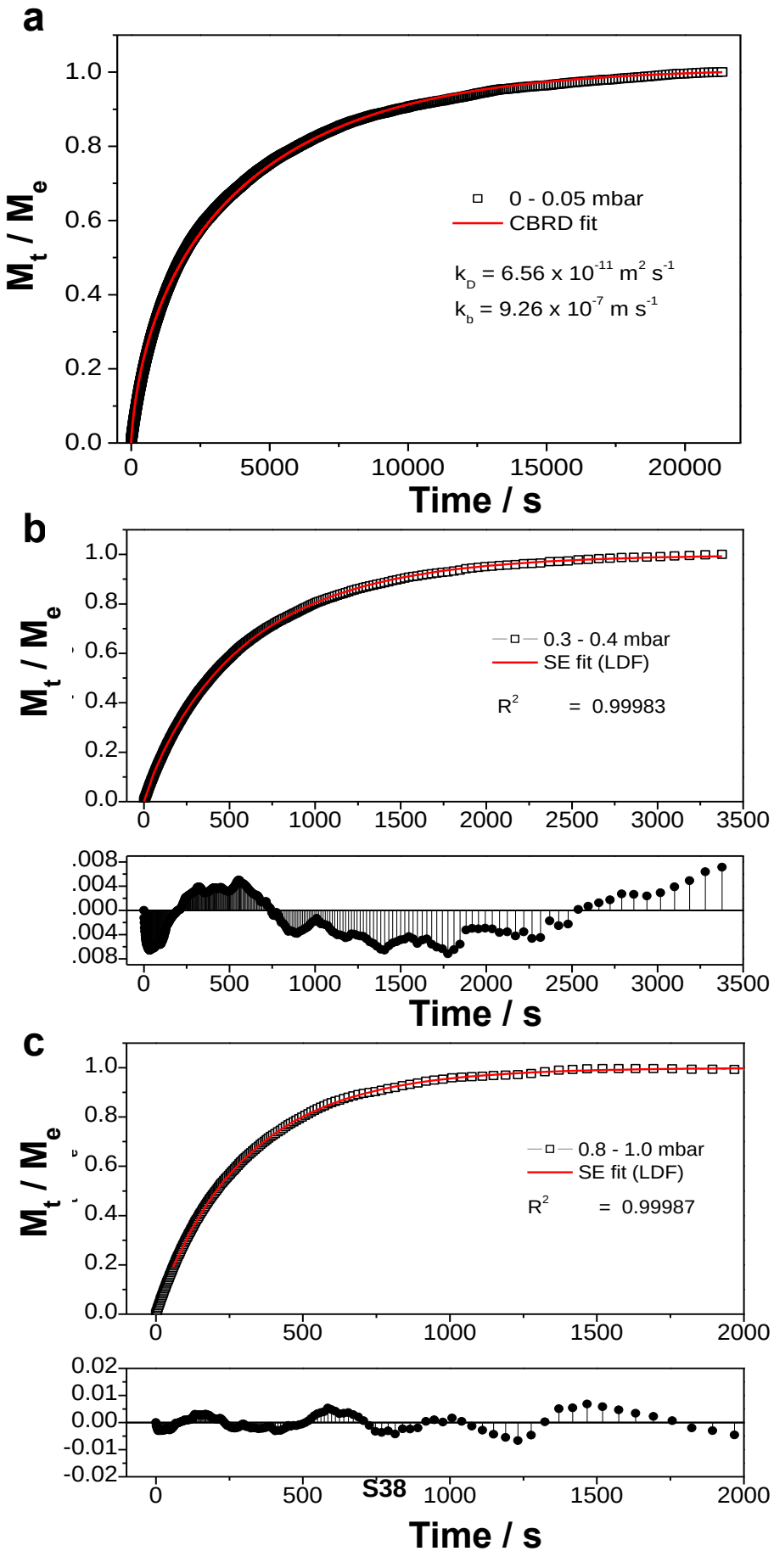
a
1.0
0.8
0.6
0.4
0.2
0.0
M_t / M_e
0 - 0.05 mbar
CBRD fit
k_D = 6.56 x 10^{-11} m^2 s^{-1}
k_b = 9.26 x 10^{-7} m s^{-1}
0
5000
10000
15000
20000
Time / s
b
1.0
0.8
0.6
0.4
0.2
0.0
M_t / M_e
0.3 - 0.4 mbar
SE fit (LDF)
R^2 = 0.99983
0
500
1000
1500
2000
2500
3000
3500
.008
.004
.000
.004
.008
Time / s
c
1.0
0.8
0.6
0.4
0.2
0.0
M_t / M_e
0.8 - 1.0 mbar
SE fit (LDF)
R^2 = 0.99987
0
500
1000
1500
2000
0.02
0.01
0.00
-0.01
-0.02
Time / s

Figure S20. Typical kinetic profiles and models for fitting for *meta*-xylene vapor adsorption on CD-MOF-2 at 333K. **(a)** CBRD model at 0.0–0.05 mbar **(b)** Stretched Exponential (SE) model 0.3–0.4 mbar **(c)** Stretched Exponential (SE) model at 0.8–1 mbar

Details of the SE fit are required for profile b) and

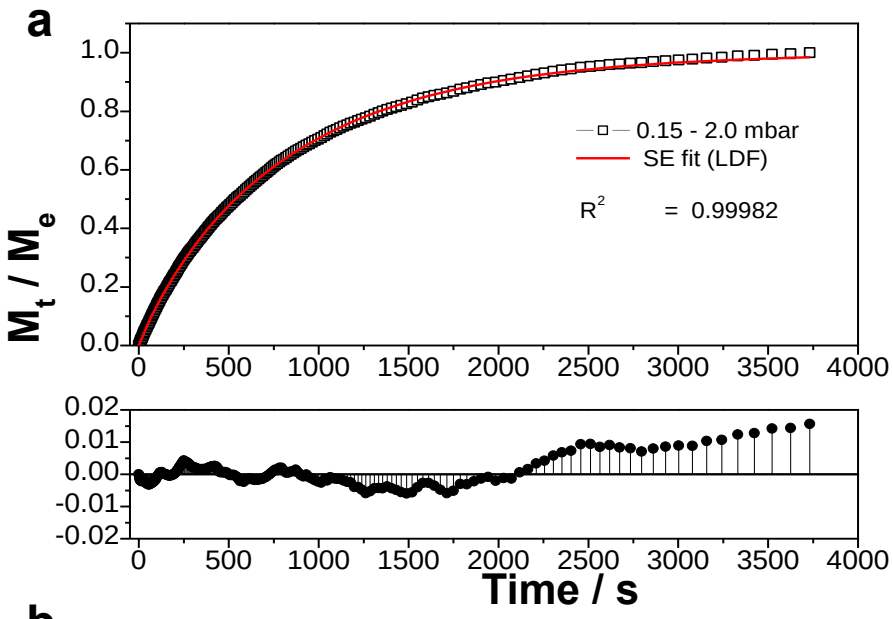
a
1.0
0.8
0.6
0.4
0.2
0.0
M_t / M_e
0.15 - 2.0 mbar
SE fit (LDF)
R^2 = 0.99982
0 500 1000 1500 2000 2500 3000 3500 4000
0.02
0.01
0.00
-0.01
-0.02
0 500 1000 1500 2000 2500 3000 3500 4000
Time / s

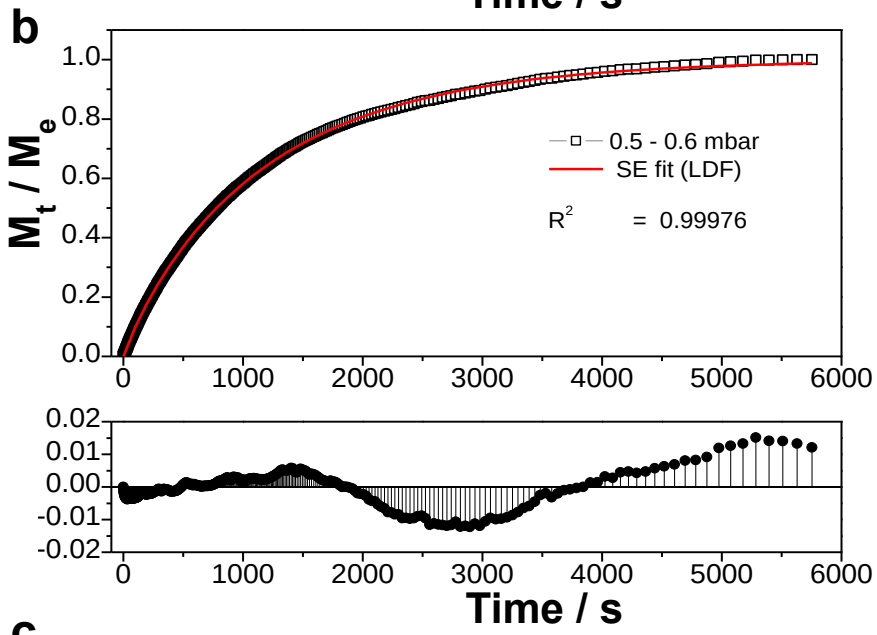
b
1.0
0.8
0.6
0.4
0.2
0.0
M_t / M_e
0.5 - 0.6 mbar
SE fit (LDF)
R^2 = 0.99976
0 1000 2000 3000 4000 5000 6000
0.02
0.01
0.00
-0.01
-0.02
0 1000 2000 3000 4000 5000 6000
Time / s

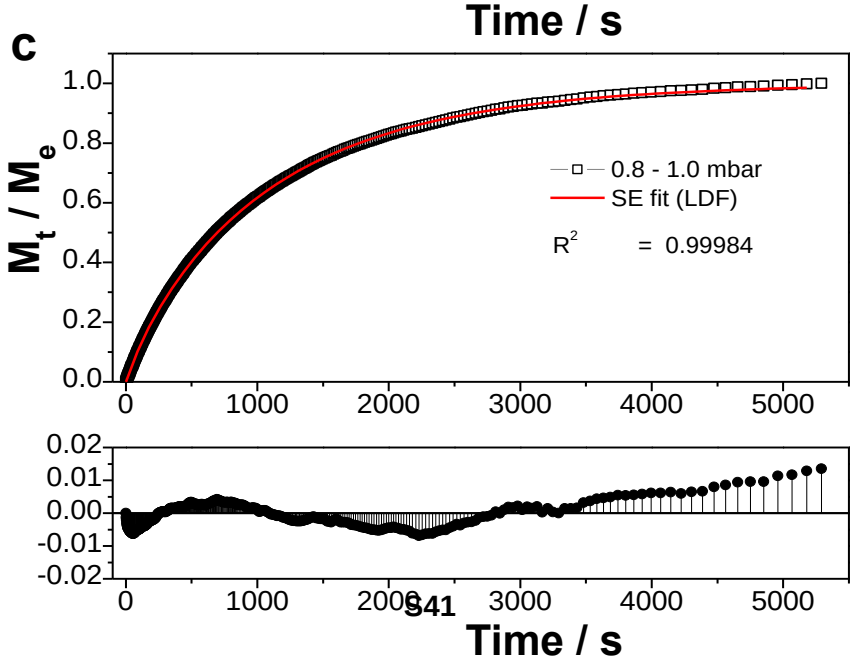
c
1.0
0.8
0.6
0.4
0.2
0.0
M_t / M_e
0.8 - 1.0 mbar
SE fit (LDF)
R^2 = 0.99984
0 1000 2000 3000 4000 5000
0.02
0.01
0.00
-0.01
-0.02
0 1000 2000 3000 4000 5000
Time / s

Figure S21. Typical kinetic profiles and models for fitting for *ortho*-xylene vapor adsorption on CD-MOF-2 at 333K **(a)** Stretched Exponential (SE) model at 0.15–0.2 mbar **(b)** Stretched Exponential (SE) model 0.5–0.6 mbar **(c)** Stretched Exponential (SE) model at 0.8–1 mbar

Details of the SE fit are required for profile a), b) and c)

FD = Fickian diffusion into a spherical particle, **CBRD** = Combined Barrier Resistance Diffusion Model for spherical particle, **LDF** = Linear Driving Force mass transfer model, UMRP – unquantifiable mass relaxation profile

Table S14. Diffusion Coefficients and Surface Barrier Resistance Constants for Fickian, CBRD and LDF for *para*-Xylene Vapor Adsorption on CD-MOF-2 at 333 K.

Pressure / mbar	Amount Adsorbed / mmol g^{-1}	Diffusion Coefficient (D) / (m^2 s^{-1})	Surface Barrier from CBRD model / K_b (m s^{-1})	Mass transfer model
0.052	0.686			UMRP
0.103	1.096			UMRP
0.152	1.203	8.00×10^{-11}		FD
0.203	1.269	2.74×10^{-10}	2.20×10^{-5}	CBRD
0.302	1.412	1.80×10^{-10}	6.45×10^{-6}	CBRD
0.402	1.556	4.04×10^{-10}	2.02×10^{-6}	CBRD
0.502	1.867			UMP
0.602	2.190	1.96×10^{-10}		LDF
0.702	2.440	2.63×10^{-10}		LDF
0.803	2.526			UMP
1.003	2.617	1.36×10^{-9}		LDF
1.502	2.694	2.10×10^{-9}		LDF
1.983	2.738			UMRP
2.487	2.770			UMRP

Table S15. Diffusion Coefficients and Surface Barrier Resistance Constants for Fickian, CBRD and LDF for *meta*-Xylene Vapor Adsorption on CD-MOF-2 at 333 K.

Pressure / mbar	Amount Adsorbed / mmol g^{-1}	Diffusion Coefficient (D) / (m^2 s^{-1})	Surface barrier from CBRD model / K_b (m s^{-1})	Mass transfer model
0.050	0.533	6.56×10^{-11}	9.26×10^{-7}	CBRD
0.100	0.665	5.86×10^{-10}		LDF
0.150	0.710	6.70×10^{-10}		LDF
0.200	0.756	5.70×10^{-10}		LDF
0.300	0.852	4.49×10^{-10}		LDF
0.400	0.957	3.49×10^{-10}		LDF
0.500	1.125			UMP
0.600	1.255			UMRP
0.700	1.309	4.36×10^{-10}	5.37×10^{-6}	CBRD
0.800	1.354	4.36×10^{-10}	5.32×10^{-6}	CBRD
1.000	1.424	6.78×10^{-10}		LDF
1.500	1.641			UMRP
1.989	2.440	2.45×10^{-10}		LDF
2.493	2.656	5.74×10^{-10}		LDF

2.995	2.732			UMP

Table S16. Diffusion Coefficients and Surface Barrier Resistance Constants for Fickian, CBRD and LDF for *ortho*-Xylene Vapor Adsorption on CD-MOF-2 at 333 K.

Pressure / mbar	Amount Adsorbed / mmol g^{-1}	Diffusion Coefficient (D) / (m^2 s^{-1})	Surface barrier from CBRD model / K_b (m s^{-1})	Mass transfer model
0.050	0.386	7.96×10^{-11}		LDF
0.100	0.466	1.27×10^{-10}	2.90×10^{-6}	CBRD
0.200	0.589	2.55×10^{-10}		LDF
0.300	0.718	1.47×10^{-10}		LDF
0.400	0.830	1.49×10^{-10}		LDF
0.500	0.927	1.43×10^{-10}		LDF
0.600	1.006	1.76×10^{-10}		LDF
0.700	1.067	1.69×10^{-10}		LDF
0.799	1.119	2.08×10^{-10}		LDF
1.000	1.214	1.96×10^{-10}		LDF
1.499	1.420	1.76×10^{-10}		LDF
1.994	2.487	8.78×10^{-11}		LDF
2.989	2.639	5.60×10^{-10}	4.37×10^{-6}	CBRD
3.495	2.667	6.43×10^{-10}		LDF

7.2. *Breakthrough Data*

Breakthrough experiments were carried out in a 4-mm glass U-tube with CD-MOF-2 crystals. CD-MOF-2 (1.46 g) was used to fill the tube at a length of 16 cm. The sample was purged with dry N_2 at 60 ºC overnight to ensure the complete activation of the sample prior to breakthrough measurements. Dry N_2 at a rate of 20 mL min^{-1} was bubbled through a mixture of xylene isomers (15 mL each) at atmospheric pressure. The effluent was passed through a VICI Valco 6-way sampling valve. An aliquot (0.25 mL) of gas was sampled every 5 min and delivered to a Perkin Elmer Clarus 500 Gas Chromatograph fitted with a Supelco SCOT capillary GC column (Sigma-Aldrich 23813-U, 50 ft long, 0.02 in. outside diameter) maintained at 90 ºC. The analyses were performed using an injector and detector (FID) temperature of 220 ºC and N_2 was used as the carrier gas which was maintained at an inlet pressure of 1.5 psi with a split ratio of 10:1. Baseline separation of xylene isomers was achieved and all peaks were easily integrated in the resulting GC trace shown in **Figure S23**.

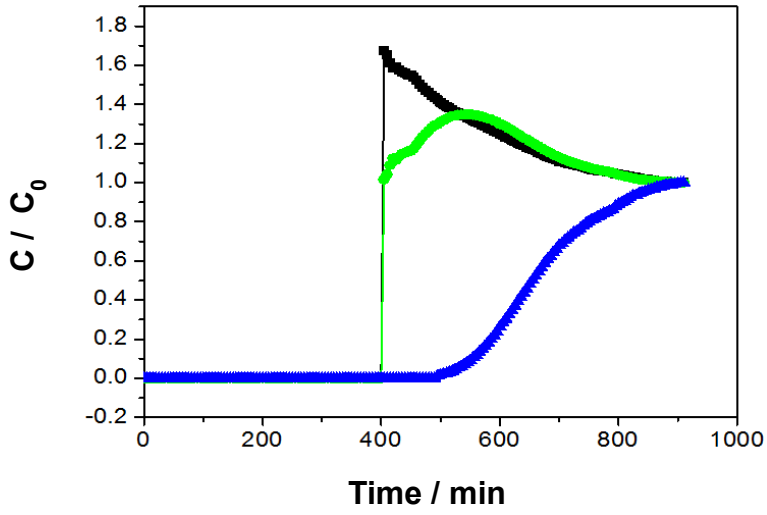

Figure S23. Concentration plot of the vapor-phase breakthrough experiment for xylene isomers at 60°C using N_2 as the carrier gas at 20 mL min^{-1} through a CD-MOF-2 column, *para*-xylene (**black**), *meta*-xylene (**green**) and *ortho*-xylene (**blue**).

8. References

(S1) Smaldone, R. A.; Forgan, R. S.; Furukawa, H.; Gassensmith, J. J.; Slawin, A. M. Z.; Yaghi, O. M.; Stoddart, J. F. *Angew. Chem. Int. Ed.* **2010**, *49*, 8630.

(S2) Furukawa, Y.; Ishiwata, T.; Sugikawa, K.; Kokado, K.; Sada, K. *Angew. Chem. Int. Ed.* **2012**, *51*, 10566.

(S3) Minceva, M.; Rodrigues, A. E. *AIChE Journal* **2007**, *53*, 138.

(S4) Lima, R. M.; Grossmann, I. E. *AIChE Journal* **2009**, *55*, 354.

(S5) Eccli, W. D. & Fremuth, A. D. S. Single temperature stage crystallisation of *para*-xylene *US Patent No.* 5,498,822 (1996).

(S6) Minceva, M.; Rodrigues, A. E. *Chem. Eng. Res. Des.* **2004**, *82*, 667.

(S7) Alaerts, L.; Kirschhock, C. E. A.; Maes, M.; van der Veen, M. A.; Finsy, V.; Depla, A.; Martens, J. A.; Baron, G. V.; Jacobs, P. A.; Denayer, J. F. M.; De Vos, D. E. *Angew. Chem. Int. Ed.* **2007**, *46*, 4293.

(S8) Alaerts, L.; Maes, M.; Giebeler, L.; Jacobs, P. A.; Martens, J. A.; Denayer, J. F. M.; Kirschhock, C. E. A.; De Vos, D. E. *J. Am. Chem. Soc.* **2008**, *130*, 14170.

(S9) El Osta, R.; Carlin-Sinclair, A.; Guillou, N.; Walton, R. I.; Vermoortele, F.; Maes, M.; de Vos, D.; Millange, F. *Chem. Mater.* **2012**, *24*, 2781.

(S10) Moreira, M. A.; Santos, J. C.; Ferreira, A. F. P.; Loureiro, J. M.; Ragon, F.; Horcajada, P.; Shim, K.-E.; Hwang, Y.-K.; Lee, U. H.; Chang, J.-S.; Serre, C.; Rodrigues, A. E. *Langmuir* **2012**, *28*, 5715.

(S11) Snyder, L.R.; Kirkland, J.J.; Glajch, J.L. Practical HPLC method development Second Edition, John Wiley & Sons, Inc. (1997).

(S12) Gupta, A.; Chempath, S.; Sanborn, M. J.; Clark, L. A.; Snurr, R. Q. *Mol. Simul.* **2003**, *29*, 29.

(S13) Rappe, A. K.; Casewit, C. J.; Colwell, K. S.; Goddard, W. A.; Skiff, W. M. *J. Am. Chem. Soc.*, **1992**, *114*, 10024.

(S14) Jorgensen, W. L.; Nguyen, T. B. *J. Comput. Chem.*, **1993**, *14*, 195.

(S15) Wilmer, C. E.; Kim, K. C.; Snurr, R. Q. *J. Phys. Chem. Lett.*, **2012**, *3*, 2506.

(S16) Dufner, H.; Kast, S. M.; Brickmann, J.; Schlenkrich, M. *J. Comput. Chem.*, **1997**, *18*, 660.

(S17) Frisch, M. J.; Trucks, G. W.; Schlegel, H. B.; Scuseria, G. E.; Robb, M. A.; Cheeseman, J. R; Scalmani, G.; Barone, V.; Mennucci, B.; Petersson, G. A.; Nakatsuji, H.; Caricato, M.; Li, X.; Hratchian, H. P.; Izmaylov, A. F.; Bloino, J.; Zheng, G.; Sonnenberg, J. L.; Hada, M.; Ehara, M.; Toyota, K.; Fukuda, R.; Hasegawa, J.; Ishida, M.; Nakajima, T.; Honda, Y.; Kitao, O.; Nakai, H.; Vreven, T.; Montgomery, J. A. Jr.; Peralta, J. E.; Ogliaro, F.; Bearpark, M.; Heyd, J. J.; Brothers, E.; Kudin, K. N.; Staroverov, V. N.; Kobayashi, R.; Normand, J.; Raghavachari, K.; Rendell, A.; Burant, J. C.; Iyengar, S. S.; Tomasi, J.; Cossi, M.; Rega, N.; Millam, M. J.; Klene, M.; Knox, J. E.; Cross, J. B.; Bakken, V.; Adamo, C.; Jaramillo, J.; Gomperts, R.; Stratmann, R. E.; Yazyev, O.; Austin, A. J.; Cammi, R.; Pomelli, C.; Ochterski, J. W.; Martin, R. L.; Morokuma, K.; Zakrzewski, V. G.; Voth, G. A.; Salvador, P.; Dannenberg, J. J.; Dapprich, S.; Daniels, A. D.; Farkas, Ö.; Foresman, J. B.; Ortiz, J. V.; Cioslowski, J.; Fox, D. J.; Gaussian, Inc., Wallingford CT, (2009).

(S18) Glueckauf, E.; Coates, J. I., *J. Chem. Soc.*, **1947**, 1315.

(S19) Glueckauf, E., *Trans. Faraday Soc.*, **1955**, *51*, 1540.

(S20) Loughlin, K. F.; Hassan, M. M.; Fatehi, A. I.; Zahur, M., *Gas Sep. Purif.*, **1993**, *7*, 264.

(S21) Crank, J., *The mathematics of diffusion*; 2nd ed.; Clarendon Press: Oxford, **1975**.

(S22) Klafter, J.; Shlesinger, M. F., *Proc. Natl. Acad. Sci. U. S. A.*, **1986**, *83*, 848.

(S23) Forster, T., *Z. Naturforsch. Teil A*, **1949**, *4*, 321.

(S24) Palmer, R. G.; Stein, D. L.; Abrahams, E.; Anderson, P. W., *Phys. Rev. Lett.*, **1984**, *53*, 958.

(S25) Glarum, S. H., *J. Chem. Phys.*, **1960**, *33*, 1371.

(S26) Bordewijk, P., *Chem. Phys. Lett.*, **1975**, *32*, 592.

(S27) Shlesinger, M. F.; Montroll, E. W., *Proceedings of the National Academy of Sciences of the United States of America- Physical Sciences*, **1984**, *81*, 1280.

(S28) Chen, B.; Zhao, X.; Putkham, A.; Hong, K.; Lobkovsky, E. B.; Hurtado, E. J.; Fletcher, A. J.; Thomas, K. M., *J. Am. Chem. Soc.*, **2008**, *130*, 6411.

(S29) Fletcher, A. J.; Cussen, E. J.; Bradshaw, D.; Rosseinsky, M. J.; Thomas, K. M., *J. Am. Chem. Soc.*, **2004**, *126*, 9750.

(S30) Fletcher, A. J.; Thomas, K. M., *J. Phys. Chem. C*, **2007**, *111*, 2107.

(S31) Fletcher, A. J.; Yuzak, Y.; Thomas, K. M., *Carbon*, **2006**, *44*, 989.

(S32) Bell, J. G.; Zhao, X.; Uygur, Y.; Thomas, K. M., *The Journal of Physical Chemistry C*, **2011**, *115*, 2776.

(S33) Zhao, X.; Villar-Rodil, S.; Fletcher, A. J.; Thomas, K. M., *J. Phys. Chem. B*, **2006**, *110*, 9947.

(S34) Fletcher, A. J.; Cussen, E. J.; Prior, T. J.; Rosseinsky, M. J.; Kepert, C. J.; Thomas, K. M., *J. Am. Chem. Soc.*, **2001**, *123*, 10001.

(S35) LeVan, M. D., In *Adsorption Science and Technology, NATO ASI Series E Applied Science*; A.E. Rodriguez, LeVan, M. D., Eds.; Kluwer: Dordrecht, **1989**, *158*, 149.